Max-Planck-Institut für Kolloid- und
Grenzflächenforschung
Abteilung: Theorie und Bio-Systeme

Folding and Aggregation of Amyloid Peptides.

von

Madeleine Kittner

Dissertation
zur Erlangung des akademischen Grades
Doktor der Naturwissenschaften (Dr. rer. nat.)
in der Wissenschaftsdisziplin Physikalische Biochemie

eingereicht an der
Mathematisch-Naturwissenschaftlichen Fakultät
der Universität Potsdam

Potsdam, im April 2011

Published online at the
Institutional Repository of the University of Potsdam:
URL http://opus.kobv.de/ubp/volltexte/2011/5357/
URN urn:nbn:de:kobv:517-opus-53570
http://nbn-resolving.de/urn:nbn:de:kobv:517-opus-53570

Contents

Chapter 1

Introduction

Many human disorders are associated with amyloid deposits in different organs or tissues. One of these so-called amyloid diseases is Alzheimer's disease (AD), an incurable, degenerative disorder which is characterized by widespread death of neurons resulting in the loss of memory and mental ability [1]. The exact cause of the disease is still unclear. However, present research relates the evolution of AD with two types of protein aggregates in the brain. The extracellular plaques consist of amyloid fibrils containing mainly the Amyloid β (Aβ) peptide. The neurofibrillary tangles occur intraneuronally and consist of twisted filaments containing hyperphosphorylated τ protein [2].

The mechanism underlying the aggregation of Aβ to amyloid fibrils is to date not fully understood. A vast number of experiments support the idea that the early aggregation intermediates in form of soluble oligomers are the major neurotoxic components in the process [3, 4, 5, 6, 7, 8, 9]. In order to develop therapeutic agents which target these toxic intermediates it is essential to gain detailed information about their molecular structure and study the thermodynamics governing transitions between different conformations. The early intermediates are of disordered and transient nature. Therefore, it is very difficult to address these questions in atomic detail using experimental techniques.

In the present work early stages of amyloid formation for two fragments of the Aβ peptide, Aβ(25-35) and Aβ(10-35)-NH_2, are studied by means of atomistic molecular dynamics (MD) simulations. We investigate the folding of the pre-aggregated monomeric states in comparison to experimental data or theoretical studies. In addition, we predict structural features of oligomers and study transitions between disordered and fibril-like states.

The following section gives an introduction to the formation of amyloid fibrils in general. In particular, characteristics of amyloid fibrils, models for the aggregation mechanism and the nature of toxic oligomers are discussed. The second part of the introduction focuses on Alzheimer's disease. It explains the role of Aβ and other factors that were shown to be involved in the process of developing the disease. The nature of

Aβ and previous experimental observations concerning the aggregation of the peptide and shorter fragments are reviewed in Sec. 1.2.1. Neurotoxic effects associated with Aβ and approaches to design therapeutic agents will be shortly discussed in Sec. 1.2.2 and 1.2.3. The last section summarizes the questions addressed by this work.

1.1 Folding and aggregation of polypeptides

Proteins are multi functional biological macromolecules essential for living organisms. Enzymatic proteins can catalyze biochemical reactions. Others can coordinate the transport of substances through membranes or the blood, e.g. hemoglobin transports oxygen. Molecular motor proteins such as kinesin or myosin transform chemical energy into mechanical work. Proteins are involved in processes regulating the immune response and biosynthesis. They are also used as storage molecules and for mechanical support.

In comparison to their various functions, proteins have a rather simple molecular framework. They are heteropolymers of the twenty proteinogenic amino acids. Individual amino acid residues are connected via a peptide bond which is planar due to its partial double bond character. Fig. 1.1 shows a polypeptide chain with one peptide bond marked in red. The figure also shows how the backbone conformation of a polypeptide is fully described by the dihedral angles ϕ (involving backbone atoms $C_{i-1} - N_i - C_i^\alpha - C_i$) and ψ (involving backbone atoms $N_i - C_i^\alpha - C_i - N_{i+1}$) of each amino acid residue. Together with rotatable bonds within the side chains R, proteins have many degrees of freedom.

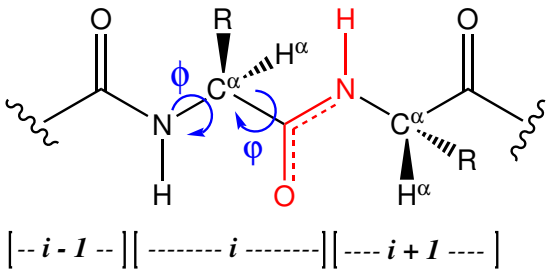

Figure 1.1: Polypeptide chain with the planar peptide bond connecting two amino acid residues marked in red. Dihedral angles ϕ and ψ of each amino acid residue define the peptide backbone conformation. R stands for one of the side chains of the 20 proteinogenic amino acids.

Under physiological conditions, the functional state of many polypeptides corresponds to a unique globular conformation with specific secondary and tertiary structure, termed the native state, while others are intrinsically unfolded. The native conformation of a

polypeptide is characterized by specific electrostatic interactions such as hydrogen bonds or salt bridges, hydrophobic contacts, and sometimes disulfide bonds. The hydrophobic residues are packed into the protein interior shielded form the aqueous environment. High or very low temperatures, extremes of pH, certain solutes such as urea and guanidine hydrochloride, or detergents cause destabilization of the native state which results in denaturation and loss of biological function [10]. *In vitro* denaturation and refolding experiments by Anfinsen and others have shown that at least for small polypeptides the amino acid sequence predetermines the native conformation, known as Anfinsen's dogma [11, 12]. It was also concluded from these experiments, that for most natural proteins the native state should correspond to a kinetically accessible global minimum of the free energy surface.

The mechanism of protein folding was already a matter of debate in the 1950s [13]. In 1968 Levinthal proposed that protein folding towards the native state is not a random process [14, 15]. Due to the large number of degrees of freedom even for small polypeptide chains a random search by adopting all possible conformations would take longer than the life time of the universe. This consideration is known as Levinthal's paradox. In contrast, *in vitro* folding is observed on the micro- to millisecond timescale. Consequently, Levinthal suggested, there must be folding intermediates and pathways [13]. In 1995 Wolynes and coworkers introduced the idea to describe the *in vitro* progression of an isolated polypeptide chain from an ensemble of denatured, random conformations to the native structure [16] by representing the free energy landscape by a *folding funnel* cartoon [17, 18]. The native state corresponds to a sharp, deep minimum in the free energy landscape and folding towards this conformation is assumed to be mainly driven by non-local hydrophobic interactions [10, 13, 19].

Spontaneous refolding to the native conformation has been observed *in vitro* for small (100 to 200 amino acids), globular, α-helix-rich proteins. In contrast, *in vitro* refolding experiments with larger, especially β-sheet-rich proteins resulted in low refolding yields and the formation of insoluble aggregates [16]. A number of *in vitro* and *in vivo* experiments lead to the conclusion that especially partly unfolded or misfolded polypeptide chains are prone to aggregation, in particular at high peptide concentrations [20, 21, 22, 23, 24]. Such partly unfolded conformations are populated under denaturing conditions as mentioned above. Also natural mutations that decrease the net charge or increase the hydrophobicity and β-sheet propensity of a polypeptide chain can result in the destabilization of the native state.

The competition between *in vitro* folding and aggregation of polypeptide chains can be illustrated by a simplified 2D free energy landscape represented by a *double funnel* cartoon as shown in Fig. 1.2 taken from Ref. [16]. It is important to mention, as also pointed out by Clark [16], that the double funnel cartoon does not attempt to describe the folding, misfolding and aggregation behavior of newly synthesized polypeptide chains

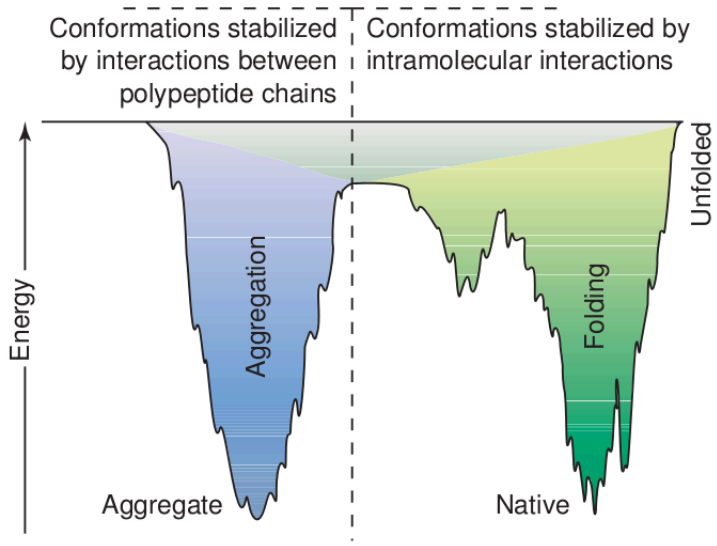

Figure 1.2: The competition between folding and aggregation of polypeptide chains *in vitro* illustrated by a simplified 2D *double funnel* representation of the free energy landscape of isolated *vs.* aggregated polypeptide chains. The picture was taken from Ref. [16].

released from ribosomes in the cell. In contrast to protein aggregates in reality which can contain many polypeptide chains stabilized by complex intermolecular interactions this representation is rather simple but useful in order to explain the general concept.

The right part of the diagram in Fig. 1.2 shows a folding funnel as a simplified 2D representation of the high dimensional conformational space accessible to an isolated polypeptide chain during folding. The width of the funnel corresponds to the chain entropy, i.e. the number of possible conformations. The broad top of the funnel renders the large number of denatured conformations while the narrow point at the bottom of the funnel corresponds to the unique native conformation. The y-axis relates to other energetic contributions such as the free energy of the polypeptide chain and the solvent, and the solvent entropy [16].

Starting from the ensemble of unfolded conformations the folding funnel allows several pathways to the global free energy minimum corresponding to the native structure. As the polypeptide chain adopts lower free energy conformations stabilized by intramolecular interactions, possibly a number of native contacts, intermediate states are populated. These are indicated by local minima along the sides of the folding funnel. These intermediate states can serve as kinetic traps that either promote folding or aggregation depending on their depth and the free energy barriers between the local minimum, the

amyloid disease	protein	native conformation
Alzheimer's disease	Amyloid β	unfolded
	τ protein	unfolded
Parkinson's disease	α-Synclein	unfolded
Chorea Huntington	Huntingtin (PolyQ)	largely unfolded
Type II diabetes	islet amyloid polypeptide	unfolded
senile systemic amyloidosis	wild-type transthyretin	all-β, prealbumin like
spongiform encephalopathy	Prion protein	partly unfolded, α-helical

Table 1.1: Selection of human diseases associated with extra- or intracellular amyloid deposits. The correlated proteins which are the major components of the fibrils and their monomeric native conformation are also given. Data were taken from Ref. [26].

native state and the *aggregation funnel* [16] shown in the left part of Fig. 1.2. Intermediates that expose a large hydrophobic surface to the solvent are highly prone to aggregation.

The aggregation funnel added on the left side of the diagram in Fig. 1.2 illustrates the interaction between several of such aggregation-prone conformations in a simplified 2D representation of the conformational space accessible to any kinds of aggregates. These protein aggregates are stabilized by electrostatic and hydrophobic intermolecular interactions resulting among other effects in a reduced hydrophobic surface area. The aggregation funnel might also contain intermediate states as shown for the folding funnel. As it relates to the interaction of several polypeptide chains the minimum in the aggregation funnel might correspond to an intersection of several free energy landscapes of individual polypeptide chains [16]. It is unclear if the minimum in the aggregation funnel corresponds to a true global minimum in the whole free energy landscape. However, this minimum is sufficiently kinetically trapped from the native state corresponding to the fact that protein aggregation often appears to be irreversible at least kinetically.

Cells have special quality-control mechanisms to prevent abnormal protein aggregation. *In vivo* partially unfolded or misfolded polypeptide chains are refolded to the native state by the help of molecular chaperones or degraded through the ubiquitin-proteasome pathway. If these processes fail the protein concentration increases and aggregation is favored [13, 25].

Aberrations in the folding process leading to aggregation of proteins can be linked to a wide range of human diseases. Many of these aggregation diseases are characterized by protein deposits in the form of insoluble amyloid fibrils [13]. Tab. 1.1 lists a few amyloid-related diseases associated with extracellular amyloid deposits or intracellular amyloid-like inclusions [26]. The involved protein and its native conformation are also given.

1.1.1 Structure of amyloid fibrils

Although amyloid fibrils can be formed by different polypeptides, the general structure of the fibrils is remarkably similar. Transmission electron microscopy (TEM) and atomic force microscopy (AFM) images indicate amyloid fibrils to be twisted and typically to consist of two to six laterally associated protofilaments [26] as shown by the structure model in the lower right corner of Fig. 1.4. A TEM image of amyloid fibrils formed by Aβ40 associated with Alzheimer's disease is shown in Fig. 1.3 (a). Here, red arrows indicate single protofilaments 6.5 ± 1.0 nm in width. Blue arrows mark other fibril morphologies with $10 - 15$ nm widths presumably due to lateral association of thinner filaments [27]. Individual protofilaments give a typical cross-β x-ray diffraction pattern similar to the schematic representation in Fig. 1.3 (b). The two main reflections correspond to the 4.8 Å spacing between hydrogen bonded β-strands oriented perpendicular to the fibril axis, and to the intersheet spacing of 5 to 15 Å depending on the involved side chain groups. This method cannot distinguish between parallel and antiparallel β-sheets. Circular dichroism (CD) and fourier transform infrared (FTIR) spectroscopy are used to monitor the secondary structure content; the latter method can distinguish between parallel and antiparallel as well as intra- and intermolecular β-sheets [28].

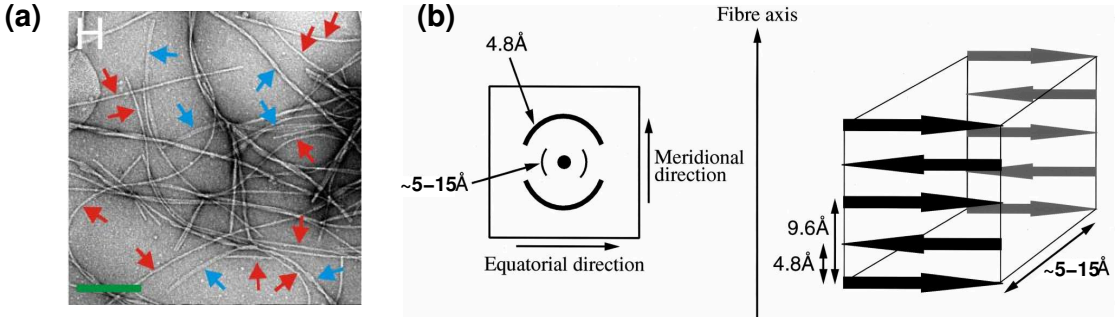

Figure 1.3: (a) TEM image of Aβ40 fibrils in the brain. Red arrows indicate the predominant fibril morphology, whereas blue arrows show other morphologies. The green scale corresponds to 400 nm. The picture is taken from Ref. [27]. (b) Schematic representation of the cross-β structure within amyloid fibrils determined by x-ray fiber diffraction. The method cannot distinguish between parallel and antiparallel β-sheets. The picture is taken from Ref. [29] and was modified.

The molecular fibril structure though depends on the protein involved. For instance, solid-state nuclear magnetic resonance (SSNMR) spectroscopy can be used to determine intra- and intermolecular ^{13}C distances [26]. Hydrogen/Deuterium exchange (H/D exchange) of amide protons monitored by nuclear magnetic resonance (NMR) facilitates the identification of residues involved in protective secondary structures [30].

Independent of the detailed fibril structure, amyloid fibrils bind to specific dyes such as Congo red (CR) and thioflavin T (ThT) which is detected by fluorescence spectroscopy. The interaction mechanism between the dyes and the amyloid structure however is still unclear.

1.1.2 Models for fibril formation

For many years it was assumed that the ability to form amyloid fibrils is limited to a small number of polypeptides with amino acid sequences encoding for the amyloid core structure [13]. In contrast, recent experiments suggest that amyloid formation might be a generic property of any polypeptide chain [31, 32, 33, 34]. Based on the amino acid sequence some proteins are more prone to aggregation than others. Under appropriate conditions amyloid formation was also observed for polypeptides not related to diseases such as myoglobin [35].

Fig. 1.4 summarizes the general knowledge of amyloid formation in a simplified representation. As mentioned above, partially or fully unfolded or misfolded conformations are more prone to aggregation than the native state. As shown in Tab. 1.1 a number of amyloidogenic polypeptides are natively unfolded, hence they are particularly vulnerable to aggregation. In the initial aggregation phase soluble oligomers of various different conformations, denoted as disordered aggregates in Fig. 1.4, are formed. These disordered aggregates might interact through relatively nonspecific interactions. Some of these early aggregation intermediates might dissociate again (off-pathway) while others, presumably β-sheet-rich species, reorganize and provide the nuclei for the amyloid structure (on-pathway) [26]. The latter then appear to transform into β-structured aggregates sometimes termed protofibrils or protofilaments. Possibly by lateral association such protofibrils are able to assemble into mature fibrils.

Degraded short polypeptide fragments are not necessarily excluded from the ability to aggregate as shown in Fig. 1.4. It will be discussed in Sec. 1.2.1 that Aβ is such an aggregation-prone degradation product.

The native conformation is less likely to aggregate. Nevertheless, at high protein concentrations the formation of amyloid fibrils through native-like aggregates which later reorganize towards the fibril structure is also observed for model proteins. Additionally, shown in Fig. 1.4, protein aggregation also leads to non pathogenic, functional aggregates such as myosin, actin filaments, or microtubules [26].

The kinetics of *in vitro* fibril formation can be measured, e.g. by detection of ThT binding using fluorescence spectroscopy. Often a lag phase is observed followed by a rapid exponential growth which is stopped when the aggregates are in equilibrium with the solution. If the solution is seeded with preformed fibrils the lag phase is shortened or even eliminated. Based on these observations it is widely believed that in many cases amyloid fibril formation proceeds by nucleated polymerization [36, 37, 38, 39].

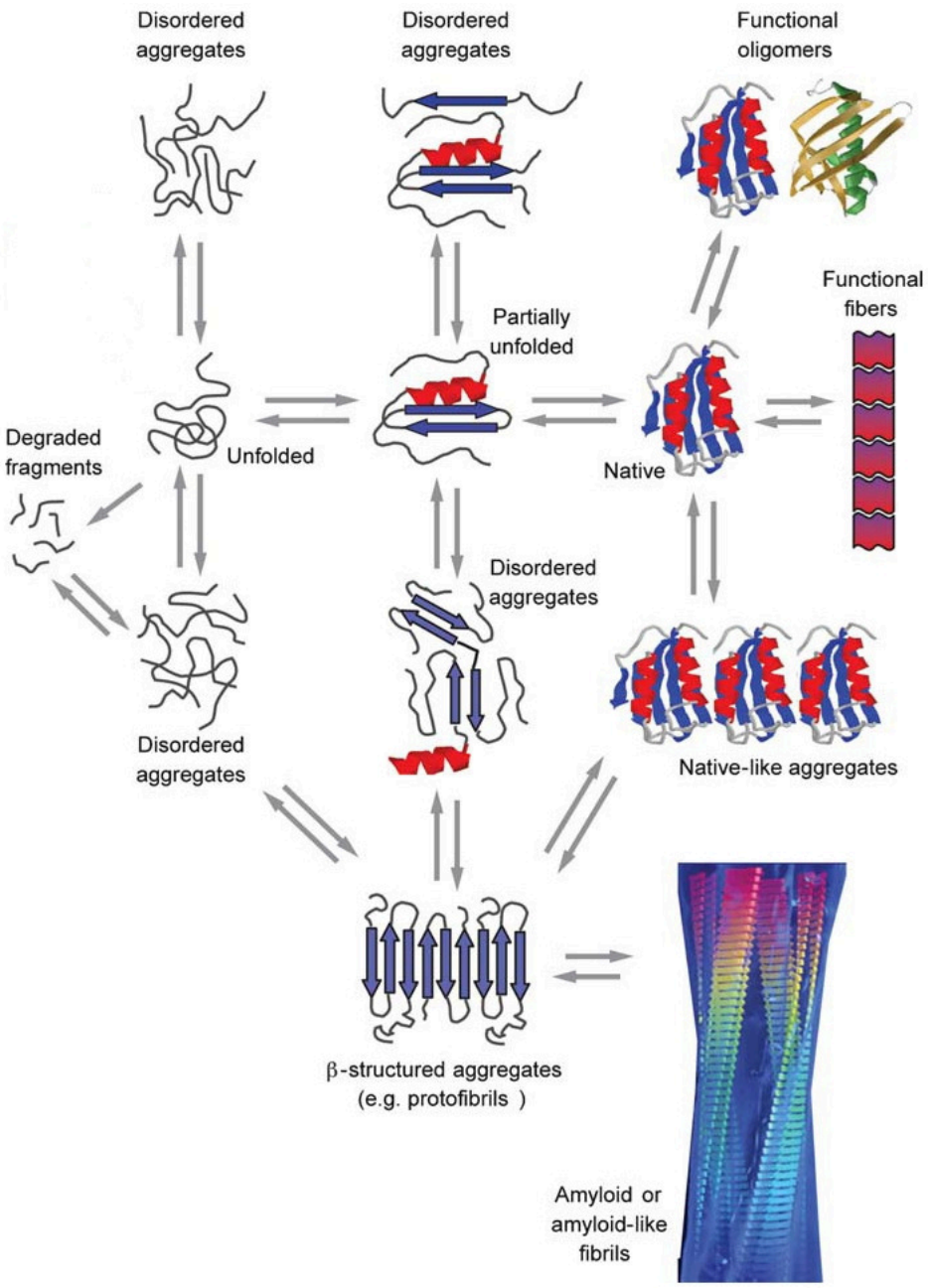

Figure 1.4: A schematic representation of the possible conformational states which can be adopted by individual polypeptide chains or several interacting chains. This diagram gives an overview of possible transitions between those conformations that might lead to the formation of amyloid fibrils. The picture is taken from reference [26] and was modified.

The lag phase is characterized by various disordered oligomeric aggregates, see Fig. 1.4 and corresponds to the time required to form a critical nucleus. The critical nucleus is the most transient and highest free energy species in the pathway. The size of the critical nucleus depends on the number of molecules required to compensate the loss of translational entropy by favorable interaction energy. Corresponding to the various number of different oligomers appearing within the lag phase, different fibril morphologies are possible. Depending on the experimental conditions one or the other morphology might be preferred.

Recent *in vitro* and *in vivo* experiments on the aggregation of Huntingtin related polyQ-containing proteins suggest that amyloid formation might follow a complex multistage mechanism. This aggregation model is based on nucleated polymerization while aggregation proceeds in substeps directed by prefibrillar oligomers. It was found that oligomers formed in the initial step contained exposed polyQ segments which presumably trigger the second aggregation step in which the polyQ-containing segments reorganize to form the amyloid core [40, 41].

For some proteins initial aggregation appears to be a downhill process. This was observed, for instance, for amyloid formation of a mutant of transthyretin under partially denaturing conditions and at certain conditions for human serum albumin [42, 43]. In this aggregation model, the monomeric state has the highest free energy, aggregation proceeds without a lag phase, and is not influenced by seeding with protofibrils.

1.1.3 Toxic oligomers

Within the last years a number of experiments suggested that not the mature fibrils but the early aggregation intermediates, in the form of soluble, low molecular weight (LMW) oligomers, are the main toxic components in amyloidogenic diseases [3, 4, 5, 6, 7, 8, 9]. In contrast, the formation of mature fibrils might be an evolutionary response to remove these toxic species. In order to develop pharmaceutic agents to cure amyloidogenic diseases, it becomes crucial to identify all conformational states involved in the aggregation process. Especially, conformations of the toxic LMW oligomers and the thermodynamics of the transitions between different oligomeric conformations are of major interest.

The macroscopic dimension and shape of oligomers can be visualized using TEM and AFM [44, 45, 46]. The size distribution can be determined by dynamic light scattering (DLS) and the number of molecules within an oligomer can be obtained by sodium dodecyl sulfate polyacrylamide gel electrophoresis (SDS-PAGE) [47]. Additionally, CD and FTIR spectroscopy can be applied to determine the secondary structure content [47].

In contrast, the molecular structure of LMW oligomers is often difficult to access experimentally due to their disordered and transient nature. Consequently, for many amyloid peptides including Aβ the structural and biological characteristics of oligomeric structures remain unclear [48]. Theoretical models such as atomistic MD simulations

can be used to predict the molecular structure of LMW oligomers.

1.2 Alzheimer's disease

Alzheimer's disease is a severe neurodegenerative disease which mostly affects people more than 65 years of age. With rising life expectancy this disease will become a serious problem for future generations. According to estimations by the World Health Organization (WHO) and Alzheimer's Disease International (ADI) in 2050 over 115 million people worldwide will be affected by AD.

The disease is characterized by widespread death of neurons and disruption of synaptic functions which cause the loss of memory and mental ability [1]. In the beginning the hippocampus is affected corresponding to an area responsible for short time memory. In late stages most of the cortex is damaged and the ability to communicate and to recognize familiar people or environments is entirely lost [49].

1.2.1 Molecular basis

Histopathologically, AD is characterized by neurofibrillary tangles of τ protein inside neurons and extracellular amyloid deposits of Aβ in the brain [50]. The latter are termed senile plaques, and were first described in 1907 by Alois Alzheimer, a German psychiatrist [51]. Although both molecular hallmarks are associated with AD it yet remains unknown whether and how they are related. The following paragraphs discuss the origin of both peptides.

Microtubules are one of the active matter components of the cytoskeleton in neurons. The τ protein is primarily expressed in neurons and stabilizes microtubules by interacting with the tubulin dimer, the polymer building block of microtubules. In AD infected brains, the τ protein is abnormally hyperphosphorylated, dissociates from the microtubules, and aggregates to neurofibrillary tangles of paired helical filaments and (only *in vitro*) straight filaments [50]. Dissociation of τ destabilizes the microtubules and causes their disintegration. The combination of these processes inhibits neuronal functionality and might also account for the loss of neurons.

The Aβ peptide is cleaved from the C-terminal region of the amyloid precursor protein (APP), a type I membrane-spanning glycoprotein. APP consists of 695 to 770 amino acids [52]. It is expressed in many tissues but concentrated in neurons, where it localizes in the plasma membrane, the trans-Golgi network, the endoplasmatic reticulum and in endosomal, lysosomal, and mitochondrial membranes [48]. The function of APP is not exactly clear, yet. The schematic representation in Fig. 1.5 shows the location of APP in the plasma membrane where proteolytic cleavage takes place. A short C-terminal end points into the cytoplasm, while a large N-terminal domain is exposed into the extracellular matrix. Abnormal cleavage of APP by β-secretase at the N-terminal end

and γ-secretase at the C-terminus yields the pathogenic Aβ peptide, see the right box in Fig. 1.5. In the normal non-amyloidogenic degradation pathway, APP is cleaved by α-secretase instead of β-secretase. The α-secretase cleaves APP closer to the C-terminus than β-secretase does, see the left box in Fig. 1.5. The remaining fragment can additionally be cleaved by γ-secretase as well resulting in the formation of the non-pathogenic fragment P3 (not shown).

Recent studies with transgenic mice and human patients indicate that Aβ can also accumulate intraneuronally, presumably preceding the formation of extracellular Aβ deposits [52]. It is yet unclear how intracellular Aβ contributes to the disease progression.

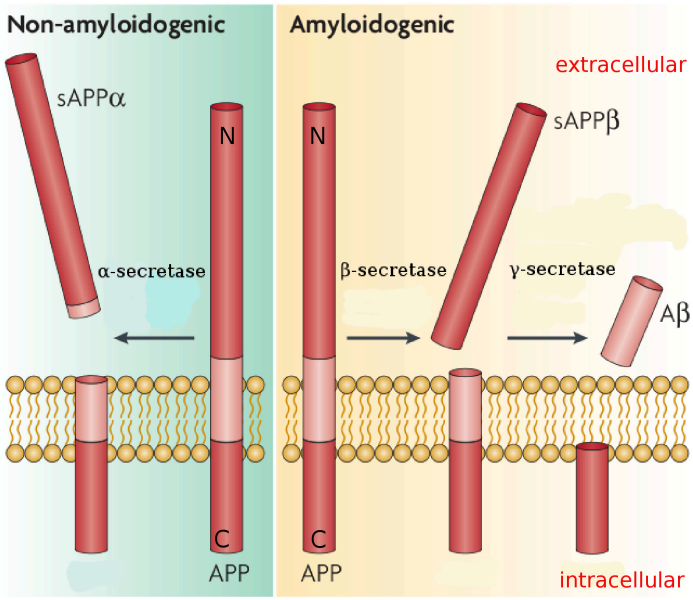

Figure 1.5: Schematic representation of the non-amyloidogenic and the amyloidogenic cleavage of APP located in the plasma membrane. The amyloidogenic pathway results in the release of the pathogenic Aβ peptide. The picture is taken from Ref. [52] and was modified.

In general, AD is not inheritable. Only approximately 5 % of the patients suffer from Familial AD. In combination with Familial AD three genes were detected, which all affect the generation of Aβ. These genes code for APP, as well as for the γ-secretase subunits presenilin 1 and presenilin 2 [53]. Apart from these cases, only one risk gene, apolipoproteinE-ϵ4 (ApoE-ϵ4) was identified to increase the probability to develop AD [1].

Full length Aβ: Aβ42 and Aβ40

The cleavage site of the γ-secretase is not precise and causes the release of Aβ fragments with 39 to 43 amino acids in length. The most abundant in amyloid deposits are Aβ40 and Aβ42 in a ratio of 10:1 while Aβ42 is significantly more neurotoxic and the main component of senile plaques [1, 26]. The amino acid sequence of human Aβ42 is given in Fig. 1.6. The peptide is amphiphilic, with a central hydrophobic region at residues L17 – A21 and a hydrophobic C-terminal tail starting at residue G29.

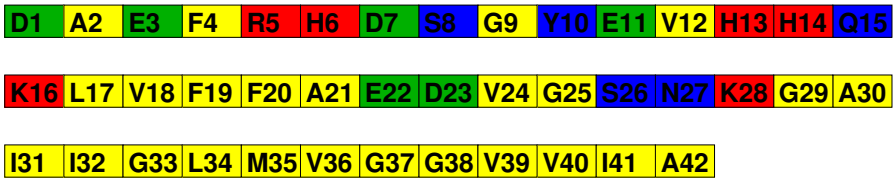

Figure 1.6: Amino acid sequence of full length Aβ42. Nonpolar residues are colored in yellow, whereas polar residues are blue, basic residues are red, and acidic residues are green.

Up to date, a vast number of *in vitro* and *in vivo* studies concerning the amyloid formation of Aβ have been published. For instance, the monomeric structure of both fragments was studied in aqueous solution by NMR. While both peptides are mostly unstructured, Aβ42 shows a decreased flexibility for residues I32 to A42 compared to Aβ40 [54, 55].

Many types of natural and synthetic Aβ oligomers of different sizes and shapes have been reported, which accounts for their biological and structural diversity [48]. However, the molecular structures of Aβ40 and Aβ42 LMW oligomers remain unknown. A promising approach seems to be the use of conformation-dependent antibodies. These studies indicate that structurally different variants may even exist among oligomers with similar morphology [48]. In a recent work two antibodies specific either for oligomers (A11) or fibrils (OC) were used to recognize LMW oligomers [56]. Based on the results of this study the appearance of two types of oligomers was proposed: prefibrillar (A11+/OC-) and fibrillar (A11-/OC+). Interestingly, the A11 antibody also recognizes oligomers from various other proteins such as α-synclein, islet amyloid polypeptide, polyglutamin (PolyQ), lysozyme, human insulin and prion peptide (106-126) suggesting that prefibrillar oligomers could share a common structure regardless of their amino acid sequence [26, 48, 57].

Concerning mature fibrils, both Aβ peptides show distinct fibril morphologies. Based on SSNMR, x-ray fiber diffraction and electron microscopy (EM) experiments both peptides adopt a β-strand-turn-β-strand motif within fibrils while its location along the amino acid sequence differs. In Aβ40, residues V12 – V24 and A30 – V40 form two inter-

molecular parallel β-sheets perpendicular to the fibril axis, while residues G25 – G29 are bent [58, 59]. In Aβ42, the β-strand-turn-β-strand motif involves residues V18 – A42, with residues N27 – A30 in the turn [60].

Shorter fragments: Aβ(25-35) and Aβ(10-35)

Besides the full length peptides various shorter fragments of Aβ are studied (i) because some of these also appear in small amounts in AD brains, (ii) in order to determine residues essential for aggregation and neurotoxicity, and (iii) because all amyloidogenic polypeptides might share a common structure motif in the oligomeric state. The present study focuses on two fragments, Aβ(25-35) and Aβ(10-35).

Containing 11 residues, Aβ(25-35) is the shortest fragment of Aβ which forms β-sheet-rich fibrils and exhibits the toxicity of the full length peptide [4, 61, 62]. The conformations of the preaggregated state in 80:20 and 20:80 (vol/vol) hexafluoroisopropanol (HFIP)/water mixtures have been solved by NMR [63]. The peptide was found to adopt an α-helical conformation in the HFIP-rich mixture, whereas it is mostly unstructured with a type I β-turn centered on residues S26 and N27 in the water-rich mixture. The monomer conformation in pure water is difficult to access because at concentrations necessary for analysis the peptide strongly aggregates. Replica exchange molecular dynamics (REMD) simulations of the peptide in a 80:20 HFIP/water mixture yielded an α-helical conformation similar to the experimental structure. An analog simulation in pure water predicted that prior to aggregation Aβ(25-35) exists as collapsed coils in equilibrium with β-hairpin conformations [62].

H/D exchange measurements monitored by NMR suggest that within Aβ(25-35) fibrils peptides form either out-of-register antiparallel or in-register parallel β-sheets presumably involving residues K28 – M35 [64]. At neutral pH and room temperature an AFM study observed two distinct fibril morphologies with diameters of 3.58 ± 1.53 nm and 1.41 ± 0.48 nm, respectively [65]. Peptides are assumed to be either fully extended or somehow bent within these fibrils. At the time this project started, there were neither oligomeric structures available from experiments nor existed any theoretical study that determined oligomeric states based on spontaneous aggregation.

The Aβ(10-35) fragment includes the self-recognition site of Aβ, K16 – F20. Peptides containing these residues were found to bind Aβ40 and prevent the formation of amyloid fibrils [66]. This region of Aβ was also determined to be a binding site for several ligands [67, 68, 69, 70]. The conformation of monomeric Aβ(10-35)-NH_2 in water at pH 5.6 has been solved by NMR. Structural calculations based on observed nuclear Overhauser effect (NOE) correlations and ${}^3J_{\mathrm{H^N H^\alpha}}$ scalar coupling constants suggest that the peptide adopts a collapsed coil conformation containing a well-structured central hydrophobic cluster involving residues L17 – A21 [54, 71].

EM images of Aβ(10-35)-NH_2 fibrils formed at neutral pH show twisted pairs of

single filaments with varying periodicities of the twist. The fibril diameters vary from 5.5 ± 1.0 nm at the narrowest point to 10.5 ± 1.0 nm at the widest point [72]. Intermolecular ^{13}C distances observed by SSNMR spectroscopy suggest that peptides form in-register parallel β-sheets while individual peptides are assumed to be fully extended [73, 74, 75, 76]. A more recent study indicates that the peptides are bent with some residues in region D23 – G29 in a non-β-strand conformation [72]. Due to the lack of experimental structures, different theoretical approaches were applied to study oligomeric conformations of Aβ(10-35)-NH_2. These studies either use simplified solvent descriptions or study the stability of pre-generated aggregates [77, 78, 79, 80].

1.2.2 Neurotoxicity of Aβ

The AD infected brain is characterized by a peculiar inflammation initiated by Aβ. The neurotoxic effect of the peptide and its oligomers is associated with several processes including oxidative stress, pore formation and damage of endothelial cells [1]. In combination with metal ions, e.g. Cu(II) or Zn(II), and oxygen Aβ generates reactive oxygen species (ROS) which cause lipid peroxidation, protein oxidation, and nucleic acid oxidation, all resulting in cell death [53]. A secondary mechanism for toxicity is correlated to the ability of Aβ oligomers to form ion-permeable pores in membranes. These pores allow an unregulated flow of ions, e.g. Ca^{2+}, in and out of the cell causing cellular dysfunction [5, 81, 82].

1.2.3 Drug design

AD was first diagnosed more than hundred years ago and is still incurable. Current medication only treats symptoms of the disease but cannot prevent the loss of neurons. There exist two types of pharmaceutical agents (i) cholinesterase inhibitors, and (ii) memantine. The first enhance the concentration of neurotransmitters by inhibiting their degradation by cholinesterase. Memantine blocks NMDA receptors for binding of glutamate which is released by damaged cells in order to accelerate cell damage [49].

Research for future drugs mainly follows two strategies (i) prevent the production of pathogenic Aβ and τ protein, i.e by deactivation of β-secretase cleavage [83], and (ii) inhibit aggregation of Aβ e.g. by small molecules (antibodies) that target the self-recognition region of Aβ or the toxic oligomers to mark them for degradation. For the latter approach, a detailed knowledge about the molecular structure of the preaggregated state and early aggregation intermediates is necessary.

1.3 Objectives and questions

In this work, two fragments of the Aβ peptide, Aβ(25-35) and Aβ(10-35), are studied by means of molecular dynamics simulations. In particular, the preaggregated monomeric state and early aggregation intermediates such as dimers and trimers are simulated. To model the peptide-water interactions as accurate as possible a fully atomistic description was chosen for peptides and solvent. As was previously discussed, early aggregation intermediates in amyloid formation are of disordered nature. Consequently, the free energy landscape of such a system can be assumed to be rather broad and rough containing many local minima. To achieve sufficient sampling of conformational space and to avoid kinetic trapping in local minima, replica exchange molecular dynamics simulations were performed for each system over several hundred nano seconds.

For each fragment the preaggregated, monomeric state in water was studied. Simulations of Aβ(25-35) were performed in order to check if the β-hairpin conformation observed at neutral pH and room temperature in a previous theoretical study [62] can be reproduced by starting from a different unbiased configuration. Simulations of monomeric Aβ(10-35)-NH_2 starting from a fully extended configuration were conducted with the aim to test if the NMR-derived collapsed coil conformation at pH 5.6 and 283 K [54, 71] is also reached by simulations. This was done by testing the performance of two different force fields, GROMOS96 43a1 and OPLS/AA, and by comparing experimental NMR data such as NOE distances and ${}^3J_{\mathrm{H^N H^\alpha}}$ coupling constants with the corresponding quantities back-calculated from the simulations.

To study oligomeric states, simulations were performed for Aβ(25-35) dimers and trimers, and Aβ(10-35)-NH_2 dimers, all at neutral pH. Here, several questions were of interest. How large is the structural variety of aggregates at the same oligomeric state, i.e dimers? Can these various conformations be somehow classified, i.e. by an appropriate reaction coordinate or by structural similarities to the monomeric or the (assumed) fibril structure? The latter question addresses the proposed existence of prefibrillar and fibril-like oligomers. Finally, if conformational substates within a dimer or trimer ensemble can be defined the question is, what mediates transitions between the different conformations? Can we determine specific intermolecular interactions or thermodynamic forces dictating the transitions?

Because standard REMD does not provide the dynamics of the system, the kinetics of dimerization and trimerization could not be studied. Nevertheless, a comparison of structural and thermodynamic properties of the individual ensembles of Aβ(25-35) monomers, dimers and trimers has been applied in order to obtain qualitative informations about the aggregation process.

Chapter 2

Molecular Dynamics Simulation and Analysis Methods

The MD simulation method is used to describe the time dependent behavior of a molecular system. Nowadays, it is often employed to study conformational changes, dynamics and thermodynamic properties of biomolecules such as proteins or nucleic acids. It can give detailed information on molecular processes which can be difficult to access in experiment.

Molecules can be described as individual atoms (atomistic) or groups of interacting atoms (coarse grained level). The solvent can also be treated on different levels, i.e. by using an explicit (atomistic) or an implicit (continuum) description. Both characterizations have advantages and disadvantages. While the atomistic description is more accurate, it is computationally more expensive. Within the last fifty years, computational power has increased significantly. Now, atomistic MD simulations can be routinely applied to systems containing up to a million atoms over several nanoseconds [84]. The use of parallel processors even allows simulations of typical middle-sized proteins over microseconds. However, this is not yet sufficient to describe realistic folding or even protein aggregation [84].

Additionally, complex molecular systems are described by many degrees of freedom. Their conformational space corresponds to a high dimensional free energy surface containing many local minima. This makes complete conformational sampling an impossible task. To overcome this problem, several enhanced sampling techniques such as the replica exchange method [85] or umbrella sampling [86] were developed. These methods have the disadvantage to generate artificial dynamics and can be very expensive for large systems.

In the present work, replica exchange molecular dynamics simulations were performed to study monomers and small oligomers of Aβ(25-35) and Aβ(10-35)-NH_2 in aqueous solution. To observe conformational changes within the peptides and to model the

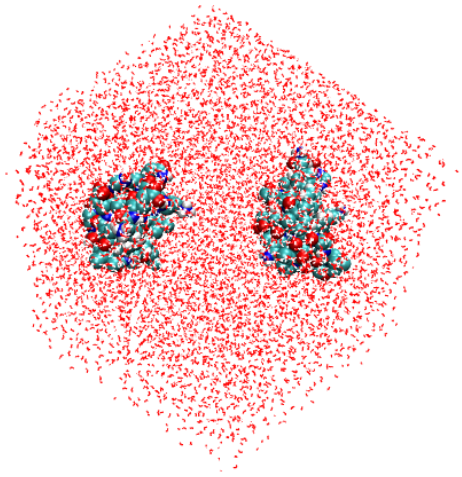

Figure 2.1: Initial configuration for simulations of Aβ(10-35)-NH_2 dimers in water. Peptide atoms are represented as spheres and water molecules are shown in stick representation. C atoms are colored turquoise, O atoms red, N atoms blue, and H atoms white.

peptide-water interaction as accurate as possible we chose a fully atomistic description for peptides and solvent. The modeled systems then contained between 18,000 to 24,000 atoms. The general simulation setup is shown for the Aβ(10-35)-NH_2 dimer system in Fig. 2.1. Here, two peptides are placed in a simulation box with random orientation to each other. The remaining space is filled with water molecules and if necessary with a certain number of counter ions to neutralize the system.

This chapter will give an introduction to the general principles of MD simulations while the focus is on techniques applied to the modeled systems. The first two sections discuss how particle interactions are handled. Sec. 2.3 then focuses on the most important algorithms necessary to describe the time dependent behavior of a many-particle system. The free energy landscape of early aggregation intermediates of amyloidogenic polypeptides are assumed to be rather broad and rough containing many local minima. In order to avoid kinetic trapping in local minima and achieve sufficient conformational sampling we applied replica exchange molecular dynamics simulations. The basics of this enhanced sampling method will be explained in Sec. 2.4. Prior to a MD simulation the initial configuration as shown in Fig. 2.1 requires an energy minimization which will be discussed in Sec. 2.5. Finally, Sec. 2.6 focuses on the analysis of the MD trajectories, and explains the calculation of often used equilibrium properties. All simulations were performed with the GROMACS software package 3.3 [87].

2.1 Principle

In MD a many-particle system is described by interactions between classical point masses. In order to do so three approximations are necessary. The most exact description of a molecular many-particle system evolving in time is given by the time-dependent Schrödinger equation [88]. The combined motion of nuclei and electrons is given by a time-dependent wave function. Since, an electron is about four orders of magnitude lighter than a nucleus, the motion of both can be decoupled. This approximation is called the Born-Oppenheimer approximation [89]. It allows to separate the wave function of a molecule into its time-dependent nuclear and time-independent electronic components.

In the second approximation, the nuclei are treated as classical point masses, i.e. atomic positions. To describe the motion of N interacting atoms the Schrödinger equation is replaced by Newton's equations of motion

$$m_i \frac{d}{dt} \mathbf{r}_i = \mathbf{p}_i, \tag{2.1}$$

$$m_i \frac{d^2}{dt^2} \mathbf{r}_i = \mathbf{f}_i, \tag{2.2}$$

where $\mathbf{r}_i$, $\mathbf{p}_i$, and m_i denote the position, momentum, and mass of atom i, with $i = 1, ..., N$. The force $\mathbf{f}_i$ acting on atom i is given by

$$\mathbf{f}_i = -\nabla_r \, E_e(\mathbf{r}_1, ..., \mathbf{r}_N), \tag{2.3}$$

where $E_e(\mathbf{r}_1, ..., \mathbf{r}_N)$ is the effective potential arising from the electronic ground state energy for given nuclei positions. The classical description holds for most atoms at room temperature but breaks down for light atoms as hydrogen and at low temperatures. For example, the transfer of a proton over a hydrogen bond cannot be described properly without quantum mechanics [90].

In the third approximation, the motion of the electrons is neglected and the effective potential E_e is described by a semi-empirical interaction potential denoted as force field. This final simplification allows to compute the time evolution of systems comprising up to several 10^6 atoms. In turn, electron transfer as in chemical reactions or excited states cannot be treated, as well as the polarizability of atoms. The following section discusses how atomic interactions are treated by semi-empirical force fields.

2.2 Force fields

Force fields describe molecular interactions as a sum of covalent (E_{cov}) and noncovalent van der Waals (E_{LJ}) and electrostatic (E_{coul}) interactions

$$E_{\mathrm{tot}} = E_{\mathrm{cov}} + E_{\mathrm{LJ}} + E_{\mathrm{coul}}. \tag{2.4}$$

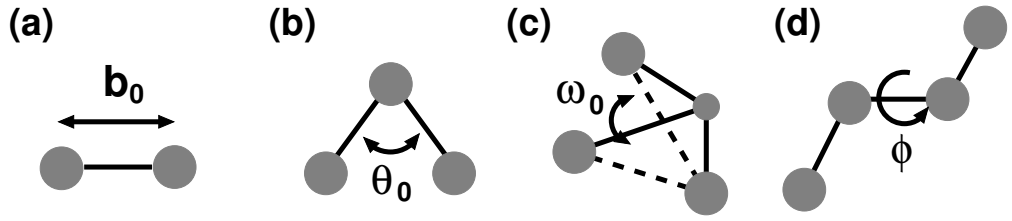

Figure 2.2: Basic covalent interactions combined in force fields; (a) bond stretching, (b) bond angle vibration, (c) improper dihedral angles (e.g. out-of-plane deflections of aromatic rings), and (d) torsion of bonds (proper dihedral angle). Lines correspond to covalent bonds. Dotted lines in (c) are drawn to define planes, but do not correspond to covalent bonds.

The covalent interactions include bond stretching ($E_{\rm b}$), bond angle vibrations ($E_{\rm ang}$), out-of-plane deflections of aromatic rings ($E_{\rm imp}$), and torsion of bonds ($E_{\rm dih}$), as shown in Fig. 2.2. The stretching of a covalent bond of length b, the vibration of a bond angle θ, and the deflection of two planes by an angle ω are described by harmonic potentials of the form

$$E_{\rm i} = \frac{1}{2}\, K_i (i - i_0)^2. \tag{2.5}$$

Here, i stands for the bond length b, or the angle θ or ω, i_0 for the corresponding equilibrium values (b_0,θ_0,ω_0), and K_i for the harmonic force constants (K_b,K_θ,K_ω). The torsion of a bond is described by the rotation around the dihedral angle ϕ as shown in Fig. 2.2 (d), and given by

$$E_{\rm dih} = \frac{1}{2}\, K_\phi \left[1 + \cos(n\phi - \delta)\right], \tag{2.6}$$

with the periodicity $n = 1, 2, ...$, and the phase shift δ.

Noncovalent interactions as the repulsion resulting from the Pauli exclusion principle which prevents the collapse of molecules, and the attraction due to dispersion, are summarized as *van der Waals* interactions. The van der Waals interaction between two atoms i and j is described by the Lennard-Jones potential [91]

$$E_{\rm LJ} = \frac{C_{ij}^{(12)}}{r_{ij}^{12}} - \frac{C_{ij}^{(6)}}{r_{ij}^{6}}. \tag{2.7}$$

The parameters $C_{ij}^{(12)}$ and $C_{ij}^{(6)}$ depend on the interacting atom types. Electrostatic interactions are described by the Coulomb potential

$$E_{\rm coul} = \frac{1}{4\pi\epsilon_0}\frac{q_i q_j}{\epsilon_r r_{ij}}, \tag{2.8}$$

where, two atoms of charge q_i and q_j a distance r_{ij} apart interact with each other. The symbol ϵ_0 denotes the dielectric constant, and ϵ_r the relative dielectric constant. In this work, nonbonded interactions, especially electrostatic interactions due to their long-range character, are treated using cutoff combined with continuum methods, as described in Sec. 2.3.5.

The force field parameters such as average bond lengths, angles, force constants, van der Waals parameters, and partial charges are obtained from crystal structures, infrared (IR) spectra, free energies of solvation, and quantum chemical calculations. The parametrization of the force fields is done for small molecules which serve as building blocks for larger molecules. In case of proteins the force fields are optimized for individual amino acids and small peptides [90].

2.2.1 Force fields used for peptides

In the present study, two force fields developed to perform protein dynamics in an explicit aqueous environment were used, GROMOS96 43a1 [92] and OPLS/AA [93]. Both force fields are optimized based on different experimental parameters and therefore, use slightly different descriptions of interaction potentials. For example, in the OPLS/AA force field the energy of proper dihedrals is described by a Ryckaert-Bellemans function [90] rather than the periodic function (Eq. 2.6) used in GROMOS96 43a1. Also the nonbonded 1,4 interactions, between the first and fourth atom in Fig. 2.2 (d), is scaled differently in both force fields. One important difference in terms of computational efficiency, is the use of united atoms in GROMOS96 43a1. Here, CH_i $(i = 1, 2, 3)$ groups are merged into compound atoms with respective total mass, adapted partial charges and van der Waals radii. On the other hand, OPLS/AA is an all atom force field.

2.2.2 Force fields used for water

In all simulations water was used as solvent and described in atomic resolution. Simple models treat the water molecule as a rigid body interacting only through non-bonded interactions. The SPC 3-site water model assigns a point charge to each atom and assumes the HOH-angle to be 109.47° as in an ideal tetrahedron instead of the observed 104.5° [94, 95]. In the TIP4P water model a dummy site is introduced near to the oxygen, which improves the electrostatic distribution around the water molecule [96]. For all simulations the SPC water model was used in combination with the GROMOS96 43a1 force field, and the TIP4P model with the OPLS/AA force field.

2.3 Computing trajectories

A basic flow scheme for MD is given in Fig. 2.3. Each simulation requires as input the interaction potential (i.e. the force field and its parameters) and the initial coordinates of all atoms in the system. The initial velocities of all atoms are randomly chosen according to a Maxwell-Boltzmann distribution. In the second step of the MD algorithm, the force acting on each atom is calculated as the negative gradient of the interaction potential (Eq. 2.3). Sometimes the positions of individual atoms are restrained as will be discussed in Sec. 2.3.4. In step 3 of the MD algorithm, the movement of the atoms is simulated by numerically solving Newton's equations of motion in small time steps Δt using the Leap-Frog algorithm which will be described in Sec. 2.3.1. To approximate realistic behavior a number of tricks are applied in MD. Among these, the use of periodic boundary conditions, thermostats and barostats are outlined in Sec. 2.3.2 and 2.3.3. As shown in Fig. 2.3 steps 2 and 3 are repeated for the required number of time steps Δt, and finally the trajectory containing the positions and velocities of all atoms including energies, pressure, temperature etc. are written out. In order to reach nanosecond time scales in reasonable real time, a number of approximations are made which are discussed in Sec. 2.3.5.

2.3.1 Integration algorithm

In MD simulations Newton's equations of motion (Eq. 2.1 and 2.2) are solved for discrete time intervals Δt using an integration algorithm. Such algorithms are based on Taylor expansions of positions, velocities or further derivatives.

The GROMACS MD program applies the leap-frog algorithm [97], which is reversible in time as the equations of motion. It is fast and requires only little memory storage. It uses the atom positions $\mathbf{r}_i$ at time t and velocities $\mathbf{v}_i$ at $(t + \Delta t/2)$. Positions and velocities are updated using the forces $\mathbf{f}_i$ at time t

$$\mathbf{v}_i(t + \frac{\Delta t}{2}) = \mathbf{v}_i(t - \frac{\Delta t}{2}) + \frac{\mathbf{f}_i(t)}{m_i}\Delta t, \tag{2.9}$$

$$\mathbf{r}_i(t + \Delta t) = \mathbf{r}_i(t) + \mathbf{v}_i(t + \frac{\Delta t}{2})\Delta t. \tag{2.10}$$

In order to integrate the equations of motion with reasonable accuracy, the maximum time step Δt should be small compared to the period of the fastest vibrations within the system. Using constraints and other approximations which will be discussed in Sec. 2.3.5, a time step of 4 fs can be used for all simulations.

2.3.2 Periodic boundary conditions

Considering a system containing up to 10^6 atoms as an isolated cluster would result in errors caused by artificial surface effects [98]. Therefore, in the present study periodic

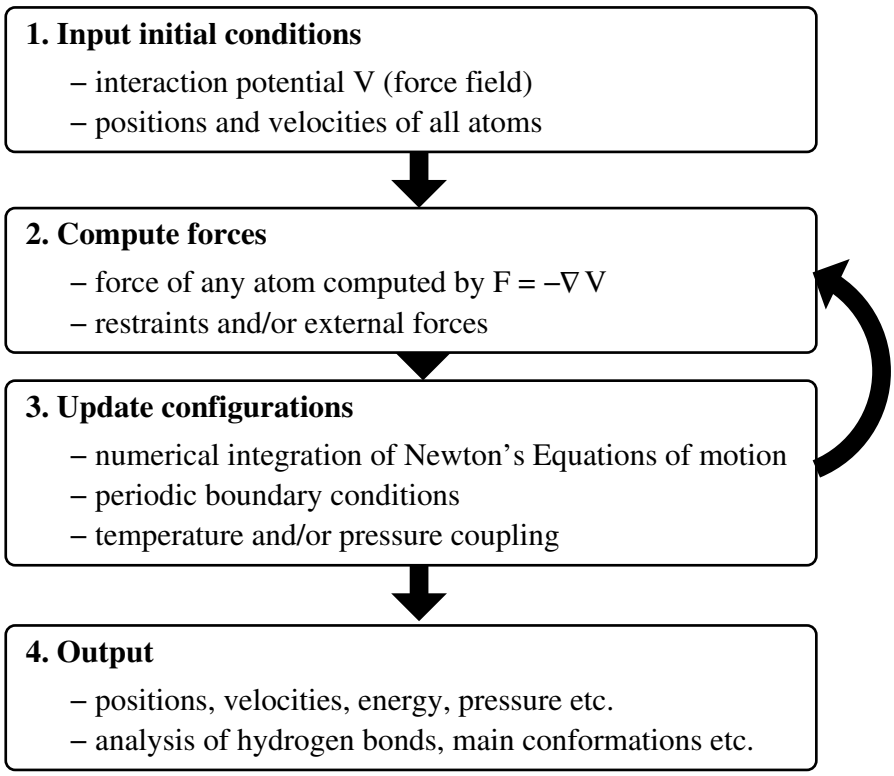

Figure 2.3: The global MD algorithm.

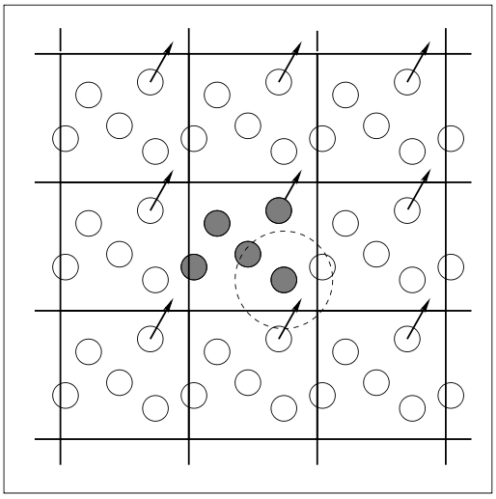

Figure 2.4: Periodic boundary conditions. If one particle moves out of the simulation box it is replaced by its image. The picture is taken form Ref. [98].

boundary conditions were applied as illustrated by the two dimensional sketch in Fig. 2.4. The simulation box is surrounded by translated copies of itself in all directions. Essentially, if one particle leaves the simulation box it is replaced by its image particle. In combination with periodic boundaries the minimum image convention is used. It implies that each atom interacts only with the nearest periodic image of another given atom. Additionally, the cutoff distance chosen for the truncation of nonbonded interactions must be smaller than half the shortest box vector.

GROMACS supports several box types, e.g. rhombic dodecahedron and truncated octahedron. These box shapes are closer to a sphere than to a cube. They require less water molecules to fill the remaining space around the peptide and are therefore more economical in terms of computational efficiency [90]. Both box types were used in the present study.

2.3.3 Temperature and pressure coupling

During an MD simulation, the temperature can be controlled by coupling the system to an external heat bath. The coupling can be managed by rescaling the velocities or introducing a friction term into the equations of motion. The latter refers to the Nosé-Hoover thermostat which produces an oscillatory relaxation of the temperature towards the reference temperature [99, 100].

In this work, the weak coupling Berendsen scheme is used which follows the minimal perturbation approach by rescaling the velocities [101]. It enforces a strongly damped relaxation of the temperature T towards the reference temperature T_0. The temperature

deviation from T_0 decays exponentially as given by

$$\frac{dT}{dt} = \frac{T_0 - T}{\tau}, \tag{2.11}$$

with the time constant τ corresponding to the strength of the coupling. To enable heat flow in and out of the system, the velocities of all atoms are rescaled at every time step. The rescaling factor λ is given by

$$\lambda = \left[1 + \frac{\Delta t}{\tau_T}\left(\frac{T_0}{T(t - \frac{\Delta t}{2})} - 1\right)\right]^{\frac{1}{2}}, \tag{2.12}$$

where the instantaneous temperature T is determined at $(t - \Delta t/2)$ according to the leap-frog algorithm (Sec. 2.3.1). The parameter τ_T is correlated to the time constant τ of the temperature coupling by

$$\tau = \frac{2C_V \tau_T}{N_{\mathrm{df}} k_B}, \tag{2.13}$$

where C_V is the total heat capacity of the system, N_{df} denotes the total degrees of freedom, and k_B the Boltzmann constant. The difference between τ and τ_T occurs because the change in kinetic energy due to the rescaling of the velocities is partly redistributed between kinetic and potential energy [90]. In all simulations peptides and solvent were separately coupled to an external heat bath using the Berendsen thermostat with a relaxation time of 0.1 ps.

For equilibration purposes, a short MD simulation at isobaric conditions was performed prior to a REMD run. The pressure was controlled with the weak coupling Berendsen scheme. Similar to the Berendsen thermostat, the so-called barostat induces a first-order kinetic relaxation on the pressure P towards the reference pressure P_0.

$$\frac{dP}{dt} = \frac{P_0 - P}{\tau_P}. \tag{2.14}$$

In all simulations were pressure coupling was applied, the coupling constant τ_P set was to 1 ps and P_0 to 1 bar. The pressure of the system is kept constant by rescaling the coordinates and box vectors, i.e. the box volume, at every time step. For isotropic systems the rescaling factor μ is given by

$$\mu = 1 - \frac{\Delta t}{3\tau_P}\kappa\left(P_0 - P\right). \tag{2.15}$$

The isothermal compressibility of the system, κ, was set to 4.6 x 10^{-5} bar^{-1}, the value for water at 1 atm and 300 K [90].

vibration	T [fs]
bond stretching	10 – 24
angle bending	20 – 40
hydrogen bond stretching	170 – 700

Table 2.1: Typical periods of vibrations within molecules or hydrogen bonded liquids [90].

2.3.4 Position restraints

The positions of individual atoms can be restricted to reference positions using harmonic potentials [90]. Before a production run a short MD simulation is performed at constant temperature and pressure with position restraints on all peptide atoms. This is done in order to equilibrate the solvent. In some setups restraints were also used to fix the position of individual atoms within the peptide, e.g. to prevent unfolding of the initial configuration.

2.3.5 Improving efficiency

The GROMACS MD program uses several common techniques to improve computational efficiency. For instance, neighbor lists, bond constraints, cutoff and continuum methods for treating nonbonded interactions or sphere-like box shapes (Sec. 2.3.2). In the following, the most important techniques are discussed in more detail.

Defining the time step

One major factor concerning efficiency is the size of the time step Δt. Generally, Δt should be five times smaller than the period of the fastest vibrations within a molecule in order to integrate them with reasonable accuracy [84, 90]. Considering flexible molecules as proteins in aqueous solution typical vibrations correspond to bond stretching, angle bending and hydrogen bond stretching. The periods of these vibrations are given in Tab. 2.1. In order to apply a time step of 4 fs, the fastest vibrations within the system were removed.

It was shown that bond length constraints do not significantly alter the dynamic properties of macromolecules such as proteins [102]. Correspondingly, bond stretching vibrations within the peptide were constrained using the LINCS method [103], whereas the SETTLE algorithm [104] was used for the water molecules. The LINCS algorithm resets bonds to their correct lengths after an unconstrained update using a numerical integration scheme. The SETTLE algorithm, specially implemented for rigid water molecules, is based on solving a set of Lagrange multipliers in the constrained equations of motion.

The bending of angles is essential to observe conformational changes [102] and should therefore not be constrained. The fastest angle vibrations though can be assigned to angles involving hydrogen atoms. These angle vibrations were slowed down by using heavy hydrogens. Here, the mass of a hydrogen atom is increased from 1 amu to 4 amu, while the additional mass of the hydrogens is subtracted from the connected heavy atom. Based on these modifications a time step of 4 fs was used in all simulations [105].

Treatment of nonbonded interactions

The handling of nonbonded interactions was improved in terms of efficiency in two ways. First, all noncovalent interactions were treated using a twin range cutoff. Short-range interactions were defined for interatomic distances up to 1 nm, and long-range interactions for distances between 1 and 1.4 nm. Short-range interactions were calculated every time step while long-range interactions together with the neighbor list were updated every five time steps.

Additionally, electrostatic interactions beyond the cutoff distance were modeled as a dielectric continuum. The Coulomb potential (Eq. 2.8) was modified by including the reaction field correction of the continuum [84] and is given by

$$E_{\text{coul,rf}} = \frac{1}{4\pi\epsilon_0}\frac{q_i q_j}{\epsilon_r}\left[\frac{1}{r_{ij}} + \frac{B_0 r_{ij}^2}{2r_c^3}\right], \tag{2.16}$$

where the cutoff radius r_c is set to 1.4 nm. The constant B_0 is defined as

$$B_0 = \frac{2(\epsilon_{\text{rf}} - 1)}{(2\epsilon_{\text{rf}} + 1)}, \tag{2.17}$$

with ϵ_{rf} the dielectric constant of the continuum. GROMACS uses a shifted force potential of $E_{\text{coul,rf}}$ to ensure that the potential as well as the force are zero for $r_{ij} = r_c$. In all simulations the reaction field method was applied using $\epsilon_{\text{rf}} = 54$, the self-consistent value for SPC water [106, 107].

2.4 Replica exchange method

The replica exchange method or parallel tempering was first introduced for Monte Carlo simulations. In 1999 Sugita and Okamoto developed a formulation of the replica exchange method for MD simulations [85]. In principle, multiple copies (replicas) of the system are simulated simultaneous- but independently at different temperatures. The complete state of two replicas at neighboring temperatures is exchanged at regular intervals with a metropolis-like exchange probability. The exchange probability for a canonical ensemble is given by

$$P_{ij} = \min\left(1, \exp\left[-\left(\frac{1}{k_B T_j} - \frac{1}{k_B T_i}\right)(E_i - E_j)\right]\right), \tag{2.18}$$

where E_i and T_i are the instantaneous potential energy and temperature of replica i, respectively. By this approach, fast conformational sampling due to accelerated crossing of energy barriers at high temperatures is coupled to the correct Boltzmann distribution at all other temperatures. After a successful exchange, the velocities of the particles in the system are rescaled by $(T_j/T_i)^{1/2}$ to ensure a smooth transition of the system from T_i to T_j and to avoid correlated back exchanges. To ensure a uniform exchange probability, the temperatures T_i were chosen according to the relation

$$T_i = T_{\min}(1+\epsilon)^i, \tag{2.19}$$

where $T_{\min}$ is the minimum temperature and $\epsilon = 2/\sqrt{N_{\mathrm{df}}c}$. Here, N_{df} denotes the number of degrees of freedom which in three dimensions and using bond constraints (Sec. 2.3.5) is approximately equal to $2N_{\mathrm{atom}}$, where N_{atom} indicates the number of atoms in the system. The parameter c was set to two as appropriate for protein-water systems [90]. The parameter ϵ was adjusted to achieve an exchange probability P_{ij} of about 0.3. In order to avoid correlated back exchanges, the exchange period is chosen large compared to the integrated autocorrelation time of E_i for the system at $T_{\min}$ [108, 109].

Properties of the investigated systems were studied at 280 and 293 K which approximately corresponds to the minimum temperature simulated. The maximum temperature was chosen around 400 K still close to the boiling point of water, which was used as solvent in all simulations. Ensuring an exchange probability of 0.3 over a temperature range of about 120 K required the use of 50 to 70 replicas for each system. In summary, REMD simulations are a powerful but very expensive tool to calculate the conformational distribution of large biomolecular systems. In addition, dynamic processes cannot be studied using standard REMD simulations, because the exchange in temperature space produces artificial dynamics.

2.5 Energy minimization

The initial configuration of a system as shown in Fig. 2.1 might contain residual overlaps of atoms resulting in large forces. To remove these instabilities within the system, an energy minimization of the initial configuration is performed, without and with all bonds constraint (Sec. 2.3.5), prior to the MD simulation. In this work, the steepest descent algorithm is used. It searches for the nearest local minimum in the potential energy surface of the system by systematically moving down the steepest local gradient [90]. In this procedure, the displacement of atoms, which is initially set to 0.01 nm, is iteratively decreased according to the gradient until the machine precision or a maximum number of steps is reached. The algorithm has the advantage to be numerically stable, but it is rather slow compared to other algorithms.

2.6 Analysis methods

The generated trajectories were analyzed at the temperatures of interest after allowing the system to reach an equilibrium state. Convergence of the simulations was tested according to system-specific reaction coordinates and is discussed for each system separately in Sec. 3.2, 4.2, and 5.2. In MD any equilibrium property A is determined as a time average, while averages obtained from REMD simulations rather correspond to ensemble averages. According to the ergodic hypothesis for reasonable long sampling periods both yield the same result

$$\langle A \rangle = \frac{1}{N} \sum_t A_t = \frac{1}{N} \sum_i A_i. \tag{2.20}$$

Here, A_t and A_i are equilibrium properties at time t or configuration i. N corresponds to the maximum number of time steps or configurations. The determination of frequently used equilibrium properties is explained in the following sections, while averages were obtained using Eq. 2.20.

2.6.1 Radius of gyration

The radius of gyration (R_g) is a measure for the linear extension or compactness of a peptide or protein and defined as

$$R_\mathrm{g} = \left(\frac{\sum_i ||\mathbf{r}_i||^2 \, m_i}{\sum_i m_i} \right)^{1/2}. \tag{2.21}$$

Here, m_i is the mass of atom i and $\mathbf{r}_i$ the position of atom i with respect to the center of mass of the molecule. Calculations of R_g were conducted using the GROMACS analysis tool `g_gyrate` [87].

2.6.2 Root mean square deviation

The root mean square deviation (RMSD) of certain atoms of a molecule at time t to a reference structure (time t_ref) is defined by

$$\mathrm{RMSD}(t, t_\mathrm{ref}) = \left(\frac{1}{M} \sum_{i=1}^{N} m_i ||\mathbf{r}_i(t) - \mathbf{r}_i(t_\mathrm{ref})||^2 \right)^{1/2}. \tag{2.22}$$

Here, $M = \sum_{i=1}^{N} m_i$ denotes the total mass of the molecule, while $\mathbf{r}_i(t)$ or $\mathbf{r}_i(t_\mathrm{ref})$ are the position of atom i at time t or t_ref, respectively. The RMSD was calculated using the GROMACS program `g_rms` [87]. First, the structure is fitted to the reference structure by least-square fitting, then the RMSD is calculated using Eq. 2.22.

2.6.3 Secondary structure of proteins (DSSP)

The secondary structure of peptides was determined using the program Define Secondary Structure in Proteins (DSSP) which is based on an hydrogen-bonding pattern recognition algorithm [110]. The electrostatic interaction energy E_{HB} between two possible hydrogen-bonding groups within the backbone, CO and NH, is calculated by placing charges on C,O ($+q_1$,$-q_1$) and N,H ($-q_2$,$+q_2$) atoms and using the Coulomb potential

$$E_{\mathrm{HB}} = q_1 q_2 \left(\frac{1}{r_{\mathrm{ON}}} + \frac{1}{r_{\mathrm{CH}}} - \frac{1}{r_{\mathrm{OH}}} - \frac{1}{r_{\mathrm{CN}}} \right) f. \tag{2.23}$$

Here, $q_1 = 0.42e$ and $q_2 = 0.20e$, with e the electronic unit charge, r_{AB} the interatomic distance between atoms A and B given in Å, the dimensional factor $f = 332$, and E_{HB} in kcal/mol. A good hydrogen bond has a binding energy of approximately -3 kcal/mol (≈ -12 kJ/mol). This method was developed based on peptide configurations obtained from x-ray crystallography. In order to average over coordinate errors observed in x-ray crystal structures the cutoff for a hydrogen bond between the CO group of residue i and the NH group of residue j is set to $E_{\mathrm{HB}} < -0.5$ kcal/mol (≈ -2.1 kJ/mol).

According to the presence of a hydrogen bond two structural features are defined. First, n-turns are characterized by hydrogen bonds between the CO group of residue i and the NH group of residue $i + n$, where $n = 3, 4, 5$. Then β-bridges are defined with hydrogen bonds between residues not near to each other in sequence. Based on these structural features secondary structure elements are assigned, i.e. repeating 4-turns correspond to α-helices, repeating β-bridges to β-sheets. In this work, the secondary structure content was calculated as an average over the whole peptide or for individual residues.

2.6.4 Cluster analysis

Conformations of individual peptides or oligomers were determined using a RMSD based cluster algorithm described by Daura *et al.* [111]. Here, two configurations with a RMSD below a certain cutoff are considered to be neighbors. The configuration with the largest number of neighbors with all its neighbors is defined as a cluster and removed from the pool of configurations. The procedure is repeated for the remaining configurations until the pool is empty. Each cluster corresponds to a conformation which is represented by the central configuration of the cluster. The chosen RMSD cutoff corresponds to the first minimum of the RMSD-distribution and ranged between 0.1 and 0.2 nm for the studied systems. The cluster analysis was performed using the GROMACS program `g_cluster` [87].

2.6.5 Solvent accessible surface area and solvation free energy

The molecular surface area of a solute in contact with a monomolecular layer of solvent is called the solvent accessible surface area (SASA). The SASA is the area traced by the center of mass of a spherical solvent molecule as it is rolled over the surface of the solute [112]. If its distance to the van der Waals surface of the solute is shorter than 1.4 Å it is considered to be in contact with the solute [113]. The hydrophobic and hydrophilic SASAs were calculated using the GROMACS program `g_sas` [87].

The program `g_sas` also computes the free energy of solvation (F_{solv}). Based on the SASA of individual peptide atoms, F_{solv} is determined using the atomic solvation parameters from free energies of transfer according to the model by Eisenberg and McLachlan [114].

2.6.6 Hydrogen bond and side chain contact maps

Inter- and intramolecular contact maps were calculated based on main chain hydrogen bonds and side chain contacts. Two residues i and j were considered to be in contact if at least one out of two possible main chain hydrogen bonds or one side chain contact was formed. The contacts of all pairs of residues are illustrated in a two-dimensional matrix $H(i, j)$. If a contact is formed, $H(i, j)$ equals 1, otherwise it is zero. Averaging $H(i, j)$ over an ensemble of configurations yields the contact frequency $P(i, j)$, denoted as contact map [115].

Main chain hydrogen bonds were computed using the GROMACS program `g_hbond`. According to a geometric criterion a hydrogen bond exists if the distance between donor and acceptor is ≤ 0.35 nm, and if the hydrogen-donor-acceptor angle is $\leq 30°$ [87].

A side chain contact is defined if the minimum distance between the center of mass of two side chains is smaller than 0.4 nm. The minimum distance was calculated using the GROMACS program `g_mindist` [87]. The cutoff corresponds to the first minimum of the distribution of minimum distances for all side chains of a system, and equals approximately 0.4 nm for all systems.

2.6.7 Principal component analysis

A principle component analysis (PCA), also called covariance analysis is a mathematical technique for analyzing high dimensional (possibly correlated) data sets based on their covariance matrix. By applying an orthogonal transformation a new set of uncorrelated variables, so called principle components (PCs), is produced. The PCs are ordered according to decreasing variance of the data. This allows for a reduction of the dimensionality by concentrating on the PCs with highest variance.

In this study PCA is applied to the atom coordinates of peptides in order to find correlated motions within these molecules. Since overall translational and rotational

motion is irrelevant to the internal motions, it is removed by least-square fitting to a reference structure. Here, the reference structure is always the central configuration of the most populated cluster of the system (Sec. 2.6.4). The resulting atomic positions of the peptide are described by a $3N$-dimensional trajectory $\mathbf{x}(t)$. In this study, $\mathbf{x}(t)$ contains only all non-hydrogen atoms of the peptide.

The covariance matrix C of $\mathbf{x}(t)$ is constructed. The matrix element C_{ij} corresponds to the covariance between the positions of atom i and j, and is given by

$$C_{ij} = \left\langle M_{ii}^{\frac{1}{2}} \left(x_i - \langle x_i \rangle\right) M_{jj}^{\frac{1}{2}} \left(x_j - \langle x_j \rangle\right) \right\rangle . \tag{2.24}$$

Here, x_i and x_j are the positions of atoms i and j, and $\langle . \rangle$ stands for the time average. M is a diagonal matrix containing the masses of the atoms. The symmetric $3N$x$3N$ matrix C can be diagonalized with an orthonormal transformation matrix R,

$$R^T C R = \mathrm{diag}(\lambda_1, \lambda_2, ..., \lambda_{3N}). \tag{2.25}$$

The columns in R are the eigenvectors or principle modes with eigenvalues λ. The eigenvalues are equal to the variance in the direction of the corresponding eigenvector. For PCA the eigenvectors are ordered by decreasing variance with $\lambda_1 \geq \lambda_2 \geq ... \geq \lambda_{3N}$.

The trajectory $\mathbf{x}(t)$ is then projected on the principal modes to give the principal components

$$\mathrm{PC}_i(t) = R^T M^{\frac{1}{2}} (\mathbf{x}(t) - \langle \mathbf{x} \rangle), \tag{2.26}$$

with $i = 1, ..., 3N$. The eigenvalue λ_i is the mean square fluctuation of principal component i. The first few principle modes describe collective, global motions of the system, whereas it has to be eliminated that they do not just resemble random diffusion. It has been shown that the time dependent behavior of PCs corresponding to random diffusion can be fitted to cosines with the number of periods equal to half the PC index [116, 117].

In this work, PC_1 and PC_2 were used as reaction coordinates to calculate free energy landscapes (Sec. 2.6.8). The GROMACS programs `g_covar` and `g_anaeig` were used to calculate the covariance matrix and the principal components [87]. The program `g_analyze` was used to determine the cosine content of the PCs, which is close to 1 if the largest fluctuations correspond to random diffusive behavior and smaller than 1 otherwise [87, 90].

2.6.8 Free energy landscape

From the equilibrated canonical ensemble the free energy along two order parameters x and y is determined from

$$\Delta F(x, y) = -k_B T \ln \left[\frac{P(x, y)}{P_{\min}} \right] . \tag{2.27}$$

Here, T denotes the temperature of interest, $P(x, y)$ the probability of the system to be in state (x, y), and $P_{\min}$ the minimum probability for which $\Delta F = 0$. The free energy along one order parameter x is calculated similarly to Eq. 2.27. The reaction coordinates chosen for $\Delta F(x, y)$ were the first and second principal components (Sec. 2.6.7), and for $\Delta F(x)$ the radius of gyration (Sec. 2.6.1).

2.6.9 Free energy, potential energy and entropy of transitions

Considering the equilibrium between two states

$$D_i \leftrightarrows D_j, \tag{2.28}$$

the free energy of transition, ΔF, from state D_i to D_j can be calculated using

$$\Delta F = -R\ T \ln K. \tag{2.29}$$

Here R denotes the ideal gas constant and T the temperature. The equilibrium constant K of the transition is estimated from the ratio of the number of configurations of each state observed in the trajectories, as $K = N_j/N_i$. The free energy difference can also be written as

$$\Delta F = \Delta U - T\ \Delta S, \tag{2.30}$$

where ΔU is the difference in internal energy and ΔS the difference in entropy. According to the equipartition theorem the change in internal energy equals the change in potential energy, $\Delta U = \Delta E_{\text{pot}}$. For the transition the latter can be calculated as the difference between the average potential energy of the two states

$$\Delta E_{\text{pot}} = \langle E_{\text{pot},j} \rangle - \langle E_{\text{pot},i} \rangle\,, \tag{2.31}$$

Transforming Eq. 2.30 and using ΔF and ΔU, $-T\ \Delta S$ can be obtained as well.

In order to determine major contributions to the potential energy, ΔE_{pot} is split in parts arising from covalent, Coulomb, and Lennard-Jones interactions

$$\Delta E_{\text{pot}} = \Delta E_{\text{cov}} + \Delta E_{\text{coul}} + \Delta E_{\text{LJ}}. \tag{2.32}$$

Covalent interactions are based on interactions due to angles, and dihedrals within an individual peptide. In order to use a larger time step, all bond vibrations were constrained during the simulations (Sec. 2.3.5), and therefore give no contribution to ΔE_{cov}. Coulomb and Lennard-Jones interactions can be further separated into contributions arising from peptide-peptide (PP), peptide-solvent (PS), and solvent-solvent (SS) interactions. The contributions to the potential energy of any interaction partners were calculated using the GROMACS tools `mdrun` and `g_energy` [87].

The change in entropy corresponding to the transition in Eq. 2.28 can also be divided into parts due to peptide-peptide interactions, denoted as the change in configurational

entropy, ΔS_{conf}, and contributions resulting from interactions with the solvent, $\Delta S_{\mathrm{solvent}}$, according to

$$\Delta S = \Delta S_{\mathrm{conf}} + \Delta S_{\mathrm{solvent}}. \tag{2.33}$$

The change in solvent entropy might be related to hydrophobic and electrostatic effects [118].

The configurational entropy of a state D_{i} was determined by estimating the phase space density P according to the number and population of clusters assigned to this state given by

$$S_{\mathrm{conf},i} = \langle -R \ln P \rangle = -R \sum_n P_{i,n} \ln P_{i,n}. \tag{2.34}$$

Here, $S_{\mathrm{conf},i}$ stands for the configurational entropy of the peptide in state D_i. P represents the phase space density, and the average is taken over the region in configurational space corresponding to this state. $P_{i,n}$ denotes the probability of cluster n given by $N_{i,n}/N_i$, where $N_{i,n}$ is the number of configurations in cluster n and N_i the total number of configurations in state D_i. For the transition from D_i to D_j, the change in free energy due to configurational entropy is then given by

$$-T\Delta S_{\mathrm{conf}} = -T(S_{\mathrm{conf},j} - S_{\mathrm{conf},i}). \tag{2.35}$$

The change in solvent entropy was determined indirectly as the difference between the change in total and configurational entropy by transforming Eq. 2.33.

2.6.10 Error estimation

The statistical error of an average value $\langle A \rangle$ corresponding to an equilibrated ensemble was determined using block averages. Here, the trajectory is divided into N blocks, over which the average is calculated. The block averages $\langle A_n \rangle$ are considered to be independent if the block length is long compared to the autocorrelation time of A. In that case the standard error can be estimated from

$$\mathrm{err} = \left(\frac{\sum_n (\langle A_n \rangle - \langle A \rangle)^2}{N(N-1)} \right)^{\frac{1}{2}}. \tag{2.36}$$

Chapter 3

Simulation Results for Aβ(25-35)

In this chapter simulations of Aβ(25-35) monomers, dimers, and trimers are presented. These simulations were performed in order (i) to determine the conformation of the preaggregated state, and (ii) to study the conformational diversity and thermodynamics of early aggregation intermediates as dimers and trimers in aqueous environment.

The following section will point out relevant conclusions from previous studies on Aβ(25-35) which form the basis of this work. Sec. 3.2 explains the setups for all simulations performed on the Aβ(25-35) system and gives details on the equilibration periods necessary. Simulation results for monomers, dimers and trimers at 293 K will be discussed in Sec. 3.3 – 3.5. Sec. 3.6 focuses on structural and thermodynamic characteristics depending on the oligomer size to obtain insides on the aggregation process.

3.1 Previous experimental and theoretical observations

Aβ(25-35) is the shortest fragment of Aβ which forms β-sheet rich fibrils and exhibits the toxicity of the full length peptide [4, 61, 62]. The amino acid sequence of this fragment can be extracted from the sequence of the full length peptide shown in Fig. 1.6 in Sec. 1.2.1. Similar to the full length peptide Aβ(25-35) is of amphiphilic nature but with only three polar residues near the N-terminus. At neutral pH residue K28 and both termini are charged, resulting in a net charge of plus one.

Observing the pre-aggregated state of Aβ(25-35) in water is unfeasible experimentally as at concentrations necessary for analysis Aβ(25-35) aggregates strongly. However, three dimensional structures of Aβ(25-35) in mixtures of water with HFIP as a membrane mimicking environment have been solved by NMR [63]. In a 80:20 (vol/vol) HFIP/water mixture, Aβ(25-35) adopts an α-helical conformation, while in 20:80 HFIP/water a type I β-turn centered on residues S26 and N27 is formed. Likewise, Wei and Shea performed all-atom REMD simulations in a 80:20 HFIP/water mixture yielding an α-helical conformation similar to experiments [62]. Their REMD simulations of Aβ(25-35)

in pure water showed the formation of collapsed coil structures coexisting with two types of β-hairpin conformations, which were characterized as type II' β-turn structures differing in the twist of the strands to one another. Simulations in both environments were started from the solved α-helical NMR structure. Sec. 3.3 of this work focuses on the monomeric state of Aβ(25-35) in water starting from a fully extended conformation in order to test if the previously obtained equilibrium between unstructured and β-hairpin conformations can be reproduced under different initial conditions.

Several experimental groups studied the nature of Aβ(25-35) aggregates in solution. For example, CD and FTIR spectra of Aβ(25-35) solutions at pH 7 and temperatures ranging from 281 to 310 K were measured immediately after mixing. The spectra showed the occurrence of β-turn as well as, presumably antiparallel, β-sheet conformations. Further incubation of the solutions for several hours yielded a decreased β-turn but increased β-sheet content [61, 119, 120, 121]. Therefore, the smallest detectable aggregates can be assumed to contain a significant β-sheet structure in combination with β-turns. H/D exchange NMR measurements revealed insights on the peptide arrangement within Aβ(25-35) fibrils [64]. The determined protected core region (K28 – M35) suggests either an out-of-register antiparallel or in-register parallel alignment of the peptides [64]. Furthermore, AFM images of Aβ(25-35) fibrils showed two distinct protofilament morphologies with diameters of 3.58 ± 1.53 nm and 1.41 ± 0.48 nm, respectively [65].

A number of theoretical studies tested the stability of pregenerated Aβ(25-35) oligmers. Starting from extended parallel or antiparallel β-sheet conformations the stability of dimers and small oligomers was studied using impulse-docking and short MD simulations [122]. Here, the most stable dimer contained extended peptides forming an anti-parallel β-sheet and salt bridges between the termini. Short MD simulations by Ma and Nussinov showed that protofibrils containing extended peptides in parallel in-register or antiparallel out-of-register alignments are stable over several nanoseconds [123].

In contrast to previous theoretical studies, the present work studied the spontaneous aggregation of Aβ(25-35) to dimers and trimers, respectively. Prestructured monomers are the most likely candidates for aggregation. In this spirit, the most typical conformation of the monomers obtained in Sec. 3.3 served as initial configurations for the individual peptides. Very recent Wei *et al.* published a study on Aβ(25-35) dimers at 300 K using a similar approach [124]. Their results will be discussed in context to the present work.

3.2 System setup and equilibration

Aβ(25-35) monomer and oligomers were studied in aqueous solution. In each system the protonation of the individual peptides was chosen to mimic neutral pH. Important setup parameters are listed in Tab. 3.1.

Simulation system	$N_{\mathrm{Cl}-}$	N_{w}	T/K	N_{r}	run time/ns
monomer	1	6846	290-403	64	100
dimer	2	4003	290-374	50	200
trimer	3	5939	290-394	60	400

Table 3.1: Simulation setups for production runs. $N_{\mathrm{Cl}-}$ and N_{w} give the number of chloride ions and water molecules, respectively. N_{r} stands for the number of replicas simulated over the corresponding temperature range. Run time gives the reached simulation time.

The simulation of the monomeric state was started from an extended configuration randomly placed in an octahedral box. The dimensions of the box were chosen such that the minimum distance between the solute and the boundaries of the box was 1.2 nm for the initial configuration. To counterbalance the positive charge of the peptide one chloride ion was added. The remaining space was filled by 6846 water molecules. The system was energy minimized and simulated for 1 ns at 293 K and 1 bar using position restraints on the peptide as described in Sec. 2.5 and 2.3.4, respectively. In addition, the system was simulated for 1 ns without restraints at the same temperature and pressure providing the initial configuration of the monomer REMD simulation.

The oligomeric systems were generated using the same procedure but with different initial configurations. As mentioned previously, the monomeric state adopts two types of β-hairpin conformations differing in the twist of the strands to one another, which are termed in the following as β-hairpin A and B [62]. Two peptides in either of both conformations served as initial configurations for the dimeric state while a third peptide in β-hairpin A conformation was used for the trimer simulation. For each oligomer system, two or three peptides in random mutual orientation separated by approximately 1 nm were placed in an octahedral box with dimensions chosen similar as for the monomer system. The number of used chloride ions and water molecules are given in Tab. 3.1.

For each Aβ(25-35) system a REMD simulation was performed. The used number of replicas, the corresponding temperature range and the simulation time of individual replicas are also listed in Tab. 3.1. Exchange of replicas between neighboring temperatures was attempted only every 5 ps for each system.

Convergence was tested according to several reaction coordinates as the radius of gyration (R_{g}), the number of hydrogen bonds (N_{HB}), and the secondary structure content. Fig. 3.1 shows running averages for the number of residues per peptide adopting a turn or β-sheet conformation in (a) monomers, (b) dimers, and (c) trimers at 293 K. Values were averaged over (a,b) 2000 ps and (c) 5000 ps windows. The data indicate that the simulations converged within 25 ns, 100 ns, and 200 ns, respectively.

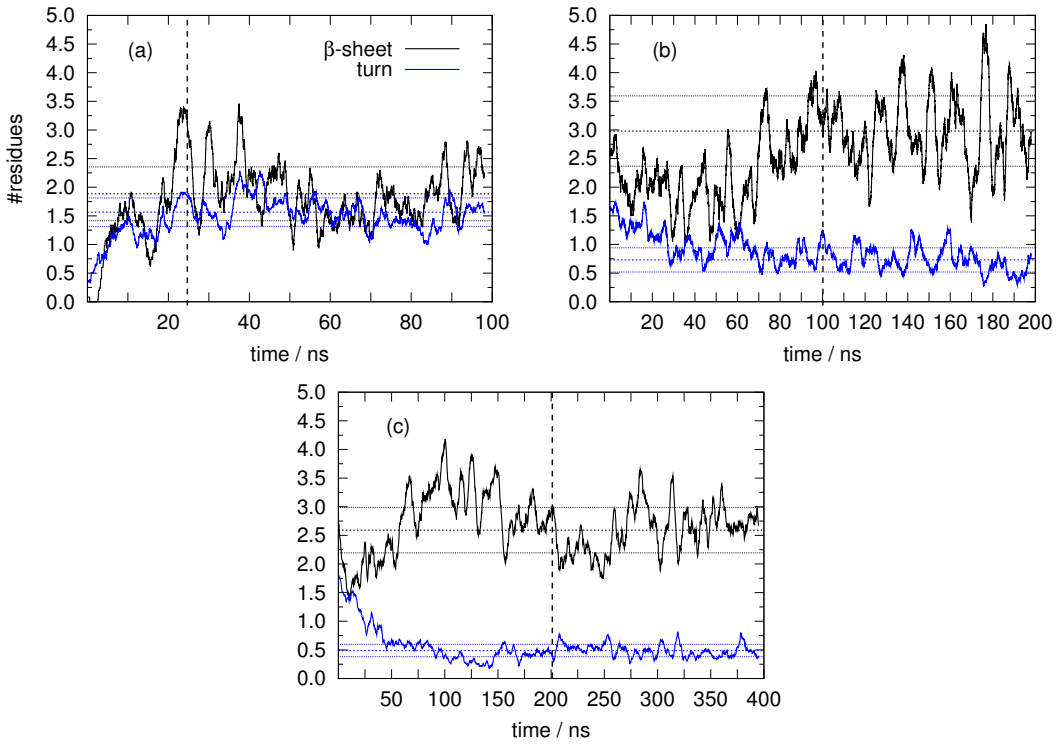

Figure 3.1: Convergence of (a) monomer, (b) dimer, and (c) trimer simulations at 293 K. Shown are running averages over (a,b) 2000 ps and (c) 5000 ps windows for the number of residues per peptide adopting turn and β-sheet conformation. The vertical dashed lines mark the beginning of the sampling period. A horizontal dashed line indicates the average over the sampling period, and the dotted lines give the corresponding standard deviation.

3.3 Conformation of monomers

Simulations of Aβ(25-35) monomers in aqueous environment were performed starting from a fully extended configuration. The ensemble sampled during the final 75 ns of the simulation was analyzed using the RMSD based cluster algorithm explained in Sec. 2.6.4. Here, two configurations belonged to one cluster if the RMSD of the backbone atoms of residues N27 – G33 was smaller than 0.1 nm. This method yielded 93 clusters. Central configurations of three predominant clusters are shown in Fig. 3.2. Conformations *A* and *B*, populated by 37 ± 5 % and 23 ± 4 % of all configurations, are two different β-hairpin structures. Conformation *C*, populated by 8 ± 2 % of all configurations, is unstructured but of similar topology as the β-hairpins. Both β-hairpin structures, *A* and *B*, are characterized by a β-turn involving residues G29 and A30, and two short antiparallel β-strands consisting of residues N27 – K28 and I31 – I32. The β-strands are stabilized by three interstrand main chain hydrogen bonds: I31:HN-K28:O, K28:HN-I31:O and G33:HN-S26:O, as shown for the main conformation (*A1*) in Fig. 3.2. Additionally, the two β-hairpin conformations, *A* and *B*, differ in the twist of the strands to one another.

The β-hairpin motif is also illustrated by the secondary structure content of individual residues shown in Fig. 3.3. According to the β-sheet content of residues N27, K28, I31, and I32, the β-hairpin structures are populated approximately 40 % of the time while at other times the peptide is rather unstructured but bent. The turn involving the central residues G29 and A30 is more stable, and appears approximately 70 % of the time. Similarly, in previous MD simulations of another amyloid peptide the turn was found to be the most stable structural element of a β-hairpin conformation [125].

All these findings agree with the previous study on Aβ(25-35) monomers in aqueous environment by Wei and Shea [62]. They started their REMD simulations from a different initial configuration, the α-helical NMR-derived conformation observed in 80:20 (vol/vol) HFIP/water mixture.

Prestructured conformers are most likely to induce aggregation due to entropic reasons. In order to use the most dominant conformations as starting point for the aggregation, the β-hairpin conformations *A* and *B* shown in Fig. 3.2 served as initial configurations of the peptides in simulations of dimers and trimers discussed in the following sections.

3.4 Conformational diversity of dimers

The following sections discuss the results of the simulations of Aβ(25-35) dimers. The last 100 ns of the trajectory at 293 K were used for the analysis.

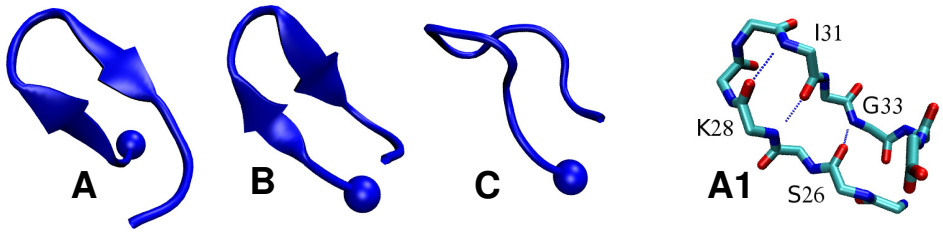

Figure 3.2: Central configurations of predominant clusters together comprising 68 % of all configurations of the ensemble of Aβ(25-35) monomers at 293 K. For conformations $A-C$, the peptide backbone is shown in ribbon representation; the C_α atom of G25 is shown as a sphere. Population of individual clusters: A 37 ± 5 %, B 23 ± 4 %, and C 8 ± 2 %. Conformation $A1$ corresponds to conformation A with the peptide main chain shown in stick representation; O atoms are colored red, N atoms are blue, and C atoms are turquoise. The dashed blue lines indicate intramolecular main chain hydrogen bonds.

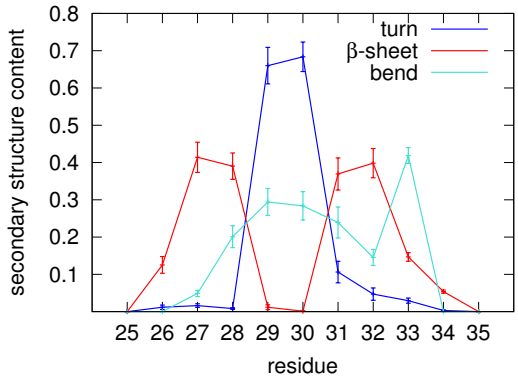

Figure 3.3: Secondary structure content of individual residues for the ensemble of Aβ(25-35) monomers at 293 K. Given are turn, bend, and intramolecular β-sheet content. There was no significant α-helix content observed.

3.4.1 Analysis of conformational clusters

In order to determine main conformations of Aβ(25-35) dimers a cluster analysis was performed as explained in Sec. 2.6.4. The analysis was based on the backbone atoms of residues N27 – G33 and a RMSD cutoff of 0.15 nm. The temperature of 293 K was chosen in correspondence to previous *in vitro* experiments on this peptide. The clustering resulted in 442 poorly populated clusters. The central structures of the nine most populated clusters ($A-I$) together with their populations are shown in Fig. 3.4. The conformations of all clusters, except C, form intra- or intermolecular β-sheets. In four of these conformations, corresponding to 13 % of all configurations, the individual peptides are partly or fully extended forming antiparallel intermolecular β-sheets. Such extended dimer conformations are one of the possible alignments that are believed to exist in Aβ(25-35) fibrils [120, 121, 126]. In three clusters, corresponding to 7 % of all configurations, one or both of the peptides adopt a compact, β-hairpin-like conformation similar to Aβ(25-35) monomers, compare with Fig. 3.2. In conformation F the dimer contains a parallel intermolecular β-sheet. Recently, Wei *et al.* observed similar results for Aβ(25-35) dimers at 310 K [124]. In contrast to the present work, they found a lower population of ordered, extended states and within these states parallel and antiparallel β-strand conformations. Differences in the results between this study and that by Wei *et al.* likely arise from differences in the simulation setups, the higher temperature and shorter equilibration period they used. For the present simulations the population of compact and extended dimers is not equilibrated before 50 ns which is twice as long as considered by Wei *et al.*.

Free energy profile along R_g

Based on the observation of compact and extended conformations the radius of gyration as a measure for the linear extension of the peptides was chosen as an order parameter to visualize the free energy landscape. In Fig. 3.5 the free energy along R_g is plotted showing two local free energy minima located at $R_g \approx 0.6$ nm and $R_g \approx 0.9$ nm. The minimum for the smaller radius of gyration is roughly 3 kJ/mol below that for the larger radius. Both minima are separated by a free energy barrier of 6 kJ/mol at $R_g \approx 0.75$ nm. Additionally, the minimum for the smaller radius of gyration is separated in two parts by an energy barrier of roughly 1 kJ/mol.

According to the free energy five R_g regions can be distinguished. Fig. 3.5 also shows the appearance of the nine main conformations $A-I$ within these R_g regions. Dimers in the free energy minimum at $R_g \approx 0.6$ nm adopt rather compact conformations. The minimum in R_g region I contains the β-hairpin-like conformations D, G, and H whereas dimer conformations within R_g region III are unstructured (C) or contain a short parallel intermolecular β-sheet (F). The local free energy minimum corresponding to R_g region

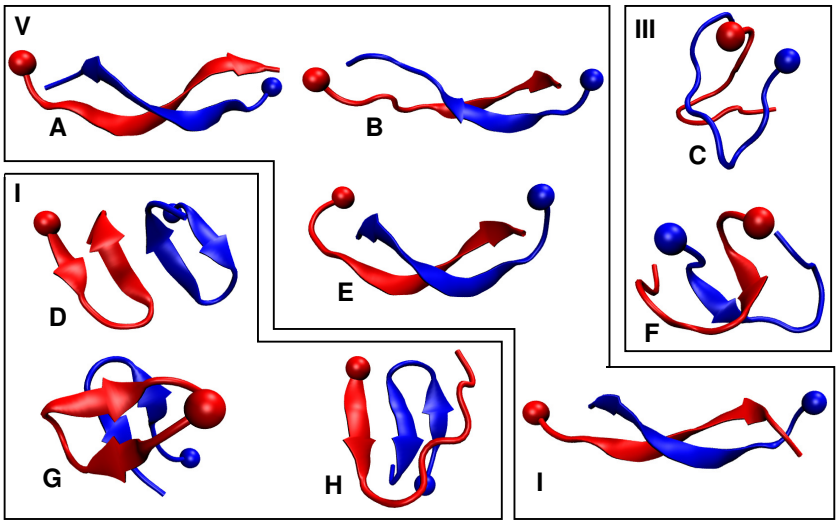

Figure 3.4: Central configurations of the nine largest out of 442 clusters together containing 25 % of all configurations of the ensemble of Aβ(25-35) dimers at 293 K. Clusters are denoted by A to I with populations A 6 ± 2 %, B 3 ± 2 %, $C-D$ 3 ± 1 %, $E-I$ 2 ± 1 %. The peptide backbone is shown in ribbon representation; the C_α atom of G25 of each peptide is depicted as a sphere. The number in the upper left of each box refers to the R_g region in which the conformations were found. Here, I corresponds to compact, β-hairpin-like conformations, III contains rather unstructured conformations, and in V peptides are partly or fully extended forming antiparallel β-sheets.

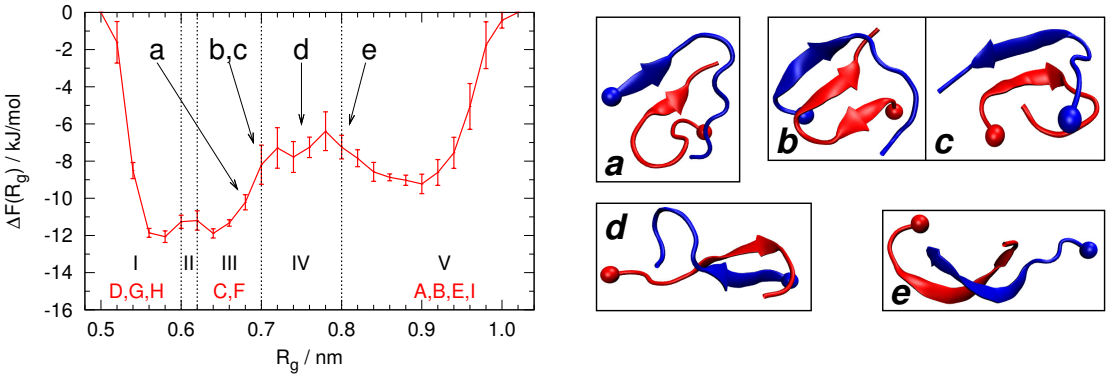

Figure 3.5: Free energy profile along the radius of gyration, R_g, and the definition of five R_g regions which are populated by (I)25 %, (II)8 %, (III)33 %, (IV)10 %, and (V)24 % of all configurations. The capital letters $A-I$ refer to the main conformations given in Fig. 3.4 and show their position along the R_g axis. Also shown are representative conformations $(a-e)$ illustrating the transition between compact and extended dimer conformations and their position along the R_g axis.

V is populated by the extended dimer conformations *A*, *B*, *E*, *I*. The individual extended conformations differ in the length of the formed β-sheet and the bending of the peptides. Interestingly, the dominant conformations *A* and *B* are found to be extended, 'fibril-like' dimers although compact conformations are more populated in total, see Fig. 3.5.

Secondary structure and intermolecular hydrogen bonds

Of course, the free energy profile along R_g is a projection of the multi-dimensional conformational space of the dimer system along one reaction coordinate. In order to determine if R_g is in fact an appropriate order parameter of th system, the defined sub-ensembles of dimers were investigated in more detail. Secondary structure motifs and intermolecular main chain hydrogen bonds were analyzed for the individual R_g regions by averaging over all configurations within a certain R_g region. Fig. 3.6 shows the secondary structure content of the individual residues for each R_g region. Plotted are (a) the turn, (b) the intra- and (c) the intermolecular β-sheet content. Fig. 3.7 shows the corresponding hydrogen bond maps. Plotted is the probability of finding at least one main chain hydrogen bond between residues of peptide A and peptide B. A high probability stands for a particularly stable hydrogen bond.

The plots of the secondary structure content verify what is suggested already from the free energy profile along R_g and the related main conformations shown in Fig. 3.5. Based on the turn and the intramolecular β-sheet content, the compact dimers especially

in R_g regions I and II are populated by β-hairpin-like conformations similar to Aβ(25-35) monomers, compare Fig. 3.3 and Fig. 3.6(a,b). With increasing R_g the turn and intramolecular β-sheet content decrease indicating a gradual dissolution of the β-hairpin motif. This is illustrated by the conformations C and F shown in Fig. 3.4. None of the extended configurations in region V forms intramolecular β-sheets and only an insignificant amount of turn content is observed, though turn conformations are more abundant than the specific intramolecular β-sheets.

As plotted in Fig. 3.6(c), with the loss of the β-hairpin motif the intermolecular β-sheet content for the inner residues increases. In general, compact dimers (R_g region I-III) form only few intermolecular hydrogen bonds as shown by the low intermolecular β-sheet content of < 25 %. Compact dimers in R_g region I form few intermolecular β-sheets preferentially involving the hydrophobic residues I32 and G33. The hydrogen bond map in Fig. 3.7(a), shows that 20-30 % of these dimers form a main chain hydrogen bond between residues I32 of both peptides. In contrast, the compact dimers in R_g region II and III form few intermolecular β-sheets between hydrophilic N-terminal and hydrophobic C-terminal residues, see Fig. 3.6(c). The hydrogen bond map in Fig. 3.7(b), shows that dimers in R_g region III form main chain hydrogen bonds rather between N- and C-terminal residues like S26 – M35 and N27 – M35, while R_g region II shows no significant hydrogen bonding pattern.

At the transition region IV where the β-hairpin motif is almost lost, the intermolecular β-sheet content increases to 30-50 % for the inner residues N27 – G33, see Fig. 3.6(c). In approximately 20 % of the configurations peptides are already aligned in an antiparallel manner as indicated by the diagonal contact pattern spanning from the top left to the bottom right of the hydrogen bond map in Fig. 3.7(c). The importance of the turn residues G29 and A30 in the course of the transition to extended conformations will be discussed in Sec. 3.4.2.

In extended dimers in R_g region V, intermolecular β-sheets between the inner residues are formed in 60-90% of the configurations as shown by Fig. 3.6(c). The hydrogen bond map of extended dimers in Fig. 3.7(d), indicates the main chain hydrogen bonds stabilizing the antiparallel β-sheet which involves the inner residues K28 – G33. This corresponds well to the protected core region within Aβ(25-35) fibrils discovered by H/D exchange NMR measurements [64]. The formation of in- and out-of-register antiparallel β-sheets is possible, the former being marked in red in the diagram. Most of the revealed hydrogen bonds appear in 40-60 % of the extended dimer configurations. Comparing the probability of main chain hydrogen bonds for the different types of dimers, the ensemble of extended dimers seems to be more ordered than the ensembles of compact configurations.

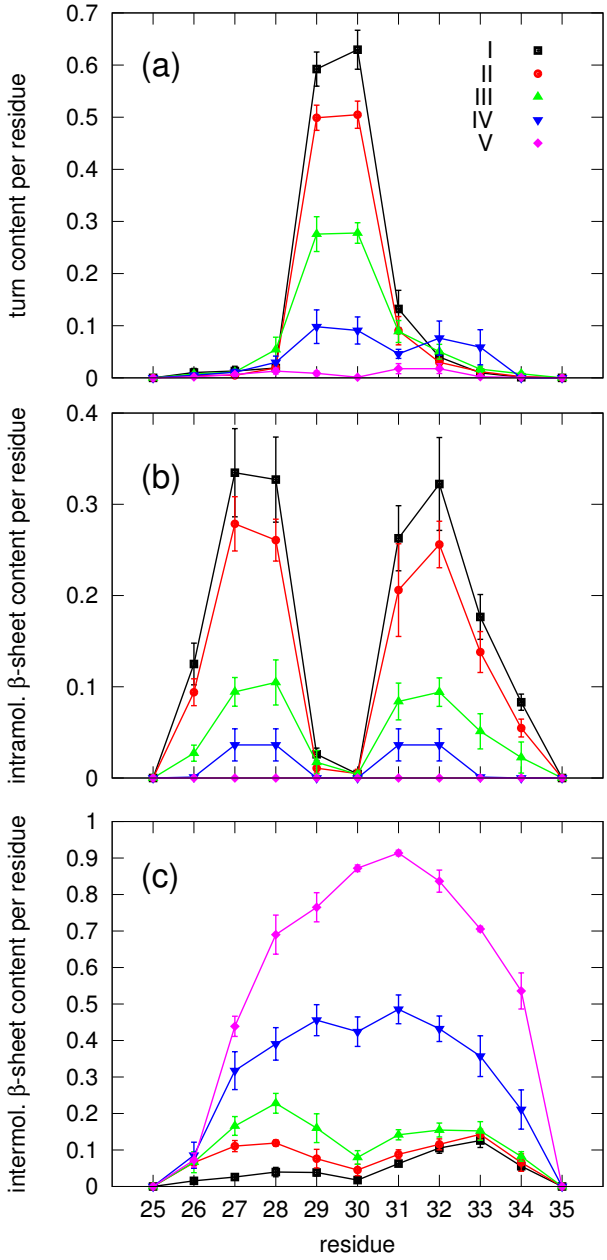

Figure 3.6: Secondary structure content of individual residues averaged over both peptides within a dimer for R_g regions I-V defined in Fig. 3.5 and the monomeric state distinguishing between (a) turn, (b) intramolecular β-sheet, and (c) intermolecular β-sheet content.

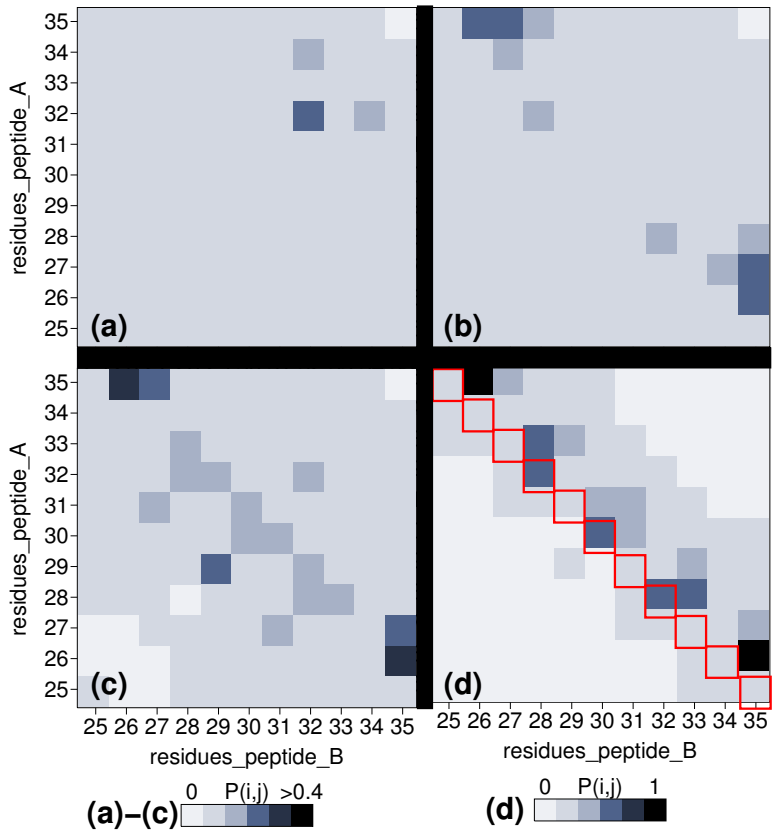

Figure 3.7: Intermolecular main chain hydrogen bond maps of R_g-regions (a) I, (b) III, (c) IV and (d) V, respectively, defined in Fig. 3.5. Hydrogen bonds characterizing antiparallel in-register alignment of peptides within extended dimers (d) are marked in red.

3.4.2 Transition from disordered to fibril-like dimers

According to the analysis in the previous section, for simplicity the ensemble of Aβ(25-35) dimers at 293 K is divided in two main sub-ensembles containing either compact (R_g region I-III) or extended conformations (R_g region V). The extended conformations show the highest intermolecular β-sheet content and might serve as precursors for protofibril formation. Hence, the transition from disordered, compact conformations to extended, fibril-like conformations is of particular interest. This section focuses on the determination of intermolecular interactions promoting this transition, while the next section discusses the thermodynamics.

In order to find dominant inter peptide interactions during the transition, configurations within R_g region IV, the transition region, were analyzed in more detail. First, configurations corresponding to a certain R_g-interval of 0.02 nm within R_g region IV were clustered as described in section Fig. 3.4.1. Representative conformations and their position along the R_g axis are plotted in Fig. 3.5. Starting at the small R_g end of the transition region, dimers form parallel or anti-parallel β-sheets between N-and C-terminal residues as illustrated by conformations *a*, *b*, and *c* shown in Fig. 3.5. With increasing R_g the anti-parallel alignment of the peptides is preferred while the residues involved in the β-sheets slightly change between conformations *c*, *d*, and *e*.

The most significant intermolecular main chain hydrogen bonds and side chain contacts were calculated along the radius of gyration, $N_X(R_g)$. Here, data were obtained in 0.02 nm intervals of R_g and averaged over the configurations within such an interval. Hydrogen bonds and side chain contacts were calculated as explained in Sec. 2.6.6. Fig. 3.8 shows the probability of such an intermolecular contact along R_g. According to Fig. 3.8 (a), intermolecular main chain hydrogen bonds between residues K28 – I32 and A30 – A30 are present in 10-30 % of the configurations at $R_g \approx 0.7$ nm. About 30 % of the dimers in this R_g region are also stabilized by a hydrophobic side chain contact between residues I31 – I31. The importance of I31 for the stability and toxicity of Aβ(25-35) fibrils is also indicated from experimental results [61]. For radii of gyration between 0.7 and 0.8 nm, intermolecular main chain hydrogen bonds between residues N27 – I31 and both turn residues G29 – G29 are the most prominent interactions as shown in Fig. 3.8 (b). With further increasing R_g the most stable main chain hydrogen bonds are formed between residues G29 – G33, I31 – I31, K28 – I32, and A30 – A30.

The observed intermolecular contacts are present in the prominent conformations shown in Fig. 3.5. In this transition region, the formation of intermolecular main chain hydrogen bonds between the turn residues A30 – A30 and G29 – G29 seems to support the antiparallel alignment of the peptides as found in extended conformations. Additionally, a shift of the intermolecular hydrogen bond network is observed, which is drawn in a simple sequence pattern shown in Fig. 3.9. Starting with conformation *c*, where both peptides are in an in-register antiparallel alignment, the prominent main chain hydrogen

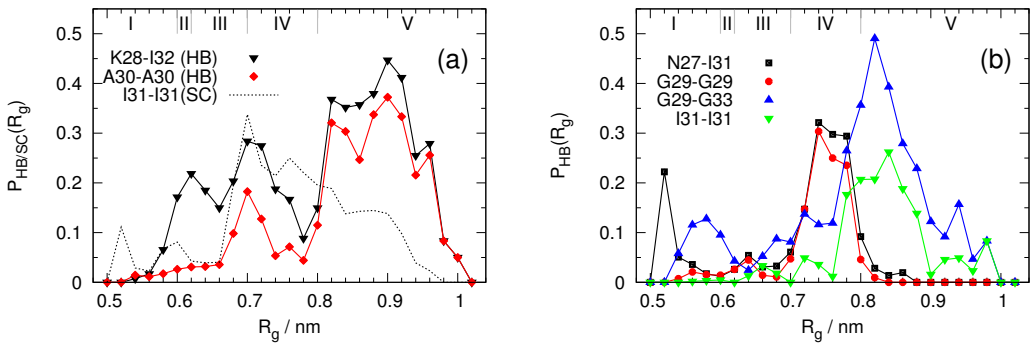

Figure 3.8: Probability of selected intermolecular main chain hydrogen bonds (HB) or side chain contacts (SC) as a function of the radius of gyration. Plotted are contacts significant at (a) $R_{\mathrm{g}} \approx 0.7$ nm, and (b) $R_{\mathrm{g}} > 0.7$ nm.

bonds are present as expected from the probability distribution given in Fig. 3.8 (a). Conformation *d*, shows a slight out-of-register shift stabilized by main chain hydrogen bonds between residues G29 – G29 and N27 – I31. With increasing R_{g} as in conformation *e* the β-sheet shifts again but in the opposite direction now forming three hydrogen bonds between the hydrophobic residues G29 – G33 and I31 – I31 as illustrated in Fig. 3.8 and Fig. 3.9.

Note that R_{g} stands for the average over the radii of gyration of the individual peptides. The change in register is observed for transitions of R_{g} from 0.7 to 0.8 nm. Dissociated states also present in the simulations correspond to significantly smaller values of R_{g} (< 0.6 nm). This suggests that no dissociation takes place for R_{g} between 0.7 and 0.8 nm. The change in register observed here hence proceeds without dissociation of the peptides; this process is denoted as reptation. Reorganization of aggregated peptide structures by reptation as well as dissolution has been observed previously [127, 128, 129]. For the prion peptide H1 both mechanisms were found while the peptide concentration determined which form of reorganization was predominant [130].

3.4.3 Interactions stabilizing compact and extended dimer conformations

In the following the compact or extended state is defined based on the free energy profile along R_{g} shown in Fig. 3.5. Compact dimers ($\mathrm{D_{com}}$) shall correspond to 0.54 nm $< R_{\mathrm{g}} <$ 0.7 nm and extended dimers ($\mathrm{D_{ext}}$) to 0.8 nm $< R_{\mathrm{g}} <$ 0.94 nm, and the equilibrium

$$\mathrm{D_{com}} \rightleftarrows \mathrm{D_{ext}} \tag{3.1}$$

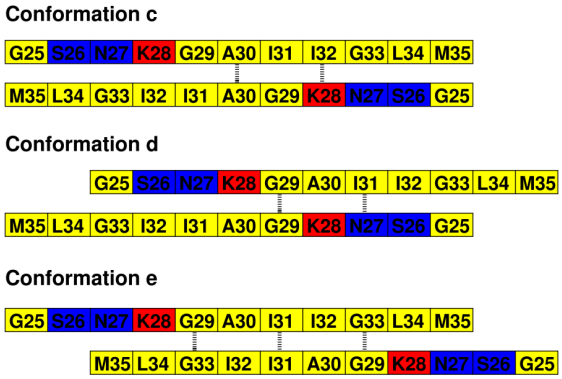

Figure 3.9: Inter main chain hydrogen bond patterns of dimer conformations *c*, *d*, and *e* in the transition region shown in Fig. 3.5. Dominant hydrogen bonds are drawn by dotted lines. Color coding of the amino acids as explained in Fig. 1.6.

is studied. The free energy of the transition from compact to extended dimers was calculated using Eq. 2.29, yielding $\Delta F = 2.9 \pm 0.5$ kJ/mol. This indicates that compact conformations are marginally favored over the extended state. The energetic and entropic contributions were determined using Eq. 2.30 and 2.31, yielding $\Delta E_{\mathrm{pot}} = -25 \pm 14$ kJ/mol and $-T\ \Delta S = 28 \pm 14$ kJ/mol, respectively. In other words, compact dimer conformations exhibit higher entropy while extended conformations are lower in energy. The equilibrium between the two is governed by a large energy-entropy compensation.

Analysis of energetic contributions

In order to determine the major contributions to the potential energy, ΔE_{pot} is split in parts arising from peptide-peptide (PP), peptide-solvent (PS), and solvent-solvent (SS) interactions. Additionally, for each interaction pair contributions due to covalent, Coulomb, and van der Waals interactions were determined, and are listed in Tab. 3.2. A few contributions for which no significant change was detected are marked with stars.

The main part to the potential energy is provided by peptide-peptide interactions (ΔE_{PP}). Interactions corresponding to angles and dihedrals are slightly more favorable in extended conformations. Most interesting is the competition between van der Waals and Coulomb interactions. Van der Waals interactions stabilize compact dimers due to closer packing of the molecules. Coulomb interactions, on the other hand, favor extended dimers as a result of stronger interactions between the charged residues and better backbone hydrogen bonding. The latter is addressed by $\Delta E_{\mathrm{bb-ter,coul}}$ based on the backbone atoms except for the terminal residues G25 and M35, and adds up to approximately -20 kJ/mol. The electrostatic stabilization arising from interactions between the charged terminal residues G25 and M35 ($\Delta E_{\mathrm{G25-M35,coul}}$) and the charged

	ΔE_{cov}	ΔE_{coul}	ΔE_{LJ}
PP	−8.8(1.2)	−37(24)	25.7(2.8)
PS	–	21(46)*	−22.4(2.2)
SS	–	4(42)*	−8(17)*
bb – ter	–	−20.2(3.1)	−4.2(3.2)
G25 – M35	–	−30(20)	0.23(0.61)*
K28 – M35	–	−43(11)	−0.1(1.7)*

Table 3.2: Covalent, electrostatic and Lennard-Jones contributions to the potential energy of the transition for certain interaction partners: peptide-peptide (PP), peptide-solvent (PS), solvent-solvent (SS), backbone atoms without terminal residues (bb – ter), the charged termini (G25 – M35), and the charged residues K28 and M35 (K28 – M35). Energies are given in kJ/mol with standard errors in parentheses. Values marked with stars are zero within error.

residues K28 and M35 ($\Delta E_{\mathrm{K28-M35,coul}}$) together yield approximately -40 to -100 kJ/mol.

Contacts between the charged groups appear if the distance between them is shorter than 0.6 nm. This criterion is based on the minimum distance distribution of these groups. Contacts between G25 and M35 were found in 79% of the extended dimers while the K28 – M35 contact appears in 56 % of the extended configurations. Fig. 3.10 shows snapshots for both types of interaction pairs. The K28 – M35 contact appears often in addition to the interaction between the termini. Here, the negatively charged M35 terminus is shielded by the positive charges of the G25 terminus and the K28 side chain. Terzi *et al.* studied the aggregation of Aβ(25-35) at different pH. For neutral pH they suggested that peptides within fibrils align in an antiparallel out-of-register β-sheet stabilized by ion pairs between K28 and M35 [119]. Their molecular dimer model looks similar to the antiparallel extended dimer conformations presented here but lacking the additional stabilization due to interactions between the charged termini G25 and M35. The present simulations show that the interaction between the charged termini are one of the major stabilizing forces in extended dimer conformations.

Analysis of entropic contributions

The total entropic contribution determined above results in $-T\Delta S = 28 \pm 14$ kJ/mol. The contribution due to the change in configurational entropy was calculated using Eq. 2.34 and 2.35. For each state, compact or extended, a cluster analysis was performed based on the criterion used in Sec. 3.4.1 for the whole ensemble. The resulting configurational entropy of the compact dimer state (317 clusters) is larger than for the ensemble of extended conformations (54 clusters). The change in configurational entropy of the transition yields $-T\ \Delta S_{\mathrm{conf}} = 6.5 \pm 2.4$ kJ/mol which corresponds to approxi-

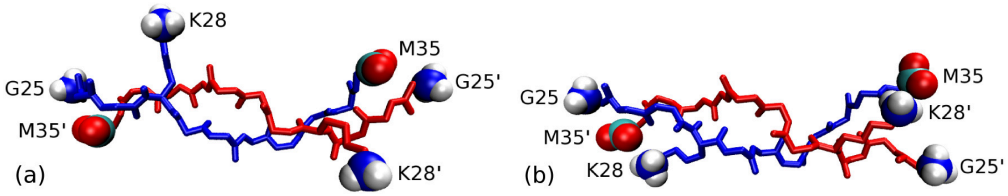

Figure 3.10: Snapshots of extended dimers with strong intermolecular interactions between the charged groups of (a) the terminal residues G25 and M35 and (b) the residues K28 and M35. The peptide backbone is shown in stick representation; atoms of amine and carboxyl groups are shown as colored spheres: C atoms in turquoise, O atoms in red, N atoms in blue, and H atoms in white.

mately 25% of the total entropic stabilization of compact dimer conformations. It could be argued that ΔS_{conf} is based only on a subunit of the full dimer, the backbone atoms of residues N27 to G33, and might represent not the total ΔS_{conf}. Taking all atoms into account for the cluster analysis changes the RMSD distribution and suggests 0.4 nm as a reasonable RMSD cutoff. The resulting $-T\ \Delta S_{\text{conf}}$ of 6.0 ± 1.1 kJ/mol is similar to the first value, confirming consistency of the applied method.

The remaining entropic contribution to the free energy of transition can be related to the solvent by

$$-T\Delta S_{\text{solvent}} = -T\Delta S - (-T\Delta S_{\text{conf}}), \tag{3.2}$$

which yields approximately 22 ± 14 kJ/mol. It is presumably due to hydrophobic effects caused by an increase in hydrophobic surface area of 0.53 ± 0.07 nm^2. A significant contribution to the solvent entropy due to electrostatic effects is also possible [118].

3.4.4 Critical dimer concentration

The protein concentration at which significant aggregation sets in is denoted as the critical concentration (CC). Below the CC only very few aggregates are present, while above the CC the concentration of monomers remains constant with increasing peptide concentration. Similar to micelle formation, for large aggregates this process can be treated as a true phase separation [131]. For Aβ(25-35), CC $\approx$ 0.02 mM, as determined from sedimentation assays [61, 132]. REMD simulations of Aβ(25-35 dimers) were conducted at a concentration $c_{\text{sim}} = 20.3$ mM. The concentration of free monomers appearing in the course of the simulation should equal CC.

At 293 K the monomeric state is only rarely found with a probability, P_{mono}, of 0.003 ± 0.002. P_{mono} corresponds to the ratio N_{mono}/N, where N_{mono} stands for the number of configurations in the monomeric state and N denotes the total number of configurations. The critical concentration of monomers in the solution can then be

estimated by

$$\mathrm{CC_{sim}} = c_{\mathrm{sim}}\ P_{\mathrm{mono}}, \tag{3.3}$$

resulting in 0.06 ± 0.04 mM, in good agreement with the experimental value. It should be noted that the calculated $\mathrm{CC_{sim}}$ may serve as a benchmark. First of all, taking into account that the formed dimers slightly reduce the box volume accessible for free monomers, the $\mathrm{CC_{sim}}$ is presumably larger than 0.06 mM. On the other hand, higher order aggregates are expected to be more stable than dimers. Hence, the former would be more stable at lower concentrations than dimeric states. Thus, the CC of dimers estimated here corresponds to an upper bound for the actual CC of this peptide corresponding to the true phase separation between peptide and water. It can be also concluded that at peptide concentrations of $\mathrm{CC_{sim}}$ the dimer corresponds to the critical nucleus for fibril formation.

3.5 Conformational ensemble of trimers

The following sections present the results of the simulations of Aβ(25-35) trimers at 293 K. As described in Sec. 3.2, the final 200 ns of the trajectory were used for analysis.

3.5.1 Analysis of conformational clusters

Similar to the other Aβ(25-35) systems, a cluster analysis (Sec. 2.6.4) based on the backbone atoms of residues N27 – G33 was performed. Here, a RMSD cutoff of 0.2 nm was used, according to the RMSD distribution of this system. The analysis yielded 469 poorly populated clusters. The central configurations of the twenty predominant clusters are shown in Fig. 3.11. Together these twenty clusters correspond to 42 % of all configurations, while none of the clusters is populated by more than 5 %. Eight conformations, illustrated by the gray box in Fig. 3.11, show none or rather little intermolecular β-sheet formation. Among these are the three most populated conformations. Only conformations #2 and #3 show β-hairpin-like or U-shaped peptide structures similar to the initial monomer conformation. In the other twelve conformations peptides are rather extended forming small or large intermolecular β-sheets which are predominantly antiparallel.

Ordered, β-sheet rich conformations can serve as building blocks for protofibrils. The most ordered Aβ(25-35) dimer was found to be in- or out-of-register antiparallel β-sheet as shown in Fig. 3.4. For Aβ(25-35) trimers an ordered conformation was defined if at least four consecutive residues adopted the β-sheet conformation. According to this criterion, 6 % of all configurations contain large β-sheets formed between all three peptides, and 32 % of all configurations contain a large β-sheet at least formed between two peptides. These ordered aggregates are termed as ordered trimers or dimers, respectively.

The most prominent ordered trimers are conformations #10, #5 and #15, illustrated by the black box in Fig. 3.11. The order corresponds to a decreasing population of this

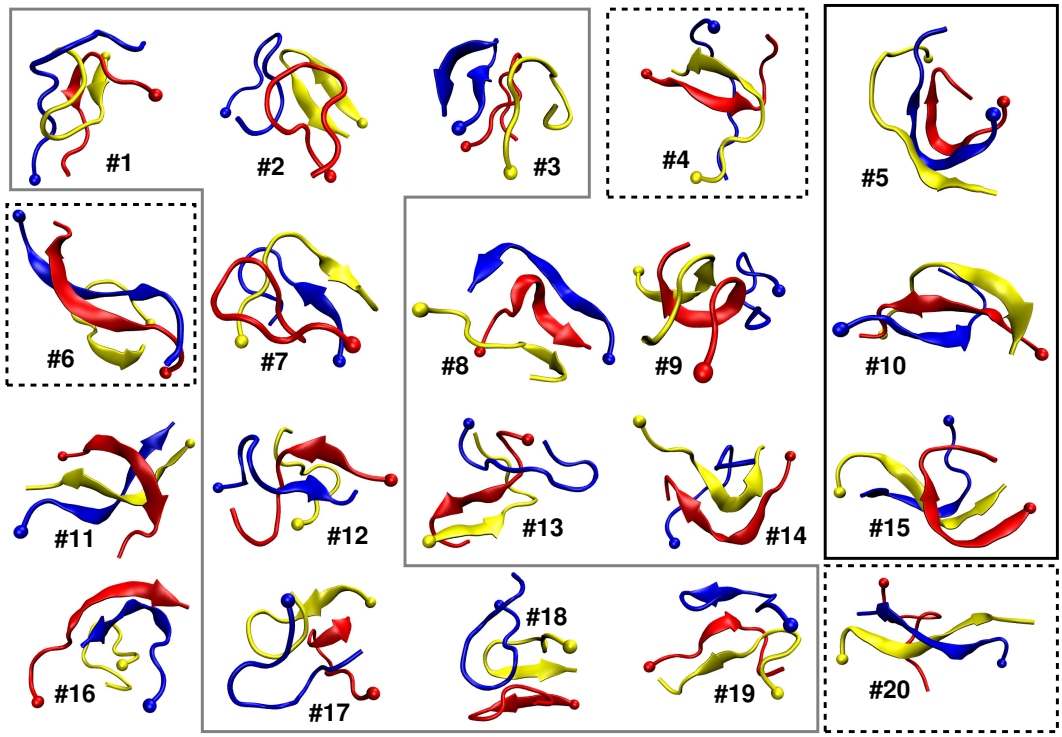

Figure 3.11: Central configurations of the twenty largest out of 469 clusters together containing 42 % of all configurations of the ensemble of Aβ(25-35) trimers at 293 K. Population of clusters given in parenthesis: #1 (4.8 ± 2.3 %), #2 (4.2 ± 1.5 %), #3 (3.0 ± 1.2 %), #4 – #9 (< 3 %), and #10 – #20 (< 2 %). The peptide backbone is shown in ribbon representation; the C_α atom of G25 of each peptide is depicted as a sphere. Configurations in the gray box are characterized by rather little secondary structure. Configurations in the black box correspond to the most prominent ordered trimers whereas the boxes marked with black dashed lines show the most prominent ordered dimers.

conformations by clustering only all ordered trimer configurations. In conformations #10 and #15 antiparallel β-sheets are formed. Additionally, in conformation #15 individual peptides are strongly bent and tilted along the axis perpendicular to the β-sheets. In contrast, conformation #5 shows two strongly bent peptides forming a parallel, V-shaped β-sheet. The third peptide aligns to the parallel V-shaped β-sheet in an antiparallel fashion. Such a parallel V-shaped conformation was found recently also for Aβ(25-35) dimers by Wei *et al.* [124].

Conformations #6, #4, and #20 are the most prominent ordered dimers, see the boxes marked with black dashed lines in Fig. 3.11. In all three conformations antiparallel β-sheets are formed similar to the fibril-like, extended dimer conformations discussed in Sec. 3.4.1. In conformation #6 the third peptide starts to form an antiparallel β-sheet to the ordered dimer.

Most likely in Aβ(25-35) fibrils grown at conditions similar to the simulation setup, individual peptides form extended antiparallel β-sheets. This conformation is mostly stabilized by backbone hydrogen bonds and a strong interaction between the charged residues G25, K28, and M35, as described in Sec. 3.4.3. However, the parallel V-shaped conformation within fibrils seems also possible. Here, stabilization might arise from strong backbone hydrogen bonding, too. The repulsion of similar charged residues might be overcome (i) by the strong bending of the peptides which allows intramolecular interactions between the oppositely charged termini, and (ii) by a change in the orientation of the peptides from parallel to antiparallel every few peptide pairs.

Besides the ordered dimers and trimers in 7 % of all Aβ(25-35) trimers one or two peptides form β-hairpin-like structures similar to conformations #2 or #3. The remaining 55 % of all configurations show neither β-hairpin-like structure nor large β-sheet formation.

3.5.2 Free energy landscape

In contrast to Aβ(25-35) dimers, the radius of gyration is not a useful order parameter to distinguish between different Aβ(25-35) trimer structures. Instead we chose the first two principal components which describe the predominant collective motions within the molecules. A principal component analysis was applied as described in Sec. 2.6.7. Based on the analysis of the cosine content (< 0.0004), the first and second principal components do not correspond to random diffusion [116, 117]. Fig. 3.12 shows the free energy landscape of Aβ(25-35) trimers along the first and second principal component (PC_1,PC_2) together with the location of conformations #1 – #20 shown in Fig. 3.11.

The free energy landscape is very complex, but rather broad. It shows several local minima corresponding to the many different conformations described above. Two broad local minima are found for $PC_1 \approx -10$ nm and $PC_2 \approx -5$ nm, denoted as minimum 1, and at $PC_1 \approx 0$ nm and $PC_2 \approx -2$ nm, denoted as minimum 2, respectively. Both

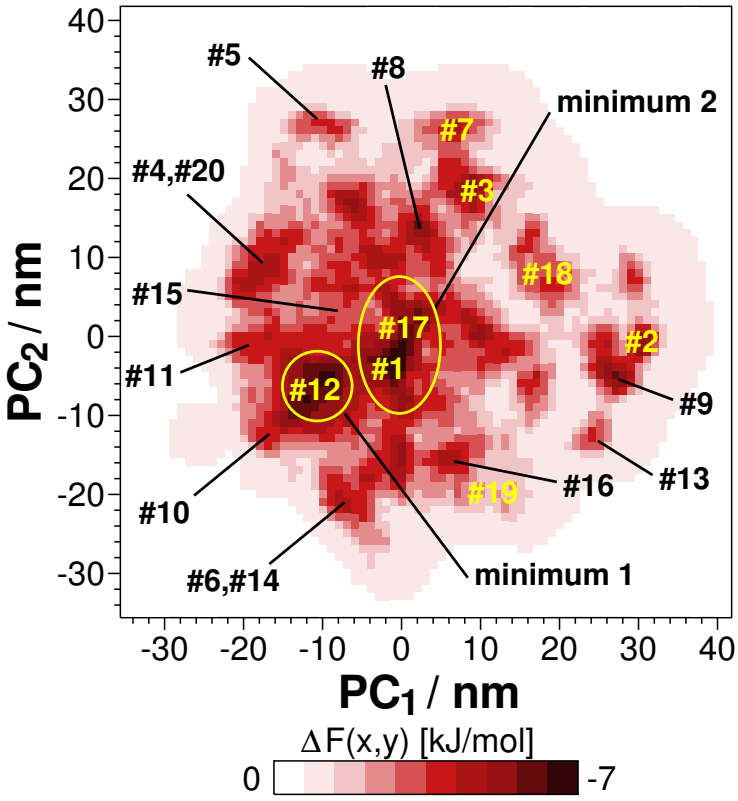

Figure 3.12: Free energy landscape along the first and second principle component (PC_1, PC_2) and the location of the twenty predominant conformations shown in Fig. 3.11. Ordered, β-sheet conformations are marked in black, others in yellow.

minima are approximately 7 kJ/mol deep and are separated by a free energy barrier of roughly 2 kJ/mol. They incorporate poorly structured conformations like #12, or #1 and #17 which will be discussed in the next paragraph in more detail. Interestingly, the ordered dimers and trimers do not correspond to the deepest minima. These conformations are located mostly at the boundary of the free energy landscape and are often of larger free energies than the poorly structured, more disordered conformations. Interestingly, the local minimum of the parallel V-shaped structure (#5) is rather disconnected from the overall free energy landscape by a free energy barrier of roughly 4 to 5 kJ/mol. This might suggest that the formation of parallel V-shaped β-sheets is rather unfavorable.

The minima in the free energy landscape corresponding to positive PC_1 values contain rather compact peptide conformations. Here, β-hairpin-like structures (#2, #3), and U-shaped or bent peptides appear within disordered or ordered aggregates. The

minima containing conformations #2, #9, #13, and #18 are also disconnected from the main free energy landscape by an energy barrier of 4 to 5 kJ/mol. Comparing conformations #2 and #3 shown in Fig. 3.11, there is no obvious difference seen in secondary structure and orientation of the individual peptides to one another. Nevertheless, both conformations are found at different locations within the free energy landscape. According to the lower free energy barriers, conformational rearrangement of aggregated β-hairpin-like conformations to highly ordered β-sheet trimers seems to proceed rather from configurations close to conformation #3 than conformation #2.

Characteristics of the two broad local minima

The question remains, if configurations within the two broad local minima, 1 and 2 in Fig. 3.12, can be distinguished by any conformational features. In the following, any values are calculated as averages over the configurations within one minimum.

Corresponding to the main conformations #12 or #1 and #17, configurations within both minima have only little secondary structure. No significant turn, α-helix, nor intramolecular β-sheet content is observed. On the other hand, the intermolecular β-sheet content adds up to 23 ± 12 % and 18 ± 7 % for minimum 1 and 2, respectively. Configurations within minimum 1 and 2 are bent to 15 ± 7 % and 19 ± 6 %, respectively. However, within the errors the average secondary structure is the same for both minima.

The intermolecular main chain hydrogen bond network averaged over all configurations within each minimum and any possible peptide pairs are shown in Fig. 3.13 for both minima. Both maps reveal that the intermolecular hydrogen bond network is rather weak as the most significant hydrogen bonds appear in only 10-20 % of all configurations within the respective minimum. Nevertheless, the hydrogen bond networks between minimum 1 and 2 differ. Configurations within minimum 1 prefer antiparallel orientation of the peptides by forming main chain hydrogen bonds between N-and C-terminal residues as S26 – M35, N27 – L34, and K28 – G33. In minimum 2 similar antiparallel alignment of the peptides as well as parallel alignment seems possible. The latter is suggested by main chain hydrogen bonds formed between residues S26 – K28 and N27 – A30. It should be noticed that the hydrogen bond map of minimum 2, Fig. 3.13 (b), shows some slight asymmetry which indicates incomplete sampling. Probably, the ensemble of configurations within minimum 2 is more disordered than the ensemble within minimum 1. This means minimum 2 corresponds to a larger conformational space which is more difficult to sample completely.

3.6 Characteristics of increasing oligomer size

This section examines the aggregation process of Aβ(25-35) based on the conformational ensembles of monomers, dimers and trimers at 293 K. Upon aggregation, the change in

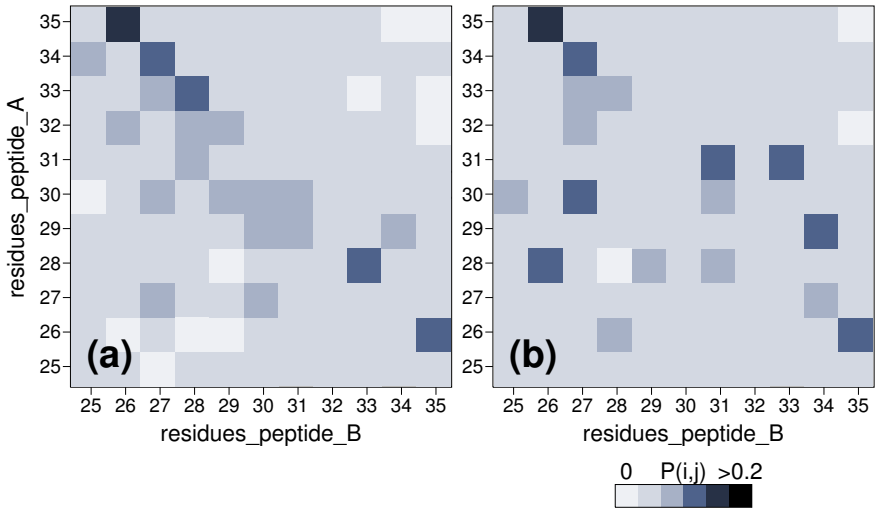

Figure 3.13: Intermolecular main chain hydrogen bond maps of configurations within local minima (a) 1, and (b) 2 shown in Fig. 3.12.

secondary structure, the degree of order in terms of configurational entropy as well as the change in solvent accessible surface area will be discussed in detail.

Tab. 3.3 gives the average secondary structure content for the ensembles of Aβ(25-35) monomers, dimers and trimers at 293 K. This measure gives the average fraction of residues within individual peptides that adopt a certain secondary structure. Independent of the aggregate size individual peptides within all three ensembles are unstructured to 46 – 49 %, and bent to 13 – 15 %. A difference is found for the turn content which is approximately 14 % for monomers, and drops down to 7 % and 5 % for dimers and trimers, respectively. The intramolecular β-sheet content shows similar behavior. While in monomers 17 % of the residues form intramolecular β-sheets, only 6 % and 3 % do so in dimers and trimers, respectively. As discussed in the previous sections Aβ(25-35) forms intermolecular β-sheets upon aggregation. Interestingly, the intermolecular β-sheet content is the same within dimers and trimers, and reaches approximately 21 %.

The change of secondary structure along the amino acid sequence is illustrated in more detail by the secondary structure content of the individual residues shown in Fig. 3.3 for monomers, and Fig. 3.14 for dimers and trimers. As discussed in Sec. 3.3, Aβ(25-35) monomers exist as β-hairpin conformations in equilibrium with unstructured conformations. The β-hairpin motif is characterized by a turn at residues G29 and A30, and intramolecular β-sheets formed between residues N27 – K28 and I31 – I32, shown by the blue and red lines, respectively, in Fig. 3.3. Upon aggregation the initial β-hairpin conformations are gradually dissolved as shown by the decrease in turn and intramolecular

	Monomer	Dimer	Trimer
coil	46(2)	47(1)	49(1)
bend	15(2)	13(1)	15(1)
turn	14(1)	7(1)	5(1)
intra β-sheet	17(2)	6(1)	3(1)
inter β-sheet	–	21(2)	21(1)

Table 3.3: Average secondary structure content of individual peptides within Aβ(25-35) monomers, dimers and trimers at 293 K. Values are given in % with standard errors in parentheses.

β-sheet content of the corresponding residues in Fig. 3.14. Simultaneously, intermolecular β-sheets are formed within oligomers. As mentioned above individual peptides within dimers and trimers have the same average intermolecular β-sheet content. These β-sheets also involve the same residues as shown by the green line in Fig. 3.14. As discussed in sections 3.4.1 and 3.5.1, an antiparallel orientation of the peptides within oligomers is preferred.

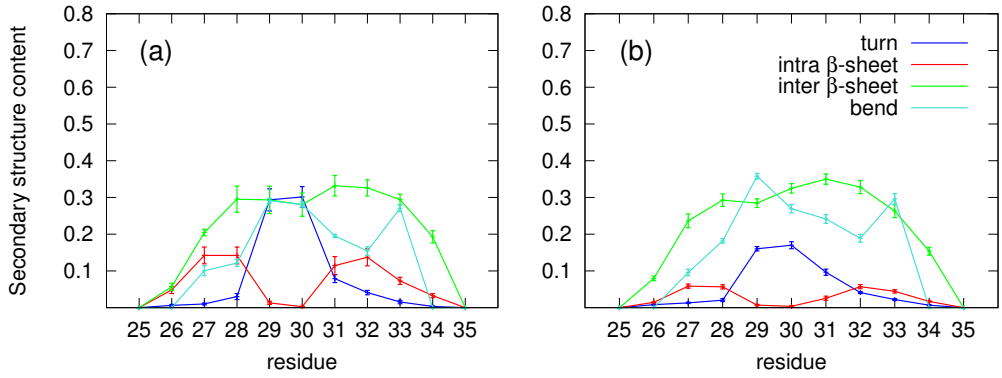

Figure 3.14: Secondary structure content of the individual residues for the ensembles of Aβ(25-35) (a) dimers, and (b) trimers at 293 K. Given are turn, bend, intra- and intermolecular β-sheet content. There was no significant α-helix content observed in both oligomer ensembles.

The following part focuses on the thermodynamics of the aggregation and examines the contributions arising from the peptide entropy and the hydrophobic effect. To properly compare the three systems a second cluster analysis based on all peptide atoms using an RMSD cutoff of 0.25 nm was performed for each system. This RMSD corresponds to the first significant minimum in the RMSD distributions determined for all three systems. The configurational entropy $S_{\mathrm{conf},i}$ with $i = 1$, 2 or 3 for monomer, dimer

system	ΔS_{conf} [J/K mol]	$-T\Delta S_{\mathrm{conf}}$ [kJ/mol]
2M $\rightarrow$ D	-14(6)	4(2)
M + D $\rightarrow$ T	-31(11)	9(3)
3M $\rightarrow$ T	-44(11)	13(3)

Table 3.4: Change in configurational entropy and entropic contribution to the peptide free energy upon aggregation at 293 K with standard errors in parentheses.

and trimer, respectively, was calculated using Eq. 2.34. The change in peptide entropy upon dimerization was estimated from

$$\Delta S_{\mathrm{2M\rightarrow D}} = S_{\mathrm{conf},2} - 2\ S_{\mathrm{conf},1}. \tag{3.4}$$

Similarly, $\Delta S_{\mathrm{M+D\rightarrow T}}$ and $\Delta S_{\mathrm{3M\rightarrow T}}$ were calculated as the change in peptide entropy upon aggregation of one dimer and one monomer, and three monomers. The obtained values of ΔS_{conf} and $-T\Delta S_{\mathrm{conf}}$ are given in Tab. 3.4. In general, the loss in configurational entropy increases with the size of the formed oligomer, and therefore $-T\Delta S_{\mathrm{conf}}$ increases. Hence, the configurational entropy disfavors aggregation. In particular, the aggregation of three monomers to a trimer, which is very unlikely, corresponds to the highest cost in peptide entropy. Concerning the errors only the dimerization 2M $\rightarrow$ D and the trimerization 3M $\rightarrow$ T can be distinguished.

In contrast, aggregation is expected to be favored by the hydrophobic effect arising from an increase of water entropy due to a reduction of peptide surface area. The hydrophobic and hydrophilic solvent accessible surface area, and the free energy of solvation were calculated for each system as described in Sec. 2.6.5. The change of these properties upon aggregation is given in Tab. 3.5. During aggregation the hydrophobic as well as the hydrophilic surface area decrease, while the change in SASA increases with the size of the formed oligomer. The aggregation of three monomers causes the highest decrease in SASA. For each aggregation system the change in hydrophobic surface area exceeds the change in hydrophilic surface area. Hence, as illustrated by the resulting solvation free energies, trimerization is favored over dimerization. The decrease in solvation free energy is larger for the aggregation of 3M $\rightarrow$ T than for M + D $\rightarrow$ T.

The net contribution to the aggregation free energy due to the peptide entropy and the hydrophobic effect $\Delta F_{\mathrm{agg}} = -T\Delta S_{\mathrm{conf}} + \Delta F_{\mathrm{solv}}$ adds up to -8 ± 3 kJ/mol for 2M $\rightarrow$ D, and M + D $\rightarrow$ T. The aggregation of three individual monomers is even more favored by $\Delta F_{\mathrm{agg}} = -16 \pm 3$ kJ/mol, but is very unlikely to happen as mentioned above.

system	hydrophobic ΔSASA [nm^2]	hydrophilic ΔSASA [nm^2]	total ΔF_{solv} [kJ/mol]
2M → D	-1.94(0.07)	-1.17(0.04)	-11.7(0.5)
M + D → T	-2.83(0.08)	-1.70(0.09)	-16.8(0.6)
3M → T	-4.8(0.1)	-2.9(0.1)	-28.5(0.8)

Table 3.5: Change in hydrophobic and hydrophilic solvent accessible surface area (ΔSASA) and the corresponding solvation free energy (ΔF_{solv}) upon aggregation at 293 K with standard errors in parentheses.

3.7 Conclusions

In this chapter conformational details and thermodynamics of Aβ(25-35) monomers and early aggregation intermediates as dimers and trimers in water were discussed. The very few experimental data available were obtained at room temperature, therefore analyses focused on ensembles at 293 K.

The simulation of Aβ(25-35) monomers corresponds to the preaggregated state at very low peptide concentrations. At 293 K the ensemble populates two types of β-hairpin conformations as well as coiled structures as shown in Fig. 3.2. The β-hairpin structures are characterized by a β-turn involving residues G29 and A30, and two short antiparallel β-strands consisting of residues N27 – K28 and I31 – I32, as illustrated by the secondary structure content of individual residues in Fig. 3.3. The two types of β-hairpins differ in the twist of the strands to one another. These results agree with a previous theoretical study which started from a different initial configuration [62].

Additionally, in the same study also reports simulations of the peptide in an apolar HFIP/water mixture using the GROMOS96 43a1 force field and yielding an α-helical conformation in agreement with experiments [62, 63]. Therefore, and especially since the GROMOS96 43a1 force field is known to overestimate the β-sheet content, the bias on the present results due to the chosen force field is assumed to be small. Additionally, the effect of overestimated β-sheet content is less pronounced if as in the present simulations the reaction field method is used to calculate electrostatic interactions [133].

From an entropic point of view prestructured conformations are more prone for aggregation than fully unstructured conformations. In order to start aggregation from rather predominant conformations, either of the two β-hairpin conformations were used as initial configurations for oligomerization.

As expected, a cluster analysis based on the RMSD in structure yielded many poorly populated conformations for the ensembles of Aβ(25-35) dimers and trimers as shown in Figs. 3.4 and 3.11. Nevertheless, we were able to differentiate between disordered and fibril-like oligomers. In case of Aβ(25-35) dimers the radius of gyration as a measure of

the extension of the peptides has been used to distinguish between compact, disordered and extended, fibril-like dimers which were observed at a ratio of 3:1 as shown by the free energy landscape in Fig. 3.5. The compact dimers contain β-hairpin-like, U-shaped or unstructured peptides connected by rather unspecific contacts. In fibril-like dimers peptides are fully extended and form in- or out-of-register antiparallel β-sheets, compare with Figs. 3.6 and 3.7.

The ensemble of Aβ(25-35) trimers is more complex as illustrated by the free energy landscape along the first and second principal components shown in Fig. 3.12. Approximately 38 % of the configurations were determined as ordered aggregates forming large intermolecular β-sheets. Among them most prominent are aggregates containing extended, antiparallel β-sheets similar to fibril-like dimers while a small amount of aggregates contained V-shaped peptides forming parallel β-sheets. Both types of fibril-like aggregates were also observed in a recently published study [124]. Interestingly, the dimensions of both aggregates, extended and V-shaped, correspond well to the diameters of two distinct morphologies observed for Aβ(25-35) fibrils, 3.58 ± 1.53 nm and 1.41 ± 0.48 nm [65]. Both aggregates also agree with H/D exchange NMR measurements on Aβ(25-35) fibrils that suggest an antiparallel out-of-register or parallel in-register alignment of the peptides [64].

If the predominant β-hairpin conformations of monomers are most likely to aggregate, the compact, disordered dimers can be assumed to be the very first aggregates formed. They will aggregate further or transform into fibril-like extended dimers. A thermodynamic analysis, discussed in Sec. 3.4.3, indicated that the transition from compact, disordered to extended, fibril-like Aβ(25-35) dimers is unfavorable as the gain in potential energy in extended dimers is overcompensated by a loss in entropy. The lower energy of the extended dimers with peptides in antiparallel alignment results in favorable intermolecular hydrogen bonding and stronger interactions between the charged termini G25 and M35, and the charged residue K28, see Tab. 3.2. Approximately 25 % of the entropic cost paid upon formation of fibril-like dimers corresponds to configurational entropy, while the rest relates to solvent entropy. The decrease in solvent entropy is presumably due to (i) the hydrophobic effect as the hydrophobic surface area changes by 0.53 ± 0.07 nm^2 and (ii) electrostatic effects. Additionally, we found that the transition towards fibril-like dimers is presumably mediated by main chain hydrogen bonds between the former turn residues G29 and A30 and side chain interactions between the I31 residues of both peptides, as illustrated by Figs. 3.8 and 3.9.

REMD simulations do not provide the kinetics of the system. Nevertheless, structural and thermodynamic properties of the individual ensembles of Aβ(25-35) monomers, dimers and trimers at 293 K were compared in oder to gain qualitative information about the aggregation process as discussed in Sec. 3.6. Starting from the β-hairpin conformation observed for monomers, this structure motif is successively dissolved in dimer and

trimer ensembles, compare Figs. 3.3 and 3.14. This agrees well with experiments that showed, that the initially observed β-turn content in Aβ(25-35) solutions decreased under further incubation [120, 121, 126]. The formation of fibril-like oligomers is characterized by the formation of intermolecular β-sheets. In the simulations, the average intermolecular β-sheet content is the same for dimers and trimers, and reaches approximately 21 %, see Tab. 3.3.

The net contribution to the aggregation free energy arising from configurational entropy and solvation free energy was dissected. As expected upon aggregation the configurational entropy decreases as more ordered, β-sheet-rich oligomers are formed, as shown in Tab. 3.4. Additionally, the solvent accessible surface area, especially the hydrophobic SASA, decreases yielding a favorable solvation free energy, see Tab. 3.5. The gain in solvation free energy is large enough to overcompensate the loss in configurational entropy. In summary, the hydrophobic effect, possibly combined with electrostatic effects, yields an increase in solvent entropy which is believed to be one major driving force towards aggregation. An exact determination of the energetic contributions was not possible. Consequently, it remains unclear to which extent aggregation of Aβ(25-35) is also influenced by energy.

Chapter 4

Simulation Results for Aβ(10-35)-NH_2 Monomers

This chapter discusses simulations of Aβ(10-35)-NH_2 monomers in aqueous environment using two different force fields. The simulations were utilized to determine the conformation of the preaggregated state depending on the applied force field. The results will be compared to experimental NMR data available. But first, important previous experimental and theoretical work on this subject will be given.

4.1 Previous experimental and theoretical observations

The 10 – 35 fragment of the Aβ peptide, precisely Aβ(10-35)-NH_2, was found to mimic the characteristics, i.e. plaque competence, of the full-length Aβ peptide [71]. As this fragment also shows improved water solubility, it provides an alternative model for high-resolution structure – function studies of the Aβ peptide in water solution. The amino acid sequence of Aβ(10-35) is shown as part of the sequence of the full length peptide in Fig. 1.6 in Sec. 1.2.1. The peptide is of amphiphilic nature with highly hydrophobic regions involving residues L17 – A21 and G29 – M35, it also contains three acidic, and four basic residues. Residues K16 – F20 are also known as self-recognition site [66] which might form initial contacts in early aggregation intermediates.

Lee *et al.* studied the plaque competence of Aβ(1-28)-OH and Aβ(10-35)-NH_2 in aqueous solution depending on the pH [71]. While both fragments where inactive below pH 4, only Aβ(10-35)-NH_2 showed increased plaque formation between pH 4 and 9, and most distinct at pH 5.6. Accordingly, the first nine and the last five residues of the full length Aβ peptide seem not essential for plaque formation.

Lee *et al.* and Zhang *et al.* collected complete sets of NMR spectra for both fragments at pH 2.1 and 5.6 at 283 K [54, 71]. At pH 5.6, chemical shift indices provided no evidence of α-helical or β-sheet structure for the active Aβ(10-35)-NH_2 peptide. Nevertheless,

NOE correlations and $^3J_{H^N H^\alpha}$ scalar coupling constants indicate, that Aβ(10-35)-NH_2 adopts a compact conformation under these conditions.

Structural calculations mostly based on interresidue NOE restraints resulted in 15 model conformations, published under PDB code 1HZ3. These model conformations are characterized as collapsed coils containing a well-structured central hydrophobic cluster (CHC) involving residues L17 – A21. All residues within the CHC except V18 contribute to a large, uninterrupted hydrophobic patch which covers approximately 25 % of the peptide surface. The remaining backbone of Aβ(10-35)-NH_2 exists as a series of loops and turns partially condensed about the CHC foundation [54]. The most robust turn stretches from residues V24 to N27. The absence of regular repeating secondary structure and large amide hydrogen exchange rates provided sufficient evidence for the lack of intramolecular hydrogen bonding to contribute to conformational stability. Zhang *et al.* suggested stabilization rather to depend upon a combination of intramolecular van der Waals interactions, and minor contributions from coulombic interactions.

Previous all-atom MD simulation studies of Aβ(10-35) monomers in explicit solvent were performed mostly using two different approaches, (i) monitoring the stability of the NMR-derived structure models at certain conditions, and (ii) testing if the NMR structure models can be reproduced by simulations starting from fully extended conformations.

The most important study following the first approach is the work by Han and Wu [115]. They simulated Aβ(10-35)-NH_2 starting from the 1st or 9th NMR model using the GROMOS96 43a1 force field at pH 2.0 and 5.6 and temperatures of 300 and 400 K over a 1.2 μs timescale. To some extent they achieved agreement with the NMR experiments, as in the MD simulations at 300 K the collapsed coil structure was unstable at pH 2 and metastable for about 200 ns at pH 5.6. Among other factors, they suggest the collapsed coil conformation of Aβ(10-35)-NH_2 monomers to be stabilized by H13/H14 – E22/D23 salt bridges. Coexisting with the collapsed coil conformation they observed the reversible formation of a predominant strand-loop-strand (SLS) conformation. It is characterized by a turn at V24 – N27, at least one contact between F19/F20 and I31/I32, and the CHC and the C-terminus in antiparallel contact. The SLS conformation does not depend on H13/H14 – E22/D23 salt bridges and has higher thermostability than the collapsed coil NMR structure. The MD simulations at pH 5.6 yielded 85 % agreement with the NOE restraints from experiments [54].

A recent study following the second approach was presented by Baumketner *et al.* [134]. In order to observe spontaneous folding, they started from a fully extended conformation. Using the OPLS/AA force field and different initial velocities they started five REMD simulations each using 72 replicas simulated at temperatures ranging from 280 to 580 K. Allowing 5 ns of equilibration and 7 ns of sampling all together 35 ns of data were collected at 280 K. From their report it is not clear which charge state for the

histidine residues was chosen. They tested the influence of the protonation by performing 2.5 ns long MD simulations starting from the 1st NMR structure model, and both histidines either single or double protonated. Based on the RMSD to the initial conformation, they observed a structural instability of the NMR-derived conformation for both protonation states while the conformation containing double protonated histidines was slightly more stable. According to this result they suggested that the charge state of the histidines would not significantly influence the conformational states of Aβ(10-35)-NH_2, at least on the nanosecond timescale. Presumably, they performed the REMD simulations using uncharged, single protonated histidines. At 280 K, Baumketner *et al.* found no well defined main conformation of Aβ(10-35)-NH_2 close to the collapsed coil structure solved by NMR. Nevertheless, similar to the NMR results, they found no significant α-helical or β-sheet structure, and 50 % agreement with experimental long-range NOE distances.

The present work studies the equilibrium conformation of Aβ(10-35)-NH_2 at experimental conditions using the second approach similar to Baumketner *et al.*. Extensive REMD simulations over 70 and 105 ns per replica were applied. This should be sufficient in order to sample a large ensemble of conformations and to allow reversible transformations on the ns timescale between possible predominant conformations. Additionally, simulations were utilized using two different forcefields, GROMOS96 43a1 and OPLS/AA [92, 93]. The two sampled ensembles are compared to the NMR-derived collapsed coil conformation and primary NMR data such as NOE distances and ${}^3J_{H^N H^\alpha}$ coupling constants.

4.2 Setup for two different force fields and equilibration

The Aβ(10-35)-NH_2 monomer was modeled in aqueous environment at pH 5.6 similar to the NMR experiments [54, 71]. The amino acid sequence of the peptide is shown in Fig. 1.6 in Sec. 1.2.1. To mimic pH 5.6, the protonation of the peptide was chosen as follows: a positively charged N-terminus, three negative charges on E11, E22 and, D23, and four positively charged residues H13, H14, K16 and K28, whereas the C-terminus is amidated. In particular, the histidines were chosen to be double protonated, according to the expected pK_a values of histidines within proteins of $6.5-7$ [135].

First, an MD simulation using the GROMOS96 43a1 force field was started from an extended peptide conformation placed in a cubic box aligned to the diagonal. To counterbalance the positive charge of the peptide two chloride ions were added. The remaining space was filled by 11267 SPC water molecules [94, 95]. After an energy minimization the system was simulated for 1 ns at 293 K and 1 bar with position restraints on the peptide atoms. Both procedures are described in Sec. 2.5 and Sec. 2.3.4, respectively. Then the system was simulated for 7 ns without restraints at 283 K and

Simulation system	force field	N_w	water model	N_{Cl^-}	run time
Aβ1035/GRO	GROMOS96 43a1	5959	SPC	2	105 ns
Aβ1035/OPL	OPLS/AA	5871	TIP4P	2	70 ns

Table 4.1: Simulation setups for production runs. N_w and N_{Cl^-} give the number of water molecules and chloride ions, respectively. Run time gives the reached simulation time of individual replicas.

1 bar providing a fully collapsed peptide configuration in an equilibrated water volume. This peptide configuration served as initial structure for studies using two different force fields, GROMOS96 43a1 and OPLS/AA [92, 93].

For each force field study the collapsed peptide was dissolved in a dodecahedral box such that the minimum distance between the solute and the boundaries of the box was 1.5 nm. The remaining space was filled by two chloride ions and water molecules, while the SPC and TIP4P water models were used [95, 96]. The detailed simulation setups are shown in Tab. 4.1. For both systems, high temperature MD simulations at 400 K and constant volume provided 62 randomly chosen configurations as initial configurations for the REMD simulations. Before starting the REMD algorithm each replica was equilibrated at its temperature for 5 ns.

For both systems, Aβ1035/GRO and Aβ1035/OPL, 62 replica were simulated at constant volume and temperatures forming a geometric sequence between 281 and 400 K for 105 ns and 70 ns each, respectively. Correlated back exchanges were avoided by attempting to swap replica between neighboring temperatures every 6 ps.

The dihedral angle ϕ of individual residues is the important parameter in order to calculate ${}^3J_{H^N H^\alpha}$ scalar coupling constants as will be discussed in Sec. 4.4. The convergence of the simulations was determined according to the stability of the ϕ dihedral angle distributions. Both systems reached equilibrium at 283 K within 25 ns. Within the sampling period the distributions remain unchanged which is shown in Fig. 4.1 for both force fields and residues L17, and A30, both belonging to large hydrophobic regions of the peptide. Therefore further analysis focused on the final 80 ns (Aβ1035/GRO) and 45 ns (Aβ1035/OPL) at 283 K, respectively.

4.3 Analysis of conformational clusters

For each simulation, Aβ1035/GRO and Aβ1035/OPL, the main conformations were determined using the cluster analysis by Daura *et al.*, see Sec. 2.6.4. The criterion for the cluster algorithm was chosen as follows: RMSD cutoff of 0.15 nm for backbone atoms of residues K16 – G29. According to the structural model derived from the NMR data, these residues represent the ordered core region of the molecule containing the CHC

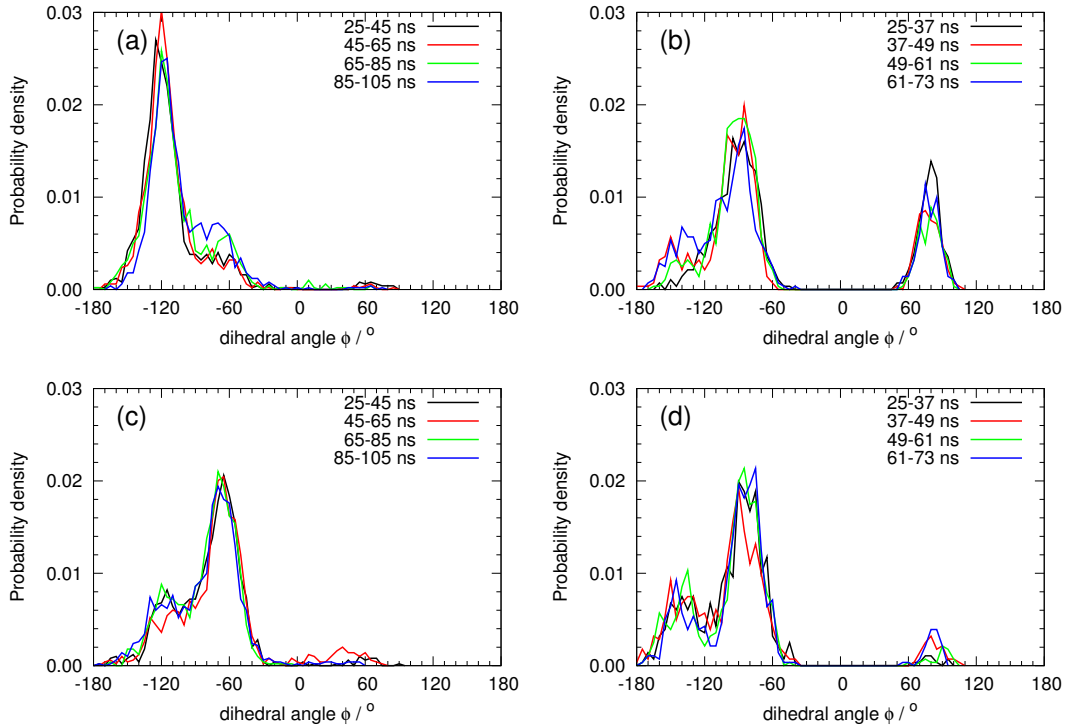

Figure 4.1: Convergence of Aβ1035/GRO and Aβ1035/OPL according to distributions of the dihedral angle ϕ for four blocks of each trajectory. Shown are distributions for residues (a) L17, and (c) A30 for Aβ1035/GRO, and (b) L17, and (d) A30 for Aβ1035/OPL.

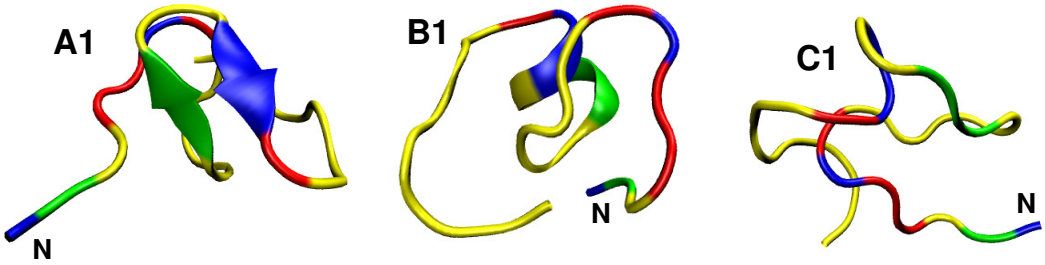

Figure 4.2: Central configurations of the three most populated out of 70 clusters together containing 41 % of all configurations of Aβ(10-35)-NH_2 monomers generated by Aβ1035/GRO at 283 K. Population of clusters are given in parentheses: *A1* (26 ± 3 %), *B1* (8 ± 2 %), *C1* (7 ± 2 %). The peptide backbone is shown in ribbon representation; the color coding of the amino acids is as follows: nonpolar residues in yellow, polar ones in blue, positively charged ones in red , and negatively charged ones in green.

(L17 – A21) and the most robust turn (V24 – N27) [54]. The cluster analysis yielded 70 clusters for Aβ1035/GRO and 77 clusters for Aβ1035/OPL. Figs. 4.2 and 4.3 show the central configurations of the three most populated clusters for both systems which will be discussed in detail in the following.

For Aβ1035/GRO, the main conformation *A1* is populated by 26 ± 3 % of all configurations. It is mostly unstructured but contains a small β-hairpin with the turn located at residues V24 and G25, and a short antiparallel β-sheet between residues E22 – D23 and S26 – N27. Interestingly, the structured region within *A1* is similar to the secondary structure determined for SLS conformations found in previous MD simulations [115] as discussed in Sec.4.1. Within SLS conformations a loop is located at V24 – S26 and the antiparallel β-sheet includes residues L17 – D23 and N27 – M35. Conformation *B1* of Aβ1035/GRO is populated by 8 ± 2 % of all configurations. In this conformation the same region as within *A1* is structured while here the residues form an α-helix. Conformation *C1*, populated by 7 ± 2 % of all configurations, is fully unstructured. The average RMSD of the backbone atoms of residues K16 – G29 to the 1st NMR-derived model is similar for all the configurations within each of the three clusters, with an RMSD of 0.4 to 0.5 $\pm$ 0.1 nm.

Contrary to Aβ1035/GRO, for Aβ1035/OPL no highly populated main conformation is found. The first three clusters are all populated by approximately 7 % of all configurations, as shown in Fig. 4.3. Only conformation *A2* is partly structured containing a short parallel β-sheet between residues Q15 – K16 and G33 – L34, which was not observed in previous simulations or experiments. Both conformations *B2* and *C2* are fully unstructured but contain several loops. For all configurations within each cluster the RMSD of the backbone atoms of residues K16 – G29 to the 1st NMR-derived model was

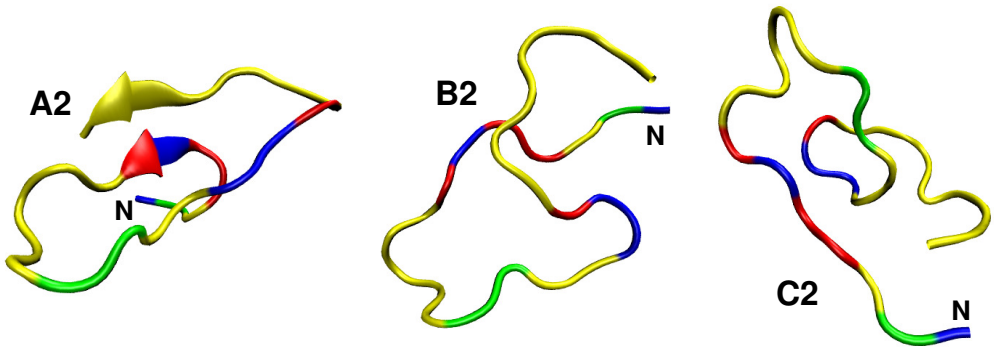

Figure 4.3: Central configurations of the three most populated out of 77 clusters together containing 21 % of all configurations of Aβ(10-35)-NH_2 monomers generated by Aβ1035/OPL at 283 K. Population of clusters are given in parentheses: *A2* (7 ± 3 %), *B2* (7 ± 2 %), *C2* (7 ± 1 %). The peptide backbone is shown in ribbon representation; the color coding of the amino acids corresponds to that given in Fig. 4.2.

	coil	bend	turn	β-sheet	β-bridge	α-helix
Aβ1035/GRO	43(3)	33(2)	10(2)	8(1)	6(1)	0.3(0.2)
Aβ1035/OPL	50(3)	30(2)	12(2)	5(2)	3(1)	0.2(0.2)

Table 4.2: Average secondary structure content within Aβ(10-35) monomers of Aβ1035/GRO and Aβ1035/OPL at 283 K. Values are given in % with standard errors in parentheses.

determined. The RMSD is smallest for the third cluster, with RMSD $= 0.4 \pm 0.1$ nm, and increases for the second and first cluster up to 0.6 ± 0.1 nm.

Secondary structure content

Based on the conformations populated by both ensembles, it could be assumed that conformations within the ensemble of Aβ1035/GRO are more structured in general. The average secondary structure content for both systems given in Tab. 4.2 reveals that this is not the case. Although, Aβ1035/OPL shows a slightly higher coil and lower β-bridge content than Aβ1035/GRO, all other secondary structure motifs appear in a similar amount within the errors.

On the other hand, corresponding to the different main conformations found for both systems the secondary structure content for the individual residues differs between the ensembles as shown by Fig. 4.4. For Aβ1035/GRO, residues E22 – N27, forming the β-hairpin in conformation *A1*, have the highest β-sheet and turn content, and also the only significant α-helix content. Only a few N- and C-terminal residues as H13, H14, and I31

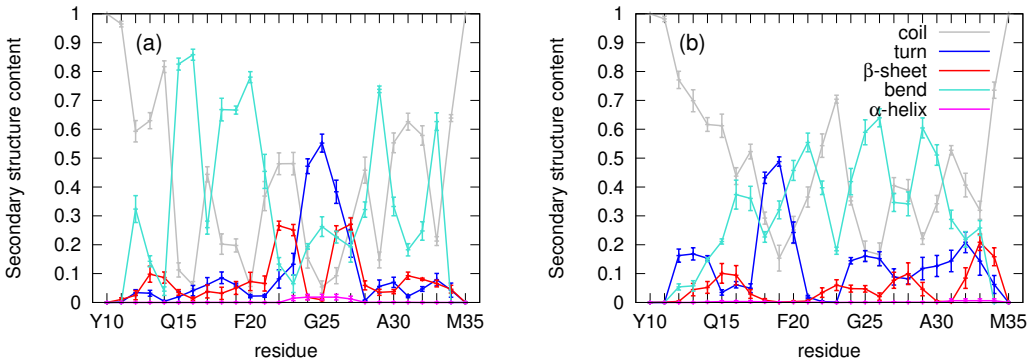

Figure 4.4: Secondary structure content of individual residues for the ensemble of (a) Aβ1035/GRO, and (b) Aβ1035/OPL at 283 K. Given are coil, bend, turn, β-sheet, and α-helix content.

show a slightly increased β-sheet content in up to 10 % of all configurations. Interestingly, on average residues V24 to N27 have the highest turn content corresponding to the most robust turn determined within the NMR-derived models [54]. For Aβ1035/OPL, shown in Fig. 4.4 (b), a β-sheet content of at least 10 % is observed for residues Q15, K16, N27, K28, and I32 – L34. In configurations sampled by the OPLS/AA force field most of the inner residues are either bent or show a significant turn formation. For more than 10 % of all configurations a turn conformation is adopted by residues V12 – H14, V18 – F20, V24 – I32.

In summary, the two force fields yield different results and none of the most populated main conformations corresponds well to the NMR-derived collapsed coil structure models. Therefore, in the following section both ensembles are compared to primary NMR data such as inter proton distances, so-called NOE distances, and $^3J_{\mathrm{H^N H^\alpha}}$ scalar coupling constants.

4.4 Comparison with experimental NMR data

Several parameters that can be measured by NMR spectroscopy are sensitive to the molecular conformation [136]. The most commonly utilized parameters for protein structure determination are dipolar cross relaxation rate constants, scalar coupling constants, isotropic chemical shifts, and residual dipole-dipole coupling constants (RCDs) [137, 138, 139]. Structural restraints are also provided by amide proton-solvent exchange protection factors [140], *trans*-hydrogen bond scalar coupling constants [141], and paramagnetic effects [142, 143, 144].

This section focuses on two NMR experiments performed for Aβ(10-35)-NH$_2$ by Lee *et*

al. and Zhang *et al.* which among other parameters provide NOE distances and $^3J_{\mathrm{H^N H^\alpha}}$ scalar coupling constants [54, 71]. The following sections discuss to which extent the experimental data can be reproduced by the REMD simulations using the two different force fields.

4.4.1 NOE distances

The nuclear Overhauser effect (NOE) describes the through-space dipolar coupling of nuclear spins *via* cross-relaxation. It is characterized by the cross-relaxation rate constant. This constant is proportional to the inverse sixth power of the distance between two interacting ^{1}H spins and can therefore be used to determine inter proton distances. Based on the relation between the cross-relaxation rate constant and the inter proton distance, it is obvious that the cross relaxation signal becomes weaker with increasing distance. Depending on the signal to noise ratio very weak signals or large NOE distances should be taken with care. A long mixing time, which is the time needed to transfer magnetization from one spin to the other, can enhance such signals but can also allow spin diffusion which can result in inaccurate NOE distances. Typically, mixing times should be in the order of 50 to 150 ms yielding reliable NOE distances smaller than 5 Å [136, 145]. Both experimental groups used mixing times of 75, 80 and 150 ms [54, 71].

From the cross relaxation signals upper bound separations of the interacting protons are determined. The NOE cross peak intensities are grouped into strong, medium, and weak signals associated with upper bound separations of 2.7 Å, 3.3 Å, and 5.0 Å [136]. The upper bounds serve as restraints in structure refinements. The model configurations should violate as less restraints as possible and be low in energy. A NOE violation appears if the NOE distance in the model structure is larger than the experimentally obtained upper bound separation.

From simulations NOE distances can be calculated as averages of the corresponding inter proton distances over the pool of configurations generated. More precise, the NOE distance between interacting protons i and j is given by

$$d_{\mathrm{NOE},ij} =< 1/r_{ij}^6 >^{-1/6}, \tag{4.1}$$

with r_{ij} being the distance between those protons. For proteins and peptides, based on the location of protons i and j along the sequence, NOE distances are classified as sequential (i and j are located on consecutive residues n and $n+1$), medium- (on residues n and $n+2$ or $n+3$), and long-range distances (on residues n and $> n+3$).

For structural calculations of Aβ(10-35)-NH_2 at pH 5.6 and 283 K Zhang *et al.* have used 84 sequential, 66 medium-, and 32 long-range restraints [54] resulting in 15 NMR models (PDB code 1HZ3). Out of all these restraints 30 long-range and 56 medium-range NOE distances were calculated for both force field systems using Eq. 4.1. The number of NOE violations for the two sampled ensembles are given in Tabs. 4.3 and

4.4. For comparison, the NOE violations of the 15 NMR-derived models, and the previous simulation study by Baumketner *et al.* are also shown [54, 134]. The latter used the OPLS/AA force field but applied a different simulation procedure compared to the present work, see Sec. 4.1. They only discussed violations of long-range NOEs in their report.

Long-range NOE distances

Shown in Tab. 4.3, only five of the thirty long-range NOE distances are violated by the NMR-derived models. Both simulated ensembles show reasonable agreement with the long-range NOE restraints: sixteen (Aβ1035/GRO) or ten (Aβ1035/OPL) of the thirty long-range distances are fully satisfied, while only seven (Aβ1035/GRO) or five (Aβ1035/OPL) distances are violated by more than 2 Å. Values in parentheses given in Tab. 4.3 are the number of upper bounds ≤ 5 Å corresponding to the weakest reliable NOE cross relaxation signals [136, 145]. Only two long-range NOE distances correspond to this criterion. They are violated by both simulated ensembles, while Aβ1035/OPL causes less large NOE violations than Aβ1035/GRO. A detailed list of all corresponding long-range distances and their violations can be found in Tab. A.1 given in appendix A. It is shown there that approximately 30% of the violations differ between the force fields. Presumably, this corresponds to different equilibrium conformations reached depending on the force field as discussed in Sec. 4.3.

The REMD simulation performed by Baumketner *et al.* gives a similar result as Aβ1035/GRO or Aβ1035/OPL although they applied a shorter sampling period [134]. As mentioned in Sec. 4.1, Baumketner *et al.* used a similar setup but a different sampling procedure. As shown in Sec. 4.2, Aβ1035/GRO and Aβ1035/OPL require an equilibration time of at least 25 ns. Therefore, it is very unlikely that the REMD simulations by Baumketner *et al.* converged within 5 ns. Their reasonable agreement with the experimental long-range NOE restraints can be explained by a higher probability of non-equilibrated configurations containing short inter proton distances. As $d_{\mathrm{NOE},ij}$ is proportional to $1/r_{ij}^6$, any very small inter proton distance decreases $d_{\mathrm{NOE},ij}$ dramatically and results in false agreement with the upper bound restraints. This fact was tested for Aβ1035/GRO allowing no equilibration and sampling for 20 ns. The resulting long-range NOE distances given in Tab. 4.3 do indeed show slightly better agreement with the experiment than the NOEs resulting from the equilibrated ensembles, as expected.

Medium-range NOE distances

Violations of the 56 medium-range NOE distances are listed for the NMR models, Aβ1035/GRO, and Aβ1035/OPL in Tab. 4.4. Again Aβ1035/GRO and Aβ1035/OPL show reasonable agreement with the NMR-derived NOE restraints, while the system

NOE violation [Å]	NMR models	Aβ1035/GRO		Aβ1035/OPL	Ref. [134]
≤ 0	25(1)	16(0)	17(0)*	10(0)	15(0)
$0 < x \leq 1$	3(1)	2(0)	2(0)*	7(1)	6(0)
$1 < x \leq 2$	2(0)	5(0)	6(0)*	8(0)	5(1)
$x > 2$	0(0)	7(2)	5(2)*	5(1)	4(1)

Table 4.3: Violations of 30 long-range NOE distances by the 15 NMR models [54], Aβ1035/GRO, Aβ1035/OPL, and a previous REMD simulation study by Baumketner *et al.* [134]. Values in parentheses give the corresponding numbers of upper bounds $\leq$ 5 Å. Values marked with * correspond to NOE distances determined for Aβ1035/GRO allowing no equilibration and a sampling period of 20 ns.

NOE violation [Å]	NMR models	Aβ1035/GRO	Aβ1035/OPL
≤ 0	42(9)	34(3)	35(5)
$0 < x \leq 1$	8(4)	8(2)	15(6)
$1 < x \leq 2$	6(2)	8(4)	3(1)
$x > 2$	0(0)	6(6)	3(3)

Table 4.4: Violations of 56 medium-range NOE distances by the 15 NMR models [54], Aβ1035/GRO, and Aβ1035/OPL. Values in parentheses give the corresponding numbers of upper bounds $\leq$ 5 Å.

using the OPLS/AA force field gives a slightly better result. Considering only upper bound separations $\leq$ 5 Å given in parentheses in Tab. 4.4, the better agreement of Aβ1035/OPL with the NMR-derived restraints becomes even more apparent. A detailed list of medium-range distances is given in Tab. A.2 in appendix A. In contrast to the long-range distances most of the violations of medium-range restraints for the two force fields are similar.

4.4.2 $^3J_{\mathrm{H^N H^\alpha}}$ scalar coupling constants

Spin-spin or scalar coupling between two nuclei is mediated by the electrons forming the chemical bonds between the nuclei [136]. The strength of the interaction is given by the scalar coupling constant $^nJ_{ab}$, in which n corresponds to the number of covalent bonds separating the two spins a and b. Karplus was the first to describe the relationship between the magnitude of a ^3J scalar coupling constant and the dihedral angle θ formed by the three covalent bonds [146]. The so-called Karplus Equation is given by

$$^3J = A\ \cos^2\theta + B\ \cos\theta + C, \tag{4.2}$$

where the constants A, B, and C depend upon the particular nuclei involved.

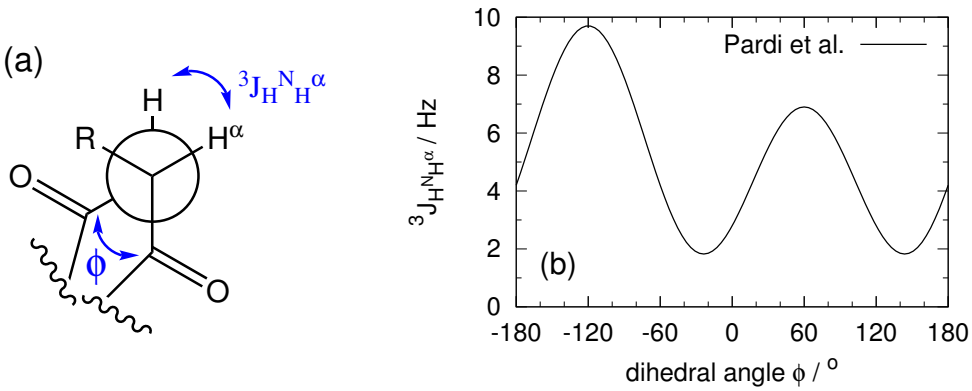

Figure 4.5: (a) Newman projection of a polypeptide chain along the $C^{\alpha}-N$-bond, and correlation between the dihedral angle ϕ and ${}^3J_{H^N H^{\alpha}}$. (b) ${}^3J_{H^N H^{\alpha}}$ as function of ϕ using the Karplus equation, given in Eq. 4.2, with parameters derived by Pardi *et al.*, where $A = 6.4$ Hz, $B = -1.4$ Hz, $C = 1.9$ Hz, and $\theta = \phi - 60°$ [147].

Common for proteins or peptides, the coupling between the amide proton and the H^{α} proton of individual amino acids is measured by the scalar coupling constant ${}^3J_{H^N H^{\alpha}}$. Fig. 4.5 (a) shows a Newman projection of a polypeptide chain along the C^{α}-N bond. This picture illustrates the scalar coupling between the amide proton and the H^{α} proton which is correlated to the dihedral angle ϕ. To calculate ${}^3J_{H^N H^{\alpha}}$ using the Karplus relationship Pardi *et al.* derived the Karplus constants from protein structures determined by X-ray crystallography or NMR spectroscopy [147]. They correlated observed ${}^3J$ values for these proteins with the corresponding dihedral angles found in the structures. For ${}^3J_{H^N H^{\alpha}}$ the Karplus constants are $A = 6.4$ Hz, $B = -1.4$ Hz, $C = 1.9$ Hz, whereas $\theta = \phi - 60°$ [147]. Fig. 4.5 (b) shows ${}^3J_{H^N H^{\alpha}}$ as a function of ϕ and these parameters. For $\phi \approx -120°$ or 60° strong coupling between the amide proton and H^{α} appears, while the weakest coupling is found for $\phi \approx -25°$ or 145°.

From simulations, ${}^3J_{H^N H^{\alpha}}$ coupling constants for each amino acid are calculated as an average according to

$$ {}^3J_{H^N H^{\alpha}} = \sum_{\phi} {}^3J_{H^N H^{\alpha}}(\phi)\ P(\phi)\ \Delta\phi. \tag{4.3} $$

Here, ${}^3J_{H^N H^{\alpha}}(\phi)$ is calculated using the Karplus relationship (Eq. 4.2) with the parameters derived by Pardi *et al.* for a given dihedral angle ϕ. $P(\phi)$ corresponds to the probability to find a dihedral angle between $(\phi - \Delta\phi/2)$ and $(\phi + \Delta\phi/2)$ with $\Delta\phi = 5°$. The probability distributions of ϕ for each amino acid, except the N-terminal residue Y10 , were calculated using the GROMACS tool `g_angle` [87]. The distributions for

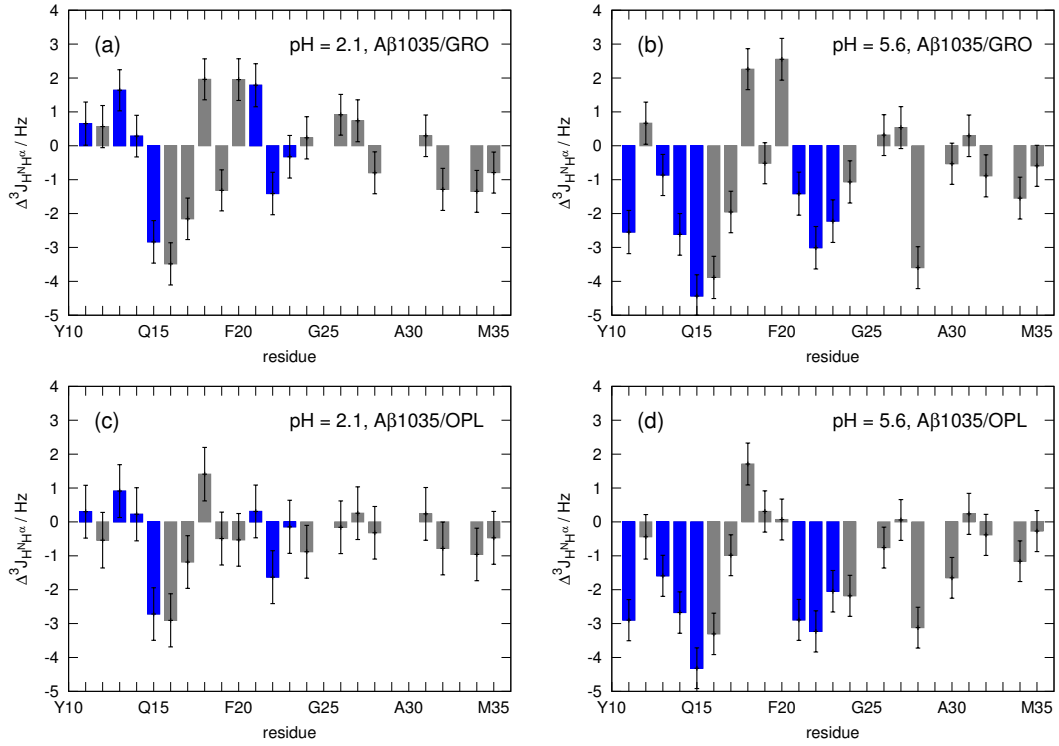

Figure 4.6: Difference between $^3J_{\mathrm{H^N H^\alpha}}$ coupling constants obtained from experiment and simulations ($\Delta^3 J_{\mathrm{H^N H^\alpha}}$). The plots show differences between Aβ1035/GRO and experiments at (a) pH 2.1, or (b) pH 5.6, and between Aβ1035/OPL and experiments at (c) pH 2.1, or (d) pH 5.6. For values marked in blue, experimental $^3J_{\mathrm{H^N H^\alpha}}$ coupling constants change by more than 1.5 Hz as the pH is changed.

both ensembles, Aβ1035/GRO and Aβ1035/OPL, are shown in Figs. B.1 and B.2 in appendix B.

Lee *et al.* obtained $^3J_{\mathrm{H^N H^\alpha}}$ coupling constants for Aβ(10-35)-NH_2 in aqueous environment at pH 2.1 and 5.6, both at 283 K [71]. The $^3J_{\mathrm{H^N H^\alpha}}$ coupling constants calculated from the simulations (set up at pH 5.6) were compared to the experimental data at both pH values. The comparison between simulations and experiments is shown Fig. 4.6. In particular, for each amino acid measured in the experiment

$$\Delta^3 J_{\mathrm{H^N H^\alpha}} = {}^3J^{\,\mathrm{exp}}_{H^N H^\alpha} - {}^3J^{\,\mathrm{sim}}_{H^N H^\alpha} \tag{4.4}$$

is plotted including error bars. For values marked in blue the experimental $^3J_{\mathrm{H^N H^\alpha}}$ coupling constants change by more than 1.5 Hz as the pH is changed. These residues are suggested to be involved in a pH dependent conformational transformation [71].

Fig. 4.6(a) and (b) show $\Delta^3 J_{\mathrm{H^N H^\alpha}}$ of all measured residues for Aβ1035/GRO at (a)

pH 2.1, and (b) pH 5.6. First of all, at both pH values the agreement with the experiment ($\Delta^3 J_{\mathrm{H^N H^\alpha}} = 0$) is weak corresponding to approximately 30 % of the data. However, in each case different residues are concerned. Additionally, although the simulation was setup to mimic pH 5.6, the difference between simulation and experiment is smaller if the data are compared to the experimental results at pH 2.1. In particular, at pH 2.1 the $^3J_{\mathrm{H^N H^\alpha}}$ coupling constants of residues E11, V12, H14, D23, V24, and I31 agree well with the experimental results. For three of these residues pH dependent $^3J_{\mathrm{H^N H^\alpha}}$ constants were observed. On the other hand, at pH 5.6 none of the coupling constants in agreement with the experiment shows a pH dependence. In summary, this suggests that the simulated ensemble might actually correspond to a pH closer to 2.1 than 5.6 as intended.

Comparing the results for Aβ1035/OPL to the experimental data this effect becomes more obvious, as shown in Fig. 4.6(c) for pH 2.1, and (d) for pH 5.6. At pH 5.6 32 % of the calculated coupling constants agree with the experimental values, while at pH 2.1 57 % agreement is reached including four pH sensitive $^3J_{\mathrm{H^N H^\alpha}}$ coupling constants. Independent of the pH the ensemble of Aβ1035/OPL shows better agreement with the experimental data than Aβ1035/GRO.

As stated above, the observations suggest, that the sampled ensembles might correspond to a pH lower than 5.6. The protonation state of the peptide used for the simulations was identified according to expected pK_a values within proteins given in the literature [135]. For histidine the pK_a within proteins is expected to be 6.5 – 7, for aspartic and glutamic acid 4.4 – 4.6. Therefore at pH 5.6, H13 and H14 were chosen to be protonated, and E11, E22, and D23 to be deprotonated. Possibly within the NMR-derived collapsed coil conformation determined at pH 5.6, the pK_a values of acidic and basic residues change upon their environment. The WHAT IF pK_a calculation software provided by the Nielsen group [148, 149, 150] was used to determine the protonation state of the first NMR-derived collapsed coil conformation. Indeed, preliminary results suggest different pK_a values for the two histidines, 6.2 for H13 and 8.4 for H14. Taking the trend and not the precise number serious, and combining with the results for $^3J_{\mathrm{H^N H^\alpha}}$ coupling constants, it is likely that at pH 5.6 H13 is protonated but H14 is deprotonated.

4.5 Conclusions

In this chapter the equilibrium conformations of Aβ(10-35)-NH_2 monomers in aqueous environment at pH 5.6 and 283 K similar to experimental conditions have been discussed. The performance of two force fields, GROMOS96 43a1 or OPLS/AA, has been tested. The results of the simulations were compared to the NMR-derived model conformations of Aβ(10-35)-NH_2 and primary NMR data as inter proton NOE distances and $^3J_{\mathrm{H^N H^\alpha}}$ scalar coupling constants [54, 71].

In summary, the two force fields yield different results. The main conformations of both systems differ significantly in structure and population as shown in Fig. 4.2 for Aβ1035/GRO and in Fig. 4.3 for Aβ1035/OPL. Additionally, the three most populated main conformations generated by the two force fields do not correspond well to the NMR-derived collapsed coil structure models. The RMSD based on the backbone atoms of residues K16 – G29 between the 1st NMR model and the configurations within the most populated clusters is larger than 0.4 ± 0.1 nm.

Corresponding to the population of clusters Aβ1035/GRO seems to be more ordered than Aβ1035/OPL. The average secondary structure content shown in Tab. 4.2 reveals that ordered secondary structure elements such as β-turns, β-sheets or β-bridges appear in the same amount within both ensembles. In contrast and corresponding to the different main conformations, significant differences were observed for the average secondary structure content of individual residues shown in Fig. 4.4. For the Aβ1035/GRO ensemble, the β-sheet and turn content is most pronounced for residues E22 – N27 forming the β-hairpin in the most populated conformation. For the Aβ1035/OPL ensemble, the probability to form β-sheets is more distributed along the sequence, while the highest turn content is measured for residues V18 – F20.

The comparison with NOE distances yielded reasonable agreement for both ensembles. For Aβ1035/GRO 53 % of the long-range NOE distances and 61 % of the medium-range NOE distances were consistent with the experimental values as shown in Tabs. 4.3 and 4.4. For Aβ1035/OPL agreement with the experiment is reached for 33 % and 63 % of the long-range and medium-range NOEs, respectively. In contrast, if only reliable NOE distances ≤ 5 Å are taken into account, all of the remaining long-range NOEs are violated by both ensembles. Concerning medium-range NOEs ≤ 5 Å, the Aβ1035/OPL ensemble shows only weak (33 %), but slightly better agreement with the experimental data than Aβ1035/GRO (20 %).

Calculated ${}^3J_{\mathrm{H^N H^\alpha}}$ scalar coupling constants were compared to experimental data measured at pH 2.1 and 5.6 as shown in Fig. 4.6. For Aβ1035/GRO approximately 30 % of the data were consistent with the experiments at both pH values, while in each case different residues were involved. Nevertheless, the deviation from the experimental data is much smaller at pH 2.1, especially for residues whose ${}^3J_{\mathrm{H^N H^\alpha}}$ coupling constants change upon pH by more than 1.5 Hz. This effect is more pronounced for Aβ1035/OPL. Here, 57 % and 32 % of the ${}^3J_{\mathrm{H^N H^\alpha}}$ coupling constants agree with the experimental values at pH 2.1 and 5.6, respectively. These results suggest that (i) independent of the pH the OPLS/AA force field yields better agreement with the experimental data, and (ii) the protonation state of the peptide in the simulations might correspond to a pH lower than 5.6.

Concerning the latter, the protonation state of the 1st NMR-derived collapsed coil conformation was determined using the WHAT IF pK_a calculation software [148, 149,

150]. Preliminary results suggest that the pK_a values of the two histidines deviate from expected values given in the literature [135]. Based on these findings it is likely that at pH 5.6 H13 is protonated and H14 is deprotonated, differing from the simulation setup. According to the obtained simulation results, a small change of the protonation state of the peptide might induce a significant conformational change.

Finally, a slightly different performance of the two force fields was expected. In contrast, in the present work either force field was found to sample different ensembles resulting in very distinct main conformations. It needs to be determined how large the overlap of both ensembles is in order to draw precise conclusions. Additionally, from the obtained results it is unclear which of the used force fields yields better results in terms of consistency with the experimental data and computational effort in order to obtain a certain level of consistency.

Chapter 5

Simulation Results for Aβ(10-35)-NH_2 Dimers

In this chapter simulations of Aβ(10-35)-NH_2 dimers in aqueous environment are discussed. Starting from the 1st NMR-derived structure model for Aβ(10-35)-NH_2 spontaneous dimer formation was modeled in explicit solvent in order to determine conformational structures of dimers at fibril growth conditions, neutral pH and 300 K. As in previous chapters, the first sections give background information on the stand of experimental and theoretical research on this subject, and explain details concerning the simulation setup. Sec. 5.3 to 5.5 discuss the conformational variety of the dimer system, the complex free energy landscape, and interactions stabilizing different types of dimers.

5.1 Previous experimental and theoretical observations

Several groups studied the morphology of Aβ(10-35)-NH_2 fibrils depending on the pH [72, 73, 74, 75, 76]. EM images showed that fibrils formed at pH 7.4 contained twisted pairs of single filaments with varying periodicities of the twist. The fibril diameters vary from 5.5 ± 1.0 nm at the narrowest point to 10.5 ± 1.0 nm at the widest point [72]. Solid-state NMR spectroscopy was used to measure intermolecular ^{13}C distances within fibrils built from peptides containing one ^{13}C labeled amino acid. These measurements suggested an in-register parallel alignment of the peptides, while the peptides are assumed to be fully extended [73, 74, 75, 76]. A more recent study suggests the peptides to be bent with some residues in region D23 – G29 in a non-β-strand conformation [72]. The stability of fibrillar aggregates containing this bent, so-called Tycko model of Aβ(10-35)-NH_2 was tested at 330 K by 1 ns short MD simulations [77]. Oligomers containing eight in-register, parallel aligned peptides in this conformation or two of these octamers in an interlocked conformation were stable within the short simulation time.

Due to the limits of experimental techniques the conformations of early aggregation

intermediates are still unknown. Therefore, different theoretical methods were used to elucidate possible conformations of Aβ(10-35)-NH_2 dimers, trimers and tetramers.

Tarus *et al.* studied the stability of possible dimer conformations in aqueous solution [78]. Using a shape complementary docking protocol and starting from the 1st NMR-derived collapsed coil model of monomers they generated two types of dimers. The ϕ-dimer is dominated by hydrophobic intermolecular contacts, and the ϵ-dimer is characterized by electrostatic interpeptide interactions. The stability of both dimers was tested with MD simulations at 300 K and pH 7. Only the ϕ-dimer was stable over 10 ns. Correspondingly, the formation of intermolecular contacts between the central hydrophobic cluster, and the repulsion of water at the interface were assumed to be the initial steps of dimerization. Additionally, a substantial structural reorganization within the C- and N-terminus was observed.

Jang and Shin studied the structural diversity of Aβ(10-35) oligomers up to tetramers in aqueous solution at neutral pH. To observe spontaneous aggregation, they applied REMD simulations using the all-atom AMBER96 force field for the peptides with an implicit solvent model [79, 80]. The 1st NMR-derived structure model of Aβ(10-35)-NH_2 monomers served as initial configuration of the peptides. Aggregates were characterized by a high β-sheet content of 40 to 50 % at 300 K. Within main conformations at least one Aβ(10-35) unit formed two β-strands joined by a turn region around residues G25 – G29. These bent, double β-strands assembled into several different interlocking patterns while peptides aligned in parallel as well as in antiparallel orientations. Partial α-helical conformations were also observed up to tetramers, and are believed to play a critical role in the aggregation process. For Aβ(10-35) dimers and trimers it was found that the average potential energies of different conformations were very similar, but somewhat lower for highly ordered β-strands. On the other hand, conformations with low potential energy were higher in solvation energy.

In the present work, the spontaneous dimerization of Aβ(10-35)-NH_2 was studied, similar to the approach used by Jang and Shin [79]. Here, the more accurate explicit solvent description was used in order to determine the peptide-solvent interaction in more detail. The results will be compared to the implicit solvent study by Jang *et al.* [79].

5.2 System setup and equilibration

The amino acid sequence of Aβ(10-35)-NH_2 can be taken from the sequence of the full length Aβ peptide shown in Fig. 1.6 in Sec. 1.2.1. Corresponding to fibril growth conditions reported in experiments [73, 74, 75, 76, 72], the protonation was chosen to mimic neutral pH: a positively charged N-terminus, three negative charges on E11, E22 and, D23, and both lysine residues, K16 and K28, positively charged. The C-terminus

is amidated. The 1st NMR-derived collapsed coil model of Aβ(10-35)-NH_2 monomers (PDB code: 1HZ3) served as initial configuration for both peptides.

To simulate spontaneous dimerization, both peptides in random mutual orientation separated by 1.5 nm were placed in an dodecahedral box. The dimensions of the box were chosen such that the minimum distance between the solute and the boundaries of the box was 0.75 nm for the initial configuration. The remaining space was filled by 7095 SPC water molecules [94, 95]. First, the system was energy minimized, followed by a 1 ns simulation at 293 K and 1 bar with position restraints on the peptide as described in Sec. 2.5 and 2.3.4, respectively. In addition, the system was simulated for 1 ns without restraints at the same temperature and pressure. The initial configurations for the REMD simulation were generated performing a high temperature simulation at 400 K for 150 ns. In order to allow the peptides to adopt different orientations to each other but prevent simultaneous unfolding, the C_α atoms of H13 and I32 were restraint to their initial positions (Sec. 2.3.4). Since the most uncorrelated and structurally different conformations should serve as initial configurations for the REMD simulation, they were chosen according to the following criteria (i) the RMSD of a configuration and the initial collapsed coil conformation should be at least 0.5 nm, and (ii) consecutive initial configurations should be at least 1 ns apart from each other.

The REMD simulation was performed using 68 replica of the system, which were simulated at constant volume and temperatures between 281 and 400 K for 380 ns each. Swapping of replica between neighboring temperatures was attempted every 6 ps. Snapshots of the system were saved every 20 ps.

Convergence of the simulation was tested for several reaction coordinates. Fig. 5.1 shows running averages for (a) the RMSD to the initial configuration of both peptides based on the backbone atoms of residues K16 – G29, and (b) R_g of the dimer at 300 K. Values were averaged over 5000 ps windows. The data indicate that the simulation converges within 150 ns. Therefore, data of the final 230 ns were used to determine equilibrium properties at 300 K.

5.3 Analysis of conformational clusters

The main conformations of Aβ(10-35)-NH_2 dimers were determined using a cluster algorithm (Sec. 2.6.4) based on the RMSD of the backbone atoms of residues K16 – G29 and a RMSD cutoff of 0.2 nm. This analysis resulted in 217 clusters. The twelve most populated conformations together corresponding to 36 % of all configurations are shown in Fig. 5.2. Within the errors each of these conformations is adopted with a probability of approximately 3.0 to 3.5 %.

These main conformations, except #5 and #10, are characterized by the formation of β-sheets while parallel as well as antiparallel orientations appear. Within these con-

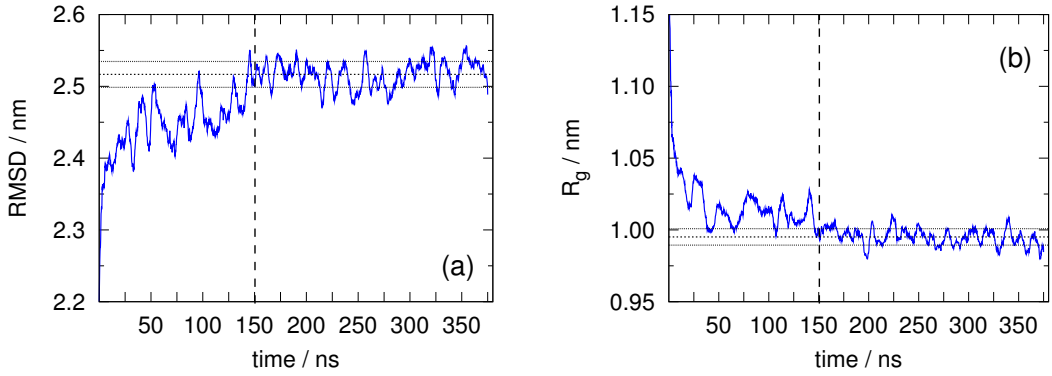

Figure 5.1: Convergence of (a) RMSD of backbone atoms of residues K16 – G29 to the initial configuration with both peptides in collapsed coil conformation, and (b) R_g of Aβ(10-35)-NH$_2$ dimer simulation at 300 K. Shown are running averages over 5000 ps windows. The vertical dashed lines mark the beginning of the sampling period, 150 ns. A horizontal dashed line indicates the average over the sampling period, and the dotted lines give the corresponding standard deviation.

formations there seems to be no predominant β-sheet arrangement. Nevertheless, the β-strand conformation is often adopted by similar residues: approximately E11 – K16 (#1, #2, #11), H14 – F19 (#1, #2 – #6, #9 – #11), and K28 – L34 (#1 – #4, #11). The numbers in parenthesis give the conformations forming β-strands in the corresponding regions. Interestingly, the second region contains the proposed self-recognition site of Aβ involving residues K16 to F20 [66]. Additionally, the formation of short helices is found in four conformations. A 3-helix formed by residues E22 – V24 appears in conformation #1, and α-helices formed by residues V12 – L17 in conformations #2 and #5, or residues V24 – G29 in conformation #12. Partially helical or unstructured conformations are assumed to be transient structures during the aggregation process [79].

Secondary structure content

In agreement with the main conformations shown in Fig. 5.2 the analysis of the secondary structure content reveals that the ensemble of Aβ(10-35)-NH$_2$ dimers at 300 K is only partly structured. About 41 ± 1 % of the residues within individual peptides are unstructured, while 23 ± 1 % are bent, 8 ± 1 % form a turn, 7 ± 1 % a β-bridge, and 2 ± 1 % an α-helix. The average β-sheet content is about 20 %, while 14 ± 1 % correspond to intramolecular and 6 ± 1 % to intermolecular β-sheets, respectively. The rare appearance of intermolecular β-sheets suggests that dimers are not stabilized by a strong intermolecular hydrogen bond pattern. This was stated before by Tarus *et al.* whose generated

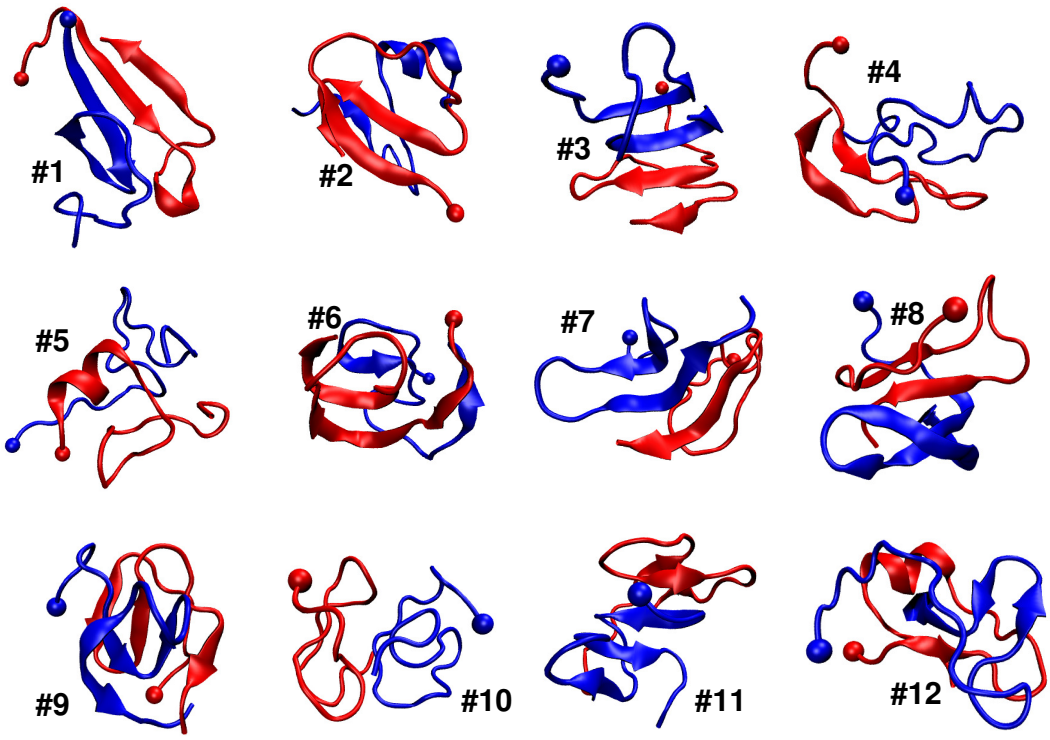

Figure 5.2: Central configurations of the twelve largest out of 217 clusters together containing 36 % of all configurations of the ensemble of Aβ(10-35)-NH_2 dimers at 300 K. Population of clusters given in parenthesis: #1, #2 (4.1 ± 0.5 %), #3, #4 (3.3 ± 0.6 %), #5 (3.1 ± 0.4 %), #6 (3.0 ± 0.4 %), and #7–#12 (< 3 %). The peptide backbone is shown in ribbon representation; the C_α atom of Y10 of each peptide is depicted as a sphere.

ϵ-dimer based on electrostatic interpeptide interactions was unstable [78]. Other possible stabilizing interpeptide interactions will be discussed in Sec. 5.5.

In order to distinguish if individual residues rather form intra- or intermolecular β-sheets the secondary structure content was determined for each residue and is shown in Fig. 5.3. Intramolecular β-sheets are preferred to be formed by residues H14 – A21, and N27 – L34, with probabilities > 10 %. The region in between, approximately E22 – S26, is bent or forms a turn. Approximately the same residues form a turn in the initial collapsed coil conformation (V24 – N27) or they are assumed to be bent in individual peptides within mature fibrils (D23 – G29) [72]. Intramolecular β-sheets corresponding to the favored regions appear in both peptides in conformations #3 and #11, or in one peptide in conformations #1, #2, #4, #5, and #7 – #9 shown in Fig. 5.2. Since five to seven residues form a bend or turn in between the β-strands, an antiparallel as well as a parallel orientation of the β-strands is possible. The highest probabilities to form intermolecular β-sheets (> 10 %) are found for residues H13 – H14, and the hydrophobic residues I31 – L34 at the C-terminus, see Fig. 5.3. Short intermolecular β-sheets involving these residues are found in conformations #2, #6, #7, #9, and #11 shown in Fig. 5.2. The α-helix content does not exceed 10 %, but is significant for residues V12 – L17 and V24 – N27 corresponding to the helices formed in conformations #1, #2, #5, and #12.

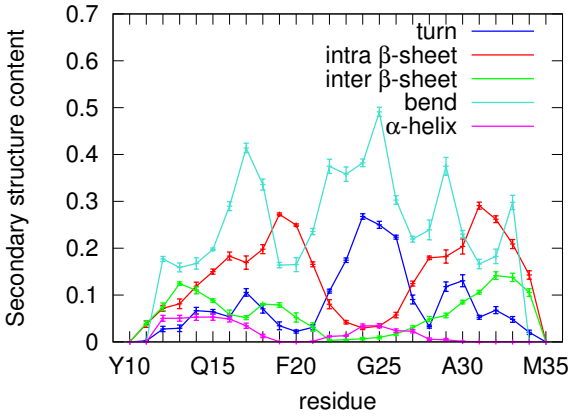

Figure 5.3: Secondary structure content of individual residues of Aβ(10-35)-NH_2 dimer at 300 K. Given are the turn, intra- and intermolecular β-sheet, bend, and α-helix content.

Comparison with implicit solvent simulation

In contrast to the present work, only nine highly populated main conformations were found in the implicit solvent simulation while the RMSD cutoff used for the cluster

analysis is not given [79]. The peptides within these dimers often form β-hairpin-like structures. Although Jang *et al.* simulated at a lower concentration, their main conformations seem to be more ordered in terms of β-sheet formation. This agrees with the secondary structure analysis. While they observe 40 to 45 % β-sheet content in the present work only 20 % are seen. Similar to the previous study partly α-helical structures were observed. From the data given by Jang *et al.* it is unclear if helices are formed by the same residues. In general, conformations #1 – #12 are more bent and compact as the ones found by the implicit solvent study. The latter is evident from a difference in the average radius of gyration of the dimers. They observe an R_g of approximately 2.5 to 3.0 nm, the ensemble sampled in the present work corresponds to an R_g of 0.99 ± 0.01 nm (Fig. 5.1 (b)). Jang *et al.* simulated the dimer in a spherical box with a radius of 4.5 nm. In the present work a dodecahedral box was used. Approximating the box shape with a sphere, the radius would correspond to 3.8 nm which would still be enough to accommodate dimers with $R_g = 2.5 - 3.0$ nm. A small effect of the box dimensions on the compactness of the dimer cannot be excluded, but it is unlikely that the decrease of the effective box radius by 0.7 nm could fully account for the decrease in R_g by $1.5 - 2.0$ nm.

5.4 Free energy landscape

For the Aβ(10-35)-NH_2 dimer system a variety of poorly populated conformations was found as a result of the RMSD based cluster analysis, see Fig. 5.2. In order to determine if these various conformations can be grouped due to prominent internal motions within the molecules, a PCA was applied and the first two PCs were used to calculate a free energy landscape. For details concerning PCA see Sec. 2.6.7. The analysis of the cosine content of the first two PCs resulted in < 0.0016, suggesting that both PCs do not correspond to random diffusion [116, 117]. The free energy landscape along the first and second principal components (PC_1, PC_2) is shown in Fig. 5.4, together with the locations of the twelve most populated conformations of Fig. 5.2.

Compared to the broad free energy landscape of the Aβ(25-35) trimer system shown in Fig. 3.12, the free energy landscape of Aβ(10-35)-NH_2 dimers is rather narrow. This might suggest that this system is somehow confined. Besides two broad minima rather canyon-like regions of low free energy appear. The minimum of lowest free energy, approximately -8 kJ/mol, is located at the center of the free energy landscape and contains conformations #1, #4, and #11. The second broad minimum of the same free energy is located at the east edge of $\Delta F(PC_1, PC_2)$, and contains the partly α-helical or unstructured conformations #2, #5, #10, and #12. The remaining main conformations #3, and #6 to #9 appear in local free energy minima of approximately -5 to -7 kJ/mol located in the north or south corners of $\Delta F(PC_1, PC_2)$.

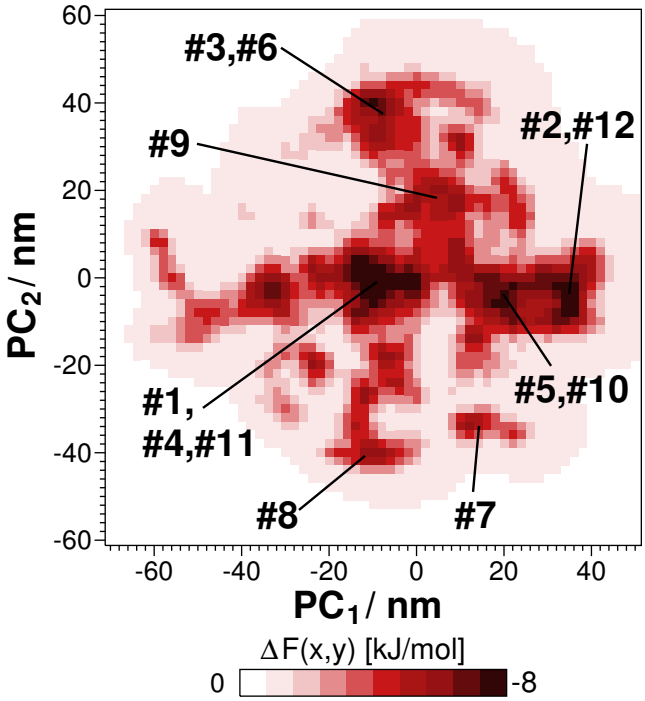

Figure 5.4: Free energy landscape along the first and second principle component (PC_1, PC_2) and the location of the twelve predominant conformations shown in Fig. 5.2.

Subdivision of the free energy landscape

In order to understand the complexity of the free energy landscape, six regions of low free energy, with $\Delta F(PC_1, PC_2) < -2$ kJ/mol, were defined as illustrated in Fig. 5.5. Each minimum was analyzed in terms of secondary structure and intermolecular side chain contacts. For each minimum the data were averaged over all configurations within the corresponding minimum.

The average secondary structure content of all minima is given in Tab. 5.1. Similar for all six minima approximately 41 % and 23 % of the residues of individual peptides are unstructured or bent, respectively. Significant differences are found for secondary structure motifs as turns, intra- and intermolecular β-sheets, and α-helices. Fig. 5.6 shows the distribution of these secondary structure elements within the free energy landscape. The color coding corresponds to 0 % (yellow) up to approximately 23 % (dark red) secondary structure content.

The most prominent secondary structure element within Aβ(10-35)-NH_2 dimers is the formation of intramolecular β-sheets, as shown by Fig. 5.6 (a). The ensemble is mostly characterized by an intramolecular β-sheet content of approximately 16 %, which

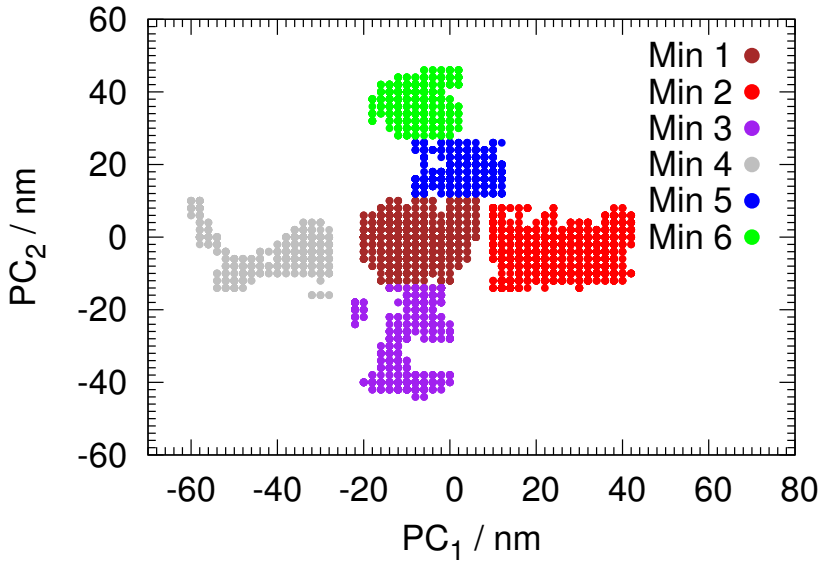

Figure 5.5: Free energy landscape along PC_1 and PC_2. Color coding corresponds to the six different regions of low free energy as shown in Fig. 5.4 which are here denoted as minima 1 to 6.

corresponds to four residues per peptide. In contrast, the dimers in minimum 2, located at the east end of $\Delta F(PC_1, PC_2)$, form intramolecular β-sheets involving less than four residues. Additionally, dimers in minimum 6, located at the north end of $\Delta F(PC_1, PC_2)$, have the highest intramolecular β-sheet content of approximately 23 %. This corresponds to at least six residues per peptide.

The intermolecular β-sheet content increases from approximately 3 to 8 % along PC_2, see Fig. 5.6 (b). Interestingly, conformations within minimum 6 and also minimum 5 have the highest intermolecular β-sheet content. Comparing Fig. 5.6 (a) and (b), it seems that the increased formation of intra- and intermolecular β-sheets is somehow correlated, which seems incomprehensible at first. However, as shown in Tab. 5.1 only approximately 30 % of the residues are involved in β-sheet formation. Additionally, much less inter- than intramolecular β-sheets are formed.

Partly α-helical conformations are only found in minima 2 and 4 located at the east and west corners of $\Delta F(PC_1, PC_2)$, as shown by Fig. 5.6 (c). Finally, the distribution of the average turn content within $\Delta F(PC_1, PC_2)$ is shown in Fig. 5.6 (d). Most prominent is a turn content of approximately 8 %. Partly α-helical conformations in minimum 2 and conformations forming rather large intra- and intermolecular β-sheets in minimum 6 are characterized by a lower turn content.

	Min 1	Min 2	Min 3	Min 4	Min 5	Min 6
coil	39	41	44	42	41	40
bend	24	21	24	24	23	21
turn	8	**11**	6	**4**	7	**4**
intra β-sheet	14	**10**	14	16	16	**23**
inter β-sheet	5	4	3	4	**8**	**7**
α-helix	1	**4**	0	**4**	0	0

Table 5.1: Average secondary structure content of Aβ(10-35)-NH_2 dimers at 300 K. Averaged over configurations within the six minima of low free energy defined in Fig. 5.5. All values are given in % with standard errors of 1 %.

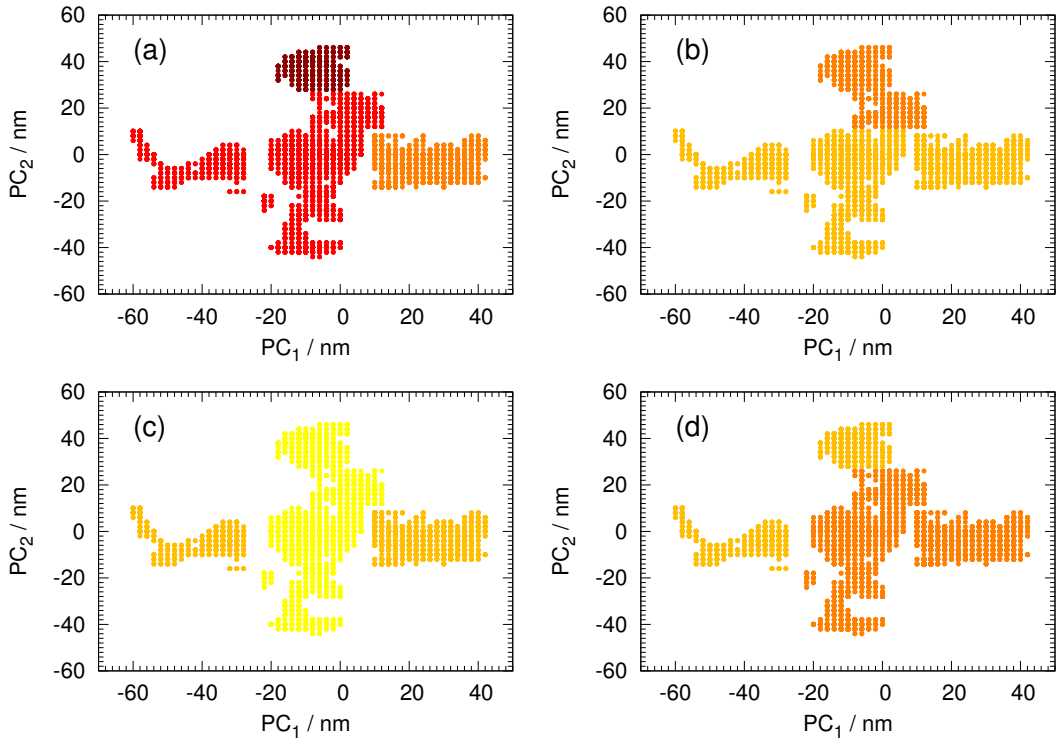

Figure 5.6: Free energy landscape along PC_1 and PC_2. Population of secondary structure within the six different minima of low free energy. Shown are (a) intramolecular β-sheet, (b) intermolecular β-sheet, (c) α-helix, and (d) turn content. The secondary structure content increases from 0 (yellow) to approximately 23 % (dark red). Compare also with Tab. 5.1.

Intermolecular side chain contacts between individual residues were determined for each minimum. Side chain contact maps for minima 1 to 6 were calculated as described in Sec. 2.6.6, and are shown in appendix C. Most of the contacts appear in less than 60 % of all configurations within a certain minimum. Therefore, no significant contact pattern could be assigned to any free energy minimum. Nevertheless, prominent contacts with probabilities between 40 and 60 % are often formed between the CHC of both peptides, the CHC and the N-terminus (in particular H13, H14), and the CHC and the hydrophobic C-terminus. Although these interactions are not very significant, they might contribute to the stabilization of the different dimer conformations.

5.5 Interactions stabilizing different dimer conformations

Based on the detailed analysis of the free energy landscape and the degree of β-sheet formation, the Aβ(10-35)-NH_2 dimer system could be characterized by three dimer states: fibril-like (D_{fib}), ordered (D_{ord}), and disordered (D_{dis}).

Within Aβ(10-35)-NH_2 fibrils individual peptides form parallel intermolecular β-sheets, either over the whole peptide length or except residues D23 – G29 [73, 74, 75, 76, 72]. Correspondingly, fibril-like dimers are characterized by large intermolecular β-sheets. The secondary structure analysis discussed in the previous section suggests that such fibril-like dimers might also contain large intramolecular β-sheets. Although the intermolecular β-sheet content was found to be rather low, D_{fib} are here defined to contain an intermolecular β-sheet formed by at least five consecutive residues.

Ordered dimers are characterized by forming large intramolecular β-sheets and possibly short intermolecular β-sheets. Large corresponds here to at least six consecutive residues in agreement with the highest intramolecular β-sheet content determined for minimum 6, listed in Tab. 5.1. Short intermolecular β-sheets are such that involve less than five residues. Here, the ordered dimers represent a pre-ordered state compared to fibril-like dimers without forming large intermolecular β-sheets. The remaining configurations of the ensemble are denoted as disordered dimers. These three states are in equilibrium

$$D_{dis} \rightleftarrows D_{ord} \rightleftarrows D_{fib} \rightleftarrows D_{dis}. \tag{5.1}$$

The free energy of transitions between those states can be calculated using Eq. 2.29 based on the population of each dimer state. In order to determine possible driving forces of the transitions, the energetic and entropic contributions to ΔF were also obtained using Eqs. 2.30 and 2.31.

Here, only the transitions $D_{dis} \rightleftarrows D_{ord}$ and $D_{ord} \rightleftarrows D_{fib}$ are considered, and their energies are given in Tab. 5.2. Both transitions are unfavorable according to small positive ΔF values, while ΔF for D_{fib} is greater. For both transitions the energetic

	ΔF	ΔE_{pot}	$-T\Delta S$	$-T\Delta S_{\mathrm{conf}}$
$D_{\mathrm{dis}} \leftrightarrows D_{\mathrm{ord}}$	4.2(0.3)	-2(10)*	6(10)*	3(1)
$D_{\mathrm{ord}} \leftrightarrows D_{\mathrm{fib}}$	6.1(0.7)	30(30)*	-20(30)*	2(1)

Table 5.2: Thermodynamics of the transitions between D_{dis}, D_{ord}, and D_{fib}. Listed are the change in free energy ΔF with its energetic (ΔE_{pot}) and entropic ($-T\Delta S$) contributions. Additionally, the contribution due to the change in configurational entropy ($-T\Delta S_{\mathrm{conf}}$) is shown. Energies are given in kJ/mol with standard errors in parentheses. Values marked with stars are zero within error.

	$D_{\mathrm{dis}} \leftrightarrows D_{\mathrm{ord}}$			$D_{\mathrm{ord}} \leftrightarrows D_{\mathrm{fib}}$		
	ΔE_{cov}	ΔE_{coul}	ΔE_{LJ}	ΔE_{cov}	ΔE_{coul}	ΔE_{LJ}
PP	-4(1)	78(6)	5(2)	5(4)	60(20)	23(7)
PS	–	-180(10)	7(2)	–	-100(40)	-15(6)
SS	–	70(20)	20(10)	–	-100(60)	-40(40)*

Table 5.3: Covalent, electrostatic and Lennard-Jones contributions to the potential energy of the transitions between D_{dis}, D_{ord}, and D_{fib} for certain interaction partners: peptide-peptide (PP), peptide-solvent (PS), and solvent-solvent (SS). Energies are given in kJ/mol with standard errors in parentheses. Values marked with stars are zero within error.

(ΔE_{pot}) and the resulting entropic contributions ($-T\Delta S$) are zero within errors. Based on these data, the main driving forces of the transitions could not be assigned.

Analysis of energetic contributions

Usually, in atomistic MD simulations large errors in the potential energy arise from averaging over all solvent molecules. To avoid this problem, the change in potential energy was separated into its contributions corresponding to peptide-peptide, peptide-solvent and solvent-solvent interactions. These contributions were further separated into parts arising from covalent, Coulomb, and van der Waals interactions, and are shown in Tab. 5.3. Although ΔE_{pot} is zero within errors, the individual energy contributions are rather large and significantly different from zero.

The transition from disordered to ordered dimers is mainly characterized by unfavorable peptide-peptide and solvent-solvent interactions. Most prominent is ΔE_{coul}(PP) with 78 ± 6 kJ/mol. Possibly, in D_{ord} the interaction between atoms of opposite charge is weaker due to a larger separation of charges. The increase of the solvent-solvent interaction energy might arise from an unfavorable hydrogen bonding network and packing of the water molecules around D_{ord}. Interestingly, the electrostatic interaction between

D_{ord} and the solvent is drastically decreased, which will be discussed in more detail later.

The transition from ordered to fibril-like dimers shows similar contributions to the total potential energy as the transition from disordered to ordered dimers. Peptide-peptide interaction energies increase, while electrostatic interactions are most prominent followed by van der Waals interactions. Peptide-solvent and solvent-solvent interaction energies decrease by approximately 100 ± 60 kJ/mol, and are dominated by electrostatic contributions.

The peptide is a complex molecule containing charges, hydrophilic (dipolar) and hydrophobic groups interacting with water. Nevertheless, the qualitative behavior of the electrostatic contributions may be explained from the separation of two single opposite charges in an aqueous environment. This simplified model is illustrated by the sketch in Fig 5.7. Assume two single opposite charges in close contact in an aqueous environment. The arising electric field will induce ordering of water molecules in the near environment, while a number of water molecules will form a (close) solvation shell around the charges. If the two single charges are separated the electrostatic interaction between both increases. For the Aβ(10-35)-NH_2 system this corresponds to $D_{dis} \rightarrow D_{ord} \rightarrow D_{fib}$ with $\Delta E_{coul}(PP) > 0$ see Tab. 5.3. In turn, in the model system more water molecules (i) are in close contact with the charges forming a solvation shell, and (ii) are influenced by the electric field between the charges and reorient along the field gradient. The first yields a favorable electrostatic interaction energy between charges and water molecules, and the second contributes to a favorable electrostatic interaction energy between ordered water molecules. For the Aβ(10-35)-NH_2 peptide-water system these two terms correspond to $\Delta E_{coul}(PS) < 0$ and $\Delta E_{coul}(SS) < 0$, respectively. The latter is only observed for the transition from D_{ord} to D_{fib}.

For the simple case of single opposite charges in water, it is known that the ordering of water molecules upon charge separation results in a significant decrease of the solvent entropy. In fact, this is the origin of the attraction between the charges [118].

Analysis of entropic contributions

The generated trajectories did not allow to evaluate the solvent entropy. However, the configurational entropy of each dimer state was determined using Eq. 2.34. For each sub-ensemble a cluster analysis was performed using the same criterion as for the full ensemble (Sec. 5.3). For both transitions, the change in free energy due to configurational entropy was then obtained using Eq. 2.35, and is listed in Tab. 5.2. Both transitions cost approximately the same amount of configurational entropy. For the transition from disordered to ordered dimers, $-T\Delta S_{conf} \approx \Delta F$, while for the transition from ordered to fibril-like dimers $-T\Delta S_{conf}$ corresponds only to one third of ΔF. Since, the total energetic and entropic contributions are zero within the errors (see Tab. 5.2) the overall influence of the configurational entropy remains unclear. However, in comparison to

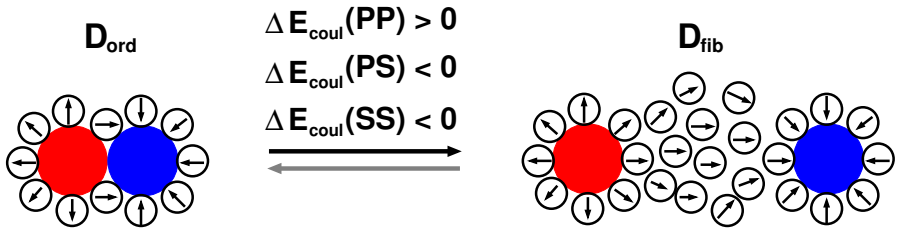

Figure 5.7: Separation of two single opposite charges (red and blue) in aqueous environment serving as a simplified model to describe the qualitative behavior of the electrostatic contributions obtained upon transitions between D_{dis}, D_{ord}, and D_{fib} Aβ(10-35)-NH_2 peptides listed in Tab. 5.3. Given are electrostatic contributions (ΔE_{coul}) of peptide-peptide (PP), peptide-solvent (PS), and solvent-solvent (SS) interactions. Water molecules are illustrated as spherical dipoles.

the individual energy contributions (Tab. 5.3) the contribution of $-T\Delta S_{conf}$ to ΔF is assumed to be small.

For each dimer state, the hydrophobic and hydrophilic solvent accessible surface area as well as the free energy of solvation were calculated as described in Sec. 2.6.5. Tab. 5.4 shows how these parameters change upon transitions between disordered, ordered and fibril-like dimers. In general, the hydrophobic SASA decreases or remains unchanged within the errors, whereas the hydrophilic SASA increases. However, each contribution is smaller than 1 nm^2. Correspondingly, ΔF_{solv} is very small but negative for the transition from disordered to ordered dimers, and zero within errors for the transition from ordered to fibril-like dimers. The free energy of solvation is based on peptide-solvent and solvent-solvent interactions. Since, $\Delta F_{solv} \approx 0$ it can be assumed that

$$\Delta E_{pot}(PS) + \Delta E_{pot}(SS) \approx T\Delta S_{solvent}. \tag{5.2}$$

In other words, the great decrease of peptide-solvent and solvent-solvent interaction energies dominated by electrostatic interactions, is almost compensated by a decrease in solvent entropy $\Delta S_{solvent} < 0$. As mentioned above, the interplay between electrostatic interactions resulting in a decrease of solvent entropy can be qualitatively compared to the effect of separating two singles charges in water [118].

5.6 Conclusions

For the Aβ(10-35)-NH_2 dimer system at 300 K, the RMSD-based cluster analysis yielded 217 poorly populated clusters with partially structured conformations. The twelve most populated main conformations arrange in rather complex alignments or interlocking

transition	hydrophobic ΔSASA [nm^2]	hydrophilic ΔSASA [nm^2]	total ΔF_{solv} [kJ/mol]
$D_{\mathrm{dis}} \leftrightarrows D_{\mathrm{ord}}$	-0.14(0.03)	0.55(0.03)	-1.4(0.2)
$D_{\mathrm{ord}} \leftrightarrows D_{\mathrm{fib}}$	0.1(0.1)*	0.7(0.08)	0.2(0.9)*

Table 5.4: Change in hydrophobic and hydrophilic SASA (ΔSASA) and the total free energy of solvation (ΔF_{solv}) for the transitions between D_{dis}, D_{ord}, and D_{fib}. Values are given with standard errors in parentheses. Values marked with stars are zero within error.

patterns, and are shown in Fig. 5.2. Dimer conformations are characterized by intramolecular β-sheets often formed between N-and C-terminal residues involving the CHC. Intermolecular β-sheets are rarely formed but preferentially involve residues H13 and H14, and the hydrophobic C-terminus, see Fig. 5.3. Parallel as well as antiparallel intra- and intermolecular β-sheets are observed.

Interestingly, the average intermolecular β-sheet content is only 6 ± 1 % and lower than the intramolecular β-sheet content of 14 ± 1 %. The rare appearance of intermolecular β-sheets suggests that dimers are rather stabilized by side chain interactions in agreement with a previous study [78]. The latter is partly supported by the calculated side chain contact maps which show rather no specific contacts between hydrophobic regions (L17 – A21, G29 – M35) and the hydrophilic N-terminus, see appendix C.

The free energy landscape of the system along the first and second principal components is shown in Fig. 5.4. Besides two broad minima, the free energy landscape is characterized by several canyon-like minima suggesting that the internal motion within the dimers is somehow confined. Based on a detailed dissection of the free energy landscape three dimer states were defined. Fibril-like dimers, containing large intermolecular β-sheets, prefibrillar dimers with large intramolecular β-sheets, and disordered dimers. Similar to Aβ(25-35), the disordered dimers correspond to the very first aggregates which either aggregate with monomers or transform to fibril-like dimers.

The transition towards β-sheet rich Aβ(10-35)-NH_2 dimers is unfavorable due to an increase of free energy by approximately 10 kJ/mol, see Tab. 5.2. The determination of individual potential energy contributions shows that peptide-peptide interaction energies increase from disordered to fibril-like dimers (Tab. 5.3). In contrast, peptide-solvent interactions, especially electrostatic contributions, become more favorable. The same is true for the solvent-solvent interactions concerning the transition from prefibrillar to fibril-like dimers. Additionally, the transition towards fibril-like dimers correlates with a small change in hydrophilic and hydrophobic solvent accessible surface area which results in small free energies of solvation, see Tab. 5.4. From this is was concluded that the decrease in peptide-solvent and solvent-solvent interaction energies, especially due

to electrostatic interactions, is nearly compensated by the a decrease in solvent entropy, see Eq. 5.2.

Finally, the formation of early aggregation intermediates is believed to be mainly driven by the hydrophobic effect in the first step. Our simulations of Aβ(10-35)-NH_2 dimers showed, that in the second step, transitions from disordered to fibril-like, β-sheet rich oligomers, probably of similar free energies, might be dictated by peptide-solvent and solvent-solvent interactions.

Chapter 6

Summary

The present PhD thesis focused on the initial stages of amyloid fibril formation for two fragments of the Amyloid β (Aβ) peptide which is associated with Alzheimer's disease. In particular, the preaggregated, monomeric state and early aggregation intermediates such as dimers and trimers of Aβ(25-35) and Aβ(10-35)-NH_2 were studied in aqueous environment performing extensive, fully atomistic REMD simulations.

Simulations of the Aβ(25-35) monomer were discussed in Chap. 3. The peptide was studied at neutral pH and 293 K similar to a previous simulation study. The latter work proposed that the peptide adopts a β-hairpin conformation in equilibrium with coiled conformations in water [62]. These results were verified by indirect comparison to experimental data. In the present work, simulations were started from a different, fully extended configuration. Similar to the previous study, β-hairpin conformations characterized by a β-turn formed by residues G29 and A30, and a β-sheet between residues N27 – K28 and I31 – I32 were the most populated conformations while also coiled conformations were observed, see Fig. 3.2. The β-hairpin conformations served as initial configurations to model spontaneous aggregation of Aβ(25-35).

Simulations of oligomeric structures were analyzed for Aβ(25-35) dimers and trimers at neutral pH and 293 K. As expected, a cluster analysis of both ensembles based on the RMSD yielded many poorly populated conformations, as shown in Figs. 3.4 and 3.11.

In case of Aβ(25-35) dimers the radius of gyration as a measure of the extension of the peptides was used to distinguish between compact, disordered and extended, fibril-like dimers which were observed at a ratio of 3:1, see Fig 3.5. In fibril-like dimers peptides are fully extended and form in- or out-of-register antiparallel β-sheets. The ensemble of Aβ(25-35) trimers is more complex, but approximately 38 % of the configurations were identified as ordered aggregates forming large intermolecular β-sheets. Among them, most prominent are aggregates containing extended, antiparallel β-sheets similar

to fibril-like dimers while a small amount of aggregates contained V-shaped peptides forming parallel β-sheets, see Fig. 3.11. V-shaped aggregates were also observed in a recently published study [124]. Interestingly, the dimensions of both aggregates, extended and V-shaped, correspond well to the diameters of Aβ(25-35) fibrils with two distinct morphologies, 3.58 ± 1.53 nm and 1.41 ± 0.48 nm [65].

If the predominant β-hairpin conformations of monomers are most likely to aggregate, the compact, disordered dimers can be assumed to be the very first aggregates formed. They will aggregate further or transform into fibril-like extended dimers. A thermodynamic analysis, reviewed in Sec. 3.4.3, indicated that the transition from compact, disordered to extended, fibril-like Aβ(25-35) dimers is unfavorable as the gain in potential energy in extended dimers is overcompensated by a loss in entropy. The lower energy of the extended dimers with peptides in antiparallel alignment arises from favorable intermolecular hydrogen bonding and stronger interactions between the charged termini at residues G25 and M35, and the charged residue K28, see Tab. 3.2 and Fig. 3.10. One fourth of the entropic cost paid upon formation of fibril-like dimers corresponds to configurational entropy, while the rest relates to solvent entropy. The decrease of solvent entropy is presumably caused by hydrophobic and electrostatic effects while the first correlates to a change in hydrophobic surface area of less than 1 nm^2.

Additionally, we found evidence that the transition towards fibril-like dimers is mediated by main chain hydrogen bonds between the former turn residues G29 and A30 and side chain interactions between the I31 residues of both peptides, as discussed in Sec. 3.4.2.

Structural and thermodynamic properties of the individual ensembles of Aβ(25-35) monomers, dimers and trimers at 293 K were compared in Sec. 3.6 in order to gain qualitative information about the aggregation process. Starting from the β-hairpin conformation observed for monomers, this structure motif is successively dissolved in dimer and trimer ensembles, see Figs. 3.3 and 3.14. The formation of fibril-like oligomers is characterized by the formation of intermolecular β-sheets. The average intermolecular β-sheet content is the same for dimers and trimers, and reaches approximately 21 %, see Tab. 3.3.

The net contribution to the aggregation free energy arising from configurational entropy and solvation free energy was dissected. As expected upon aggregation the configurational entropy decreases as the conformations of individual peptides within aggregates are strongly correlated whereas they are independent in the monomeric state, see Tab. 3.4. Additionally, the solvent accessible surface area, especially the hydrophobic area, decreases yielding a favorable solvation free energy, see Tab. 3.5. The decrease in solvation free energy is large enough to overcompensate the loss in configurational entropy. In summary, the hydrophobic effect, possibly combined with electrostatic effects,

yields an increase in solvent entropy which is believed to be one major driving force towards aggregation.

Chap. 4 discussed simulations of the Aβ(10-35)-NH_2 monomer conducted at pH 5.6. The results were compared to the NMR-derived collapsed coil conformation and primary NMR data collected at 283 K [54, 71]. Here, in order to minimize the bias from the initial configuration, the simulations were started from a fully extended configuration. The protonation of the peptide was chosen according to expected pK_a values of amino acids within proteins in order to mimic pH 5.6. In particular, the histidine residues H13 and H14 were chosen to be protonated as their pK_a values are expected to range from 6.5 to 7 [135]. In this project, the performance of two force fields, GROMOS96 43a1 and OPLS/AA, was tested.

None of the two sampled ensembles could reproduce the NMR-derived collapsed coil conformation while the two force fields yielded significantly different main conformations, compare Figs. 4.2 and 4.3. Nevertheless, reasonable agreement with NOE distances was found for both ensembles while the OPLS/AA force field shows slightly better agreement especially if only reliable NOE distances ≤ 5 Å were taken into account, see Tabs. 4.3 and 4.4. $^3J_{\mathrm{H^N H^\alpha}}$ scalar coupling constants calculated from the simulations were compared to experimental data measured at different pH values. The result supported the previous finding that the ensemble sampled with the OPLS/AA force field is more consistent with experimental observations. Additionally, both ensembles showed better agreement with the experimental $^3J_{\mathrm{H^N H^\alpha}}$ coupling constants observed at pH 2.1 than at pH 5.6, see Fig. 4.6. This suggests that the chosen protonation in the simulations corresponds to a pH lower than 5.6. Indeed, preliminary calculations of the pK_a values within the NMR-derived collapsed coil conformation using WHAT IF indicate that only one of the histidine residues, H13, might be protonated at pH 5.6. According to the obtained simulation results, a small change in the protonation state of the peptide might induce a significant conformational change.

Although a slightly different performance of the two force fields was expected, one major outcome of this project is that either force field samples different ensembles resulting in very distinct main conformations. In order to draw precise conclusions, it needs to be determined how large the overlap of both ensembles is. Additionally, it would be interesting to test which of the force fields yields better agreement with the experimental data if simulations are conducted using the protonation state suggested by WHAT IF.

Simulations of Aβ(10-35)-NH_2 dimers, outlined in Chap. 5, were performed at nearly physiological conditions, neutral pH and 300 K. Besides studies on mature fibrils at these conditions, there are no experimental data available. Therefore, it is unclear how good the used GROMOS96 43a1 force field represents the molecular structure of Aβ(10-35)-

NH_2 dimers. In comparison to a previous implicit solvent study [79], dimer conformations arrange in many different rather complex alignments or interlocking patterns which are poorly populated, see Fig. 5.2. Interestingly, the average intermolecular β-sheet content is only 6 ± 1 % and lower than the intramolecular β-sheet content of 14 ± 1 %. The rare appearance of intermolecular β-sheets suggests that dimers are rather stabilized by side chain interactions in agreement with a previous study [78]. The latter is partly supported by the calculated side chain contact maps which show rather nonspecific contacts between hydrophobic regions (L17 – A21, G29 – M35) and the hydrophilic N-terminus, see appendix C.

Based on the length of inter- and intramolecular β-sheets fibril-like, prefibrillar, and disordered dimers were determined at a ratio of 1:10:55. A thermodynamic analysis revealed that the transition towards β-sheet-rich, fibril-like dimers is mediated by favorable peptide-solvent and solvent-solvent interactions mainly arising from electrostatic interactions, see Tab. 5.3. Similar to the transition towards fibril-like Aβ(25-35) dimers, the formation of β-sheet-rich Aβ(10-35)-NH_2 dimers proceeds by a loss in configurational (Tab. 5.2) and solvent entropy. An exact quantitative determination of the latter was not possible. Nevertheless, the contribution of the solvent entropy is presumably much larger than the contribution of the configurational entropy. Similar to the Aβ(25-35) dimer system, the decrease in solvent entropy might arise from the hydrophobic effect corresponding to a small change of the hydrophobic SASA of less than 1 nm^2 (Tab. 5.4), and electrostatic effects.

Finally, in each of the ensembles of early aggregation intermediates modeled in the present study we found an equilibrium between rather disordered and fibril-like oligomers. In order to address the toxicity of these intermediate states it would be interesting to study how either disordered or fibril-like oligomers interact with membranes using MD simulations. Additionally, the nature of the prefibrillar, disordered oligomers is of particular interest and still comprises many questions. For example, why do certain antibodies distinguish between fibrillar and prefibrillar amyloid structures independent of the involved peptide? It would be interesting to search for common structure motifs in prefibrillar oligomers of different amyloidogenic peptides sampled by MD simulations. This may help to understand the detection process of these antibodies and in the future even to design new specific antibodies that could be used in clinical trials in order to detect, treat and possibly prevent Alzheimer's disease.

Appendix A

List of long- and medium-range NOE distances for Aβ(10-35)-NH_2 monomer

Table A.1: List of 30 long-range NOE distances calculated for Aβ(10-35) monomer at 283 K. Violations of the NOE distances are given for Aβ1035/GRO (GROMOS90 43a1 force field), Aβ1035/OPL (OPLS/AA force field), and a previous study by Baumketner *et al.* [134]. The NOE violations are given by (++) $\leq$ 0 Å, (+) 0 Å$< x \leq$ 1 Å, (-) 1 Å$< x \leq$ 2 Å, and (- -) $x >$ 2 Å. NOE distances with NMR upper bound separations $\leq$ 5 Å are printed bold [54].

Number	NOE distance	Aβ1035/GRO	Aβ1035/OPL	Ref. [134]
1	Y10:HD* – A21:HB*	++	-	++
2	Y10:HE* – A21:HB*	++	+	++
3	V18:H – V12:HG*	- -	- -	++
4	D23:H – V12:HG*	++	-	-
5	H14:HD2 – E22:HB*	++	+	++
6	H14:HD2 – E22:HG*	++	+	++
7	V18:H – M35:HE*	++	-	- -
8	D23:H – V18:HG*	-	++	+
9	E22:H – V18:HG*	-	+	+
10	S26:H – V18:HG*	- -	-	- -
11	**F19:HA – D23:H**	- -	- -	- -
12	**F19:HA – A30:H**	- -	+	-
13	F19:HD* – K28:HB*	++	- -	++
14	F19:HE* – K28:HB*	+	- -	++
15	F19:HZ – K28:HB*	- -	- -	+
16	F19:HD* – M35:HE*	++	++	-
17	F19:HE* – M35:HE*	++	++	++
18	F20:HD* – K28:HB*	++	++	++

Table A.1: (continued)

Number	NOE distance	Aβ1035/GRO	Aβ1035/OPL	Ref. [134]
19	F20:HE* – K28:HB*	++	++	++
20	F20:HZ – K28:HB*	++	++	++
21	F20:HD* – M35:HE*	++	++	++
22	F20:HE* – M35:HE*	++	++	++
23	G25:H – A21:HB*	-	-	+
24	S26:H – A21:HB*	-	-	-
25	S26:H – E22:HB*	++	+	++
26	S26:H – E22:HG*	++	++	+
27	S26:H – I32:HG*	- -	++	-
28	N27:H – I31:H	- -	-	- -
29	K28:H – M35:HE*	+	+	+
30	G29:H – M35:HE*	-	-	++

Table A.2: List of 56 medium-range NOE distances calculated for the Aβ(10-35) monomer at 283 K. Violations of the NOE distances are given for Aβ1035/GRO (GROMOS90 43a1 force field), and Aβ1035/OPL (OPLS/AA force field). The NOE violations are given by (++) ≤ 0 Å, (+) 0 Å$< x \leq 1$ Å, (-) 1 Å$< x \leq 2$ Å, and (- -) $x > 2$ Å. NOE distances with NMR upper bound separations ≤ 5 Å are printed bold [54].

Number	NOE distance	Aβ1035/GRO	Aβ1035/OPL
1	L17:HB* – F19:HE*	++	++
2	**L17:HG – F19:HD***	-	-
3	L17:HG – F19:HE*	++	++
4	**L17:HG – F19:HZ**	-	+
5	**L17:HG – F20:HZ**	- -	+
6	L17:HD* – F19:HZ	++	++
7	L17:HD* – F20:HE*	++	++
8	L17:HD* – F20:HZ	+	++
9	L17:HD* – F19:HE*	++	++
10	**V18:HA – F20:H**	+	++
11	V18:HA – F20:HZ	-	+
12	V18:HA – F20:HE*	+	++
13	V18:HA – F20:HD*	++	++
14	V18:HB – F20:HD*	++	++
15	V18:HB – F20:HZ	+	++
16	V18:HB – F20:HE*	++	++

Table A.2: (continued)

Number	NOE distance	Aβ1035/GRO	Aβ1035/OPL
17	V18:HG* – F20:HD*	++	++
18	V18:HG* – F20:HE*	++	++
19	V18:HG* – F20:HZ	-	++
20	**V18:HG* – F20:H**	-	+
21	F19:HD* – A21:HB*	++	+
22	F19:HE* – A21:HB*	++	+
23	F19:HZ – A21:HB*	++	++
24	F19:HA – E22:H	+	-
25	**E22:HA – V24:H**	- -	- -
26	E22:HB* – V24:H	++	+
27	**E22:HG* – V24:H**	++	++
28	V24:HG* – N27:H	-	-
29	**N27:H – A30:HB***	- -	- -
30	**N27:HA – G29:H**	+	++
31	**N27:HA – A30:H**	- -	+
32	**N27:HB* – G29:H**	-	+
33	N27:HD2* – G29:HA*	++	++
34	N27:HD2* – A30:HB*	++	++
35	A30:HA – I32:HA	-	+
36	**A30:HA – G33:H**	- -	+
37	**A30:HB* – G33:H**	- -	- -
38	G33:H – M35:HE*	++	+
39	I32:H – M35:HE*	++	+
40	G29:H – I31:HD*	++	++
41	S26:HB* – K28:H	++	++
42	**D23:HA – G25:H**	++	++
43	Y10:HD* – V12:H	++	++
44	Y10:HD* – V12:HB	++	++
45	Y10:HD* – V12:HG*	++	++
46	Y10:HE* – V12:H	++	++
47	Y10:HE* – V12:HB	++	++
48	Y10:HE* – V12:HG*	++	++
49	E11:HA – H13:HD2	+	+
50	E11:HB* – H13:HD2	++	++
51	E11:HG* – H13:HD2	++	++
52	V12:HG* – H14:HD2	++	++
53	**V12:HB – H14:HD2**	++	++

Table A.2: (continued)

Number	NOE distance	Aβ1035/GRO	Aβ1035/OPL
54	H14:HA – K16:H	++	++
55	H14:HD2 – K16:H	+	+
56	K16:H – V18:HG*	++	++

Appendix B

Dihedral angle ϕ distributions for Aβ(10-35) monomer

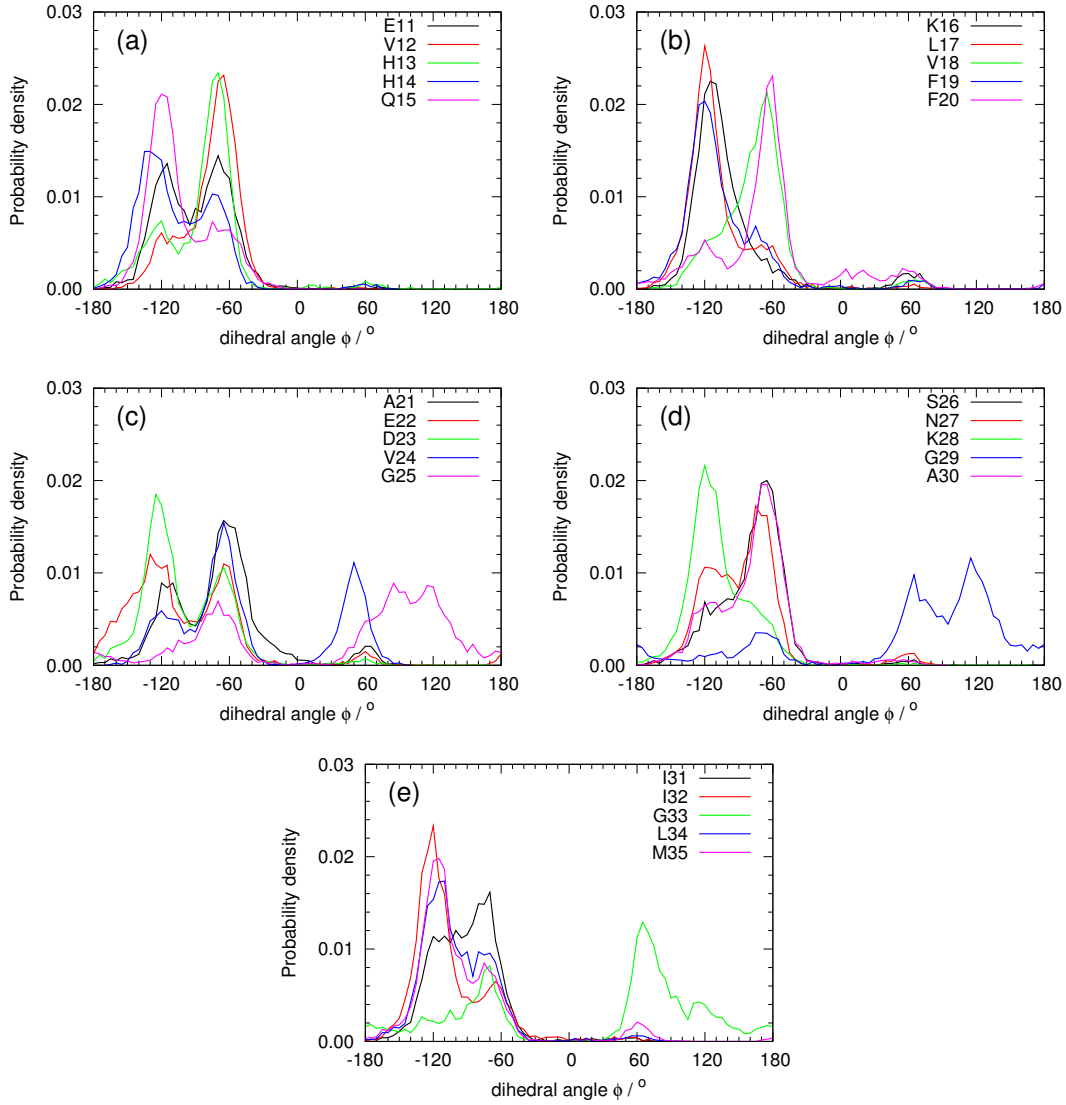

Figure B.1: Distribution of dihedral angle ϕ for residues (a) E11 to Q15, (b) K16 to F20, (c) A21 to G25, (d) S26 to A30, and (e) I31 to M35 within the Aβ(10-35) monomer in Aβ1035/GRO.

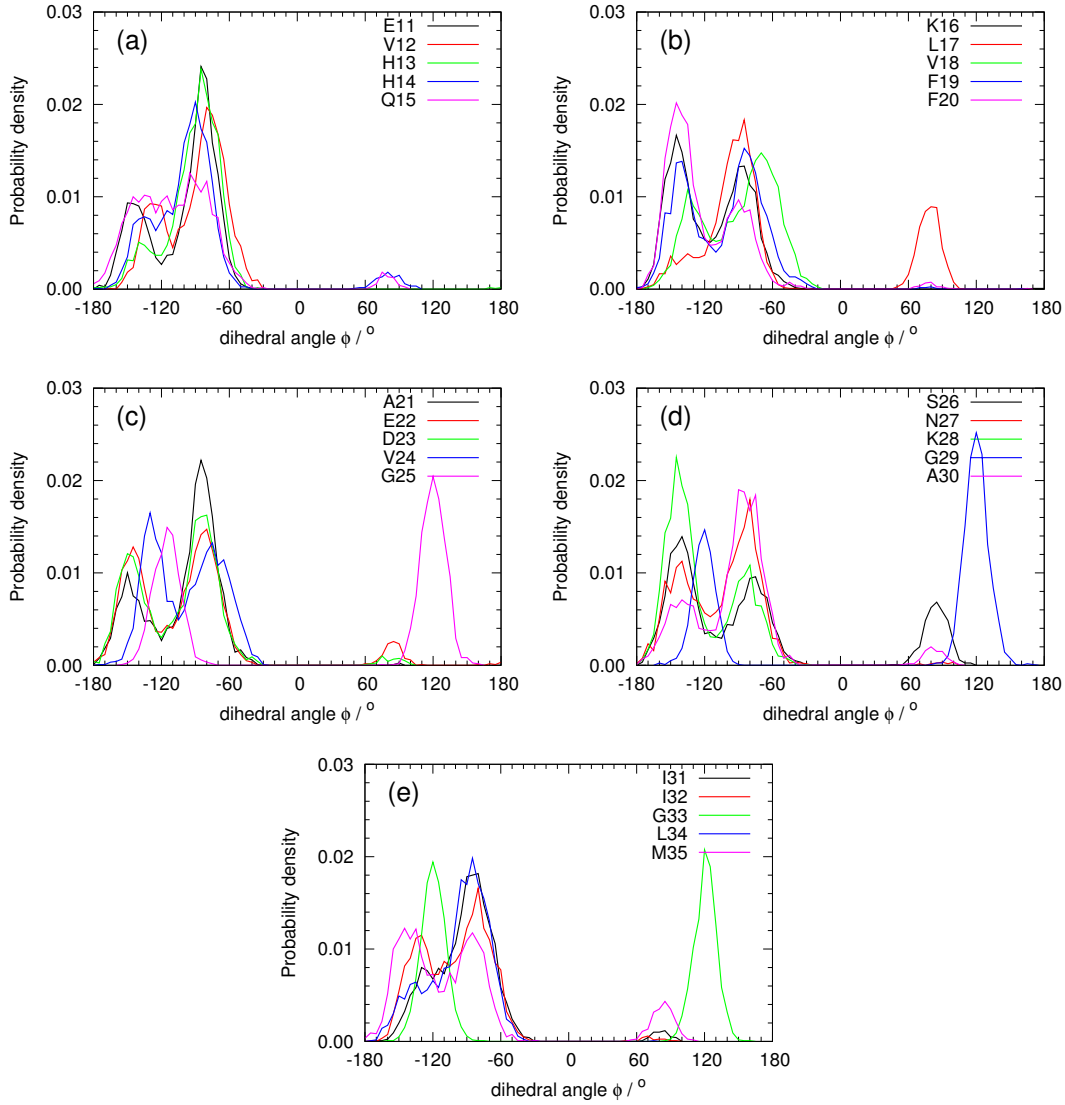

Figure B.2: Distribution of dihedral angle ϕ for residues (a) E11 to Q15, (b) K16 to F20, (c) A21 to G25, (d) S26 to A30, and (e) I31 to M35 within the Aβ(10-35) monomer in Aβ1035/OPL.

Appendix C

Intermolecular side chain contacts within Aβ(10-35)-NH_2 dimers

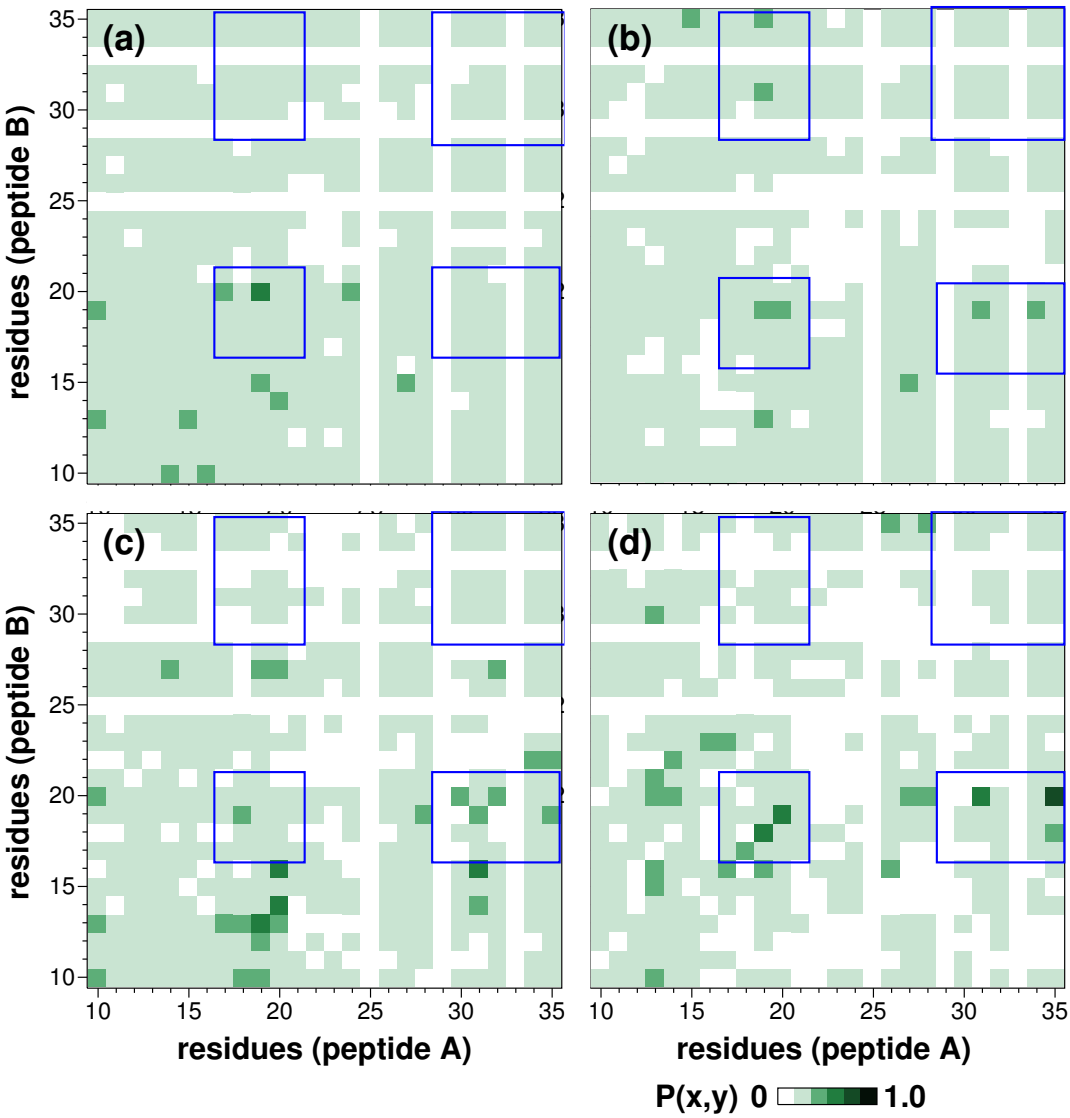

Figure C.1: Intermolecular side chain contacts within Aβ(10-35)-NH_2 dimers at 300 K. Shown are contact maps for minima 1 to 4 of low free energy defined in Fig. 5.5. Regions corresponding to interactions between the central hydrophobic cluster L17 – A21 and the hydrophobic C-terminus G29 – M35 are marked in blue.

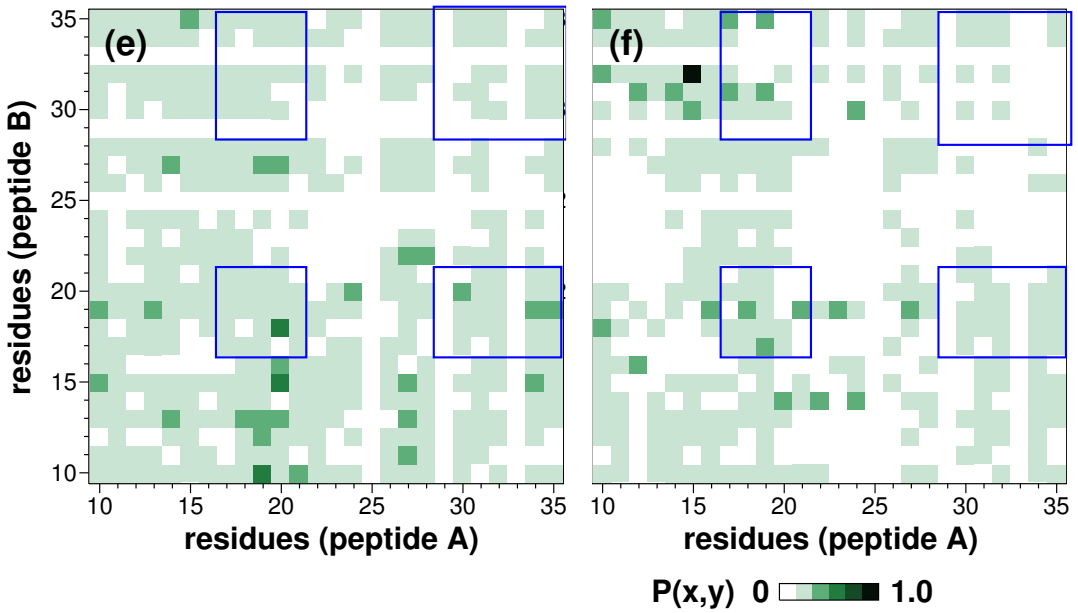

Figure C.2: Intermolecular side chain contacts within Aβ(10-35)-NH_2 dimers at 300 K. Shown are contact maps for minima 5 and 6 of low free energy defined in Fig. 5.5. Regions corresponding to interactions between the central hydrophobic cluster L17 – A21 and the hydrophobic C-terminus G29 – M35 are marked in blue.

Glossary

Aβ Amyloid β.

amu atom mass unit 1.66 x 10^{-27} kg.

e electronic unit charge 1.602 x 10^{-19} C.

κ isothermal compressibility 4.6 x 10^{-5} bar^{-1}.

k_B Boltzmann constant 1.38 x 10^{-23} JK^{-1}.

R ideal gas constant 8.314 $JK^{-1}mol^{-1}$.

AD Alzheimer's disease.

AFM atomic force microscopy.

APP amyloid precursor protein.

CC critical concentration.

CD circular dichroism.

CHC central hydrophobic cluster of Aβ(10-35)-NH_2 involving L17 – A21.

CR Congo red.

D_i conformational state i.

DLS dynamic light scattering.

DSSP Define Secondary Structure in Proteins.

EM electron microscopy.

E_{ang} potential energy of bond angle vibrations.

E_{b} potential energy of bond stretching.

E_{coul} Coulomb interaction energy.

E_{cov} potential energy due to covalent interactions.

E_{dih} potential energy of bond torsion.

E_e electronic ground state energy.

E_{HB} potential energy a hydrogen bond.

E_{imp} potential energy of out-of-plane deflections of aromatic rings.

E_{LJ} Lennard-Jones interaction energy.

E_i potential energy of replica i.

E_{tot} total potential energy.

ΔE_{coul} change in potential energy due to Coulomb interactions.

ΔE_{cov} change in potential energy due to covalent interactions.

ΔE_{LJ} change in potential energy due to Lennard-Jones interactions.

ΔE_{pot} change in total potential energy.

ϵ_{rf} dielectric constant of continuum in reaction field model.

F_{solv} free energy of solvation.

ΔF change in total free energy.

ΔF_{agg} change in free energy of aggregation.

ΔF_{solv} change in free energy of solvation.

$\mathbf{f}_i$ force acting on atom i.

FTIR fourier transform infrared.

GROMACS Groningen Machine for Chemical Simulations, software package.

GROMOS96 43a1 GROningen MOlecular Simulation, 43a1 force field.

H/D exchange Hydrogen/Deuterium exchange.

HFIP hexafluoroisopropanol.

IR infrared.

$^3J_{\mathrm{H^N H^\alpha}}$ scalar coupling constant for interaction between amide proton and H^α.

K equilibrium constant.

LMW low molecular weight.

MD molecular dynamics.

m_i mass of atom i.

NMDA N-methyl D-aspartate.

NMR nuclear magnetic resonance.

NOE nuclear Overhauser effect.

N_{atom} number of atoms.

$N_{\mathrm{Cl-}}$ number of chloride ions in simulation setup.

N_{df} number of degrees of freedom.

N_{HB} number of hydrogen bonds.

N_i number of configurations in state i.

N_{r} number of replica used within REMD simulation.

N_{w} number of water molecules in simulation setup.

OPLS/AA Optimized Potentials for Liquid Simulations/All Atom, force field.

PC principle component.

PCA principle component analysis.

PDB Protein Data Base.

$\mathbf{p}_i$ momentum of atom i.

pK_a negative logarithmic acid dissociation constant.

P pressure.

P_0 reference pressure.

REMD replica exchange molecular dynamics.

R_g radius of gyration.

RMSD root mean square deviation.

$\mathbf{r}_i$ position of atom i.

SASA solvent accessible surface area.

SDS-PAGE sodium dodecyl sulfate polyacrylamide gel electrophoresis.

SLS strand-loop-strand.

SPC simple point charge water model.

$S_{\mathrm{conf},i}$ configurational entropy of state i.

ΔS change in total entropy.

ΔS_{conf} change in configurational entropy.

$\Delta S_{\mathrm{solvent}}$ change in solvent entropy.

SSNMR solid-state nuclear magnetic resonance.

Δt discrete time interval (integration time step).

τ time constant of temperature coupling.

τ_P time constant of pressure coupling.

TEM transmission electron microscopy.

T temperature.

T_0 temperature of heat bath.

T_i temperature of replica i.

ThT thioflavin T.

TIP4P TIP4P water model.

ΔU change in total internal energy.

$\mathbf{v}_i$ velocity of atom i.

Bibliography

[1] A. Rauk. Why is the amyloid β peptide of Alzheimer's disease neurotoxic? *Dalton Trans.*, 2008(10):1273–1282, 2008.

[2] W. Annaert and B. De Strooper. A cell biological perspective on Alzheimer's disease. *Annu. Rev. Cell Dev. Biol.*, 18(1):25–51, 2002.

[3] C. J. Pike, A. J. Walencewicz, C. G. Glabe, and C. W. Cotman. In vitro aging of β amyloid protein causes peptide aggregation and neurotoxicity. *Brain Res.*, 563(1-2):311–314, 1991.

[4] M. P. Lambert, A. K. Barlow, B. A. Chromy, C. Edwards, R. Freed, M. Liosatos, T. E. Morgan, I. Rozovsky, B. Trommer, K. L. Viola, P. Wals, C. Zhang, C. E. Finch, G. A. Krafft, and W. L. Klein. Diffusible, nonfibrillar ligands derived from Aβ1–42 are potent central nervous system neurotoxins. *Proc. Natl. Acad. Sci. USA*, 95(11):6448, 1998.

[5] D. M. Hartley, D. M. Walsh, C. P. Ye, T. Diehl, S. Vasquez, P. M. Vassilev, D. B. Teplow, and D. J. Selkoe. Protofibrillar intermediates of amyloid β-protein induce acute electrophysiological changes and progressive neurotoxicity in cortical neurons. *J. Neurosci.*, 19(20):8876, 1999.

[6] L. F. Lue, Y. M. Kuo, A. E. Roher, L. Brachova, Y. Shen, L. Sue, T. Beach, J. H. Kurth, R. E. Rydel, and J. Rogers. Soluble amyloid β peptide concentration as a predictor of synaptic change in Alzheimer's disease. *Am. J. Pathol.*, 155(3):853, 1999.

[7] C. A. McLean, R. A. Cherny, F. W. Fraser, S. J. Fuller, M. J. Smith, K. Vbeyreuther, A. I. Bush, and C. L. Masters. Soluble pool of Aβ amyloid as a determinant of severity of neurodegeneration in Alzheimer's disease. *Ann. Neurol.*, 46(6):860–866, 1999.

[8] M. Mendes Sousa, I. Cardoso, R. Fernandes, A. Guimaraes, and M. J. Saraiva. Deposition of transthyretin in early stages of familial amyloidotic polyneuropathy: evidence for toxicity of nonfibrillar aggregates. *Am. J. Pathol.*, 159(6):1993, 2001.

[9] J. R. Silveira, G. J. Raymond, A. G. Hughson, R. E. Race, V. L. Sim, S. F. Hayes, and B. Caughey. The most infectious prion protein particles. *Nature*, 437(7056):257–261, 2005.

[10] D. L. Nelson, M. M. Cox, et al. *Lehninger principles of biochemistry*, volume 5. W. H. Freeman New York, 2008.

[11] C. B. Anfinsen, E. Haber, M. Sela, and F. H. White Jr. The kinetics of formation of native ribonuclease during oxidation of the reduced polypeptide chain. *Proc. Natl. Acad. Sci. USA*, 47(9):1309, 1961.

[12] C. B. Anfinsen et al. Principles that govern the folding of protein chains. *Science*, 181(96):223–230, 1973.

[13] J. Buchner and T. Kiefhaber. *Protein Folding Handbook*. Wiley-VCH, 2005.

[14] C. Levinthal. Are there pathways for protein folding. *J. Chim. Phys.*, 65(1):44–45, 1968.

[15] C. Levinthal. How to fold graciously. *Mössbauer spectroscopy in biological systems*, pages 22–24, 1969.

[16] P. L. Clark. Protein folding in the cell: reshaping the folding funnel. *Trends Biochem. Sci.*, 29(10):527–534, 2004.

[17] J. D. Bryngelson, J. N. Onuchic, N. D. Socci, and P. G. Wolynes. Funnels, pathways, and the energy landscape of protein folding: A synthesis. *Proteins*, 21(3):167–195, 1995.

[18] J. N. Onuchic, P. G. Wolynes, Z. Luthey-Schulten, and N. D. Socci. Toward an outline of the topography of a realistic protein-folding funnel. *Proc. Natl. Acad. Sci. USA*, 92(8):3626, 1995.

[19] E. Sackmann and R. Merkel. *Lehrbuch der Biophysik*. Wiley-VCH, 2010.

[20] R. F. Goldberger et al. Acceleration of reactivation of reduced bovine pancreatic ribonuclease by a microsomal system from rat liver. *J. Biol. Chem.*, 238:628, 1963.

[21] J. London, C. Skrzynia, and M. E. Goldberg. Renaturation of *Escherichia coli* tryptophanase after exposure to 8 M urea. Evidence for the existence of nucleation centers. *Eur. J. Biochem.*, 47(2):409–415, 1974.

[22] M. A. Speed, D. I. C. Wang, and J. King. Multimeric intermediates in the pathway to the aggregated inclusion body state for P22 tailspike polypeptide chains. *Protein Sci.*, 4(5):900–908, 1995.

[23] A. Mitraki and J. King. Protein Folding Intermediates and Inclusion Body Formation. *Nature Biotechnology*, 7(7):690–697, 1989.

[24] R. Wetzel. For protein misassembly, it's the "I" decade. *Cell*, 86(5):699, 1996.

[25] A. J. L. Macario and E. C. de Macario. Sick chaperones and ageing: a perspective. *Ageing Res. Rev.*, 1(2):295–311, 2002.

[26] F. Chiti and C. M. Dobson. Protein misfolding, functional Amyloid, and human disease. *Ann. Rev. Biochem.*, 75:333, 2006.

[27] A. K. Paravastu, I. Qahwash, R. D. Leapman, S. C. Meredith, and R. Tycko. Seeded growth of β-amyloid fibrils from Alzheimer's brain-derived fibrils produces a distinct fibril structure. *Proc. Natl. Acad. Sci. USA*, 106(18):7443, 2009.

[28] P. H. Von Hippel and T. Schleich. *Structure and stability of biological macromolecules*, volume 417. Marcel Dekker, New York, 1969.

[29] L. C. Serpell. Alzheimer's amyloid fibrils: structure and assembly. *Biochem. Biophys. Acta*, 1502(1):16–30, 2000.

[30] Y. Bai, J. S. Milne, L. Mayne, and S. W. Englander. Primary structure effects on peptide group hydrogen exchange. *Proteins*, 17(1):75–86, 1993.

[31] C. M. Dobson. Protein folding and misfolding. *Nature*, 426(6968):884–890, 2003.

[32] F. Chiti, P. Webster, N. Taddei, A. Clark, M. Stefani, G. Ramponi, and C. M. Dobson. Designing conditions for in vitro formation of amyloid protofilaments and fibrils. *Proc. Natl. Acad. Sci. USA*, 96(7):3590, 1999.

[33] C. M. Dobson. Protein misfolding, evolution and disease. *Trends Biochem. Sci.*, 24(9):329–332, 1999.

[34] C. M. Dobson. Protein folding and disease: a view from the first Horizon Symposium. *Nature Rev. Drug Disc.*, 2(2):154–160, 2003.

[35] M. Fändrich and C. M. Dobson. The behavior of polyamino acids reveals an inverse side chain effect in amyloid structure formation. *EMBO J.*, 21(21):5682–5690, 2002.

[36] H. Naiki, N. Hashimoto, S. Suzuki, H. Kimura, K. Nakakuki, and F. Gejyo. Establishment of a kinetic model of dialysis-related amyloid fibril extension *in vitro*. *Amyloid*, 4(4):223–232, 1997.

[37] T. R. Serio, A. G. Cashikar, A. S. Kowal, G. J. Sawicki, J. J. Moslehi, L. Serpell, M. F. Arnsdorf, and S. L. Lindquist. Nucleated conformational conversion and the replication of conformational information by a prion determinant. *Science*, 289(5483):1317, 2000.

[38] V. N. Uversky, J. Li, P. Souillac, I. S. Millett, S. Doniach, R. Jakes, M. Goedert, and A. L. Fink. Biophysical properties of the synucleins and their propensities to fibrillate. *J. Biol. Chem.*, 277(14):11970, 2002.

[39] J. S. Pedersen, G. Christensen, and D. E. Otzen. Modulation of S6 fibrillation by unfolding rates and gatekeeper residues. *J. Molec. Biol.*, 341(2):575–588, 2004.

[40] Z. Ignatova, A. K. Thakur, R. Wetzel, and L. M. Gierasch. In-cell aggregation of a polyglutamine-containing chimera is a multistep process initiated by the flanking sequence. *J. Biol. Chem.*, 282(50):36736, 2007.

[41] A. K. Thakur, M. Jayaraman, R. Mishra, M. Thakur, V. M. Chellgren, I. J. L. Byeon, D. H. Anjum, R. Kodali, T. P. Creamer, J. F. Conway, A. M. Gronenborn, and R. Wetzel. Polyglutamine disruption of the huntingtin exon 1 N terminus triggers a complex aggregation mechanism. *Nature Struct. & Mol. Biol.*, 16(4):380–389, 2009.

[42] A. R. Hurshman, J. T. White, E. T. Powers, and J. W. Kelly. Transthyretin aggregation under partially denaturing conditions is a downhill polymerization. *Biochemistry*, 43(23):7365–7381, 2004.

[43] J. Juárez, P. Taboada, and V. Mosquera. Existence of different structural intermediates on the fibrillation pathway of human serum albumin. *Biophys. J.*, 96(6):2353–2370, 2009.

[44] J. D. Harper, C. M. Lieber, and P. T. Lansbury Jr. Atomic force microscopic imaging of seeded fibril formation and fibril branching by the Alzheimer's disease amyloid-β protein. *Chem. Biol.*, 4(12):951–959, 1997.

[45] J. D. Harper, S. S. Wong, C. M. Lieber, and P. T. Lansbury Jr. Assembly of Aβ Amyloid Protofibrils: An in Vitro Model for a Possible Early Event in Alzheimer's Disease. *Chem. Biol.*, 38(28):8972–8980, 1999.

[46] D. M. Walsh, D. M. Hartley, Y. Kusumoto, Y. Fezoui, M. M. Condron, A. Lomakin, G. B. Benedek, D. J. Selkoe, and D. B. Teplow. Amyloid β-protein fibrillogenesis. *J. Biol. Chem.*, 274(36):25945, 1999.

[47] G. Bitan, M. D. Kirkitadze, A. Lomakin, S. S. Vollers, G. B. Benedek, and D. B. Teplow. Amyloid β-protein (Aβ) assembly: Aβ40 and Aβ42 oligomerize through distinct pathways. *Proc. Natl. Acad. Sci. USA*, 100(1):330, 2003.

[48] M. Sakono and T. Zako. Amyloid oligomers: formation and toxicity of Aβ oligomers. *FEBS J.*, 277(6):1348–1358, 2010.

[49] Alzheimer's association. `http://www.alz.org`.

[50] A. C. Alonso, T. Zaidi, M. Novak, I. Grundke-Iqbal, and K. Iqbal. Hyperphosphorylation induces self-assembly of τ into tangles of paired helical filaments/straight filaments. *Proc. Natl. Acad. Sci. USA*, 98(12):6923, 2001.

[51] A. Alzheimer. Über eine eigenartige Erkrankung der Hirnrinde. *Allg. Zeit. Psychiatrie Psychisch-Gerichtl. Med.*, 64:146–148, 1907.

[52] F. M. LaFerla, K. N. Green, and S. Oddo. Intracellular amyloid-β in Alzheimer's disease. *Nature Rev. Neurosci.*, 8(7):499–509, 2007.

[53] E. Gaggelli, H. Kozlowski, D. Valensin, and G. Valensin. Copper homeostasis and neurodegenerative disorders (Alzheimer's, prion, and Parkinson's diseases and amyotrophic lateral sclerosis). *Chem. Rev.*, 106(6):1995–2044, 2006.

[54] S. Zhang, K. Iwata, M. J. Lachenmann, J. W. Peng, S. Li, E. R. Stimson, Y. Lu, A. M. Felix, J. E. Maggio, and J. P. Lee. The Alzheimer's peptide Aβ adopts a collapsed coil structure in water. *J. Struct. Biol.*, 130(2-3):130–141, 2000.

[55] R. Riek, P. Güntert, H. Döbeli, B. Wipf, and K. Wüthrich. NMR studies in aqueous solution fail to identify significant conformational differences between the monomeric forms of two Alzheimer peptides with widely different plaque-competence, Aβ(1-40)(ox) and Aβ(1-42)(ox). *Eur. J. Biochem.*, 268(22):5930, 2001.

[56] C. G. Glabe. Structural classification of toxic amyloid oligomers. *J. Biol. Chem.*, 283(44):29639, 2008.

[57] R. Kayed, E. Head, J. L. Thompson, T. M. McIntire, S. C. Milton, C. W. Cotman, and C. G. Glabe. Common structure of soluble amyloid oligomers implies common mechanism of pathogenesis. *Science*, 300(5618):486, 2003.

[58] A. T. Petkova, Y. Ishii, J. J. Balbach, O. N. Antzutkin, R. D. Leapman, F. Delaglio, and R. Tycko. A structural model for Alzheimer's β-amyloid fibrils based on experimental constraints from solid state NMR. *Proc. Natl. Acad. Sci. USA*, 99(26):16742–16747, 2002.

[59] N. A. Whittemore, R. Mishra, I. Kheterpal, A. D. Williams, R. Wetzel, and E. H. Serpersu. Hydrogen-deuterium (H/D) exchange mapping of Aβ1-40 amyloid fibril secondary structure using nuclear magnetic resonance spectroscopy. *Biochemistry*, 44(11):4434–4441, 2005.

[60] T. Lührs, C. Ritter, M. Adrian, D. Riek-Loher, B. Bohrmann, H. Döbeli, D. Schubert, and R. Riek. 3D structure of Alzheimer's amyloid-β (1–42) fibrils. *Proc. Natl. Acad. Sci. USA*, 102(48):17342, 2005.

[61] C. J. Pike, A. J. Walencewicz-Wasserman, J. Kosmoski, D. H. Cribbs, C. G. Glabe, and C. W. Cotman. Structure-activity analyses of β-amyloid peptides: contributions of the beta 25-35 region to aggregation and neurotoxicity. *J. Neurochem.*, 64(1):253–265, 1995.

[62] G. Wei and J. E. Shea. Effects of solvent on the structure of the Alzheimer amyloid-β(25-35) peptide. *Biophys. J.*, 91(5):1638, 2006.

[63] A. M. D'Ursi, M. R. Armenante, R. Guerrini, S. Salvadori, G. Sorrentino, and D. Picone. Solution structure of Amyloid β-peptide (25-35) in different media. *J. Med. Chem.*, 47(17):4231–4238, 2004.

[64] J. H. Ippel, A. Olofsson, J. Schleucher, E. Lundgren, and S. S. Wijmenga. Probing solvent accessibility of amyloid fibrils by solution NMR spectroscopy. *Proc. Natl. Acad. Sci. USA*, 99(13):8648–8653, 2002.

[65] R. Liu, C. McAllister, Y. Lyubchenko, and M. R. Sierks. Residues 17-20 and 30-35 of β-amyloid play critical roles in aggregation. *J. Neurosci. Res.*, 75(2):162–171, 2004.

[66] L. O. Tjernberg, J. Näslund, F. Lindqvist, J. Johansson, A. R. Karlström, J. Thyberg, L. Terenius, and C. Nordstedt. Arrest of amyloid fibril formation by a pentapeptide ligand. *J. Biol. Chem.*, 271(15):8545, 1996.

[67] Z. X. Yao and V. Papadopoulos. Function of β-amyloid in cholesterol transport: a lead to neurotoxicity. *FASEB J.*, page 202851, 2002.

[68] M. J. Sadowski, J. Pankiewicz, H. Scholtzova, P. D. Mehta, F. Prelli, D. Quartermain, and T. Wisniewski. Blocking the apolipoprotein E/amyloid-β interaction as a potential therapeutic approach for Alzheimer's disease. *Proc. Natl. Acad. Sci. USA*, 103(49):18787, 2006.

[69] H. Y. Wang, D. H. S. Lee, C. B. Davis, and R. P. Shank. Amyloid peptide Aβ1-42 binds selectively and with picomolar affinity to α7 nicotinic acetylcholine receptors. *J. Neurochem.*, 75(3):1155–1161, 2000.

[70] J. W. Lustbader et al. ABAD directly links Aβ to mitochondrial toxicity in Alzheimer's disease. *Science*, 304(5669):448, 2004.

[71] J. P. Lee, E. R. Stimson, J. R. Ghilardi, P. W. Mantyh, Y. A. Lu, A. M. Felix, W. Llanos, A. Behbin, M. Cummings, M. Vancriekinge, W. Timms, and J. E. Maggio. ^{1}H-NMR of Aβ amyloid peptide congeners in water solution - conformational changes correlate with plaque competence. *Biochemistry*, 34(15):5191–5200, 1995.

[72] O. N. Antzutkin, R. D. Leapman, J. J. Balbach, and R. Tycko. Supramolecular structural constraints on Alzheimer's β-amyloid fibrils from electron microscopy and solid-state nuclear magnetic resonance. *Biochemistry*, 41(51):15436–15450, 2002.

[73] D. M. Gregory, T. L. S. Benzinger, T. S. Burkoth, H. Miller-Auer, D. G. Lynn, S. C. Meredith, and R. E. Botto. Dipolar recoupling NMR of biomolecular self-assemblies: determining inter- and intrastrand distances in fibrilized Alzheimer's β-amyloid peptide. *Solid State Nucl. Magn. Reson.*, 13(3):149–166, 1998.

[74] T. L. S. Benzinger, D. M. Gregory, T. S. Burkoth, H. Miller-Auer, D. G. Lynn, R. E. Botto, and S. C. Meredith. Propagating structure of Alzheimer's β-amyloid(10-35) is parallel β-sheet with residues in exact register. *Proc. Natl. Acad. Sci. USA*, 95(23):13407–13412, 1998.

[75] T. L. S. Benzinger, D. M. Gregory, T. S. Burkoth, H. Miller-Auer, D. G. Lynn, R. E. Botto, and S. C. Meredith. Two-dimensional structure of β-amyloid(10-35) fibrils. *Biochemistry*, 39(12):3491–3499, 2000.

[76] T. S. Burkoth, T. L. S. Benzinger, V. Urban, D. M. Morgan, D. M. Gregory, P. Thiyagarajan, R. E. Botto, S. C. Meredith, and D. G. Lynn. Structure of the β-amyloid (10-35) fibril. *J. Am. Chem. Soc.*, 122(33):7883–7889, 2000.

[77] B. Ma and R. Nussinov. Stabilities and conformations of Alzheimer's β-amyloid peptide oligomers (Aβ(16-22), Aβ(16-35), and Aβ(10-35)): Sequence effects. *Proc. Natl. Acad. Sci. USA*, 99(22):14126–14131, 2002.

[78] B. Tarus, J. E. Straub, and D. Thirumalai. Probing the initial stage of aggregation of the Aβ10-35-protein: Assessing the propensity for peptide dimerization. *J. Molec. Biol.*, 345(5):1141–1156, 2005.

[79] S. Jang and S. Shin. Amyloid β-peptide oligomerization in silico: Dimer and trimer. *J. Phys. Chem. B*, 110(5):1955–1958, 2006.

[80] S. Jang and S. Shin. Computational study on the structural diversity of amyloid β peptide (Aβ 10-35) oligomers. *J. Phys. Chem. B*, 112(11):3479–3484, 2008.

[81] G. Valincius, F. Heinrich, R. Budvytyte, D. J. Vanderah, D. J. McGillivray, Y. Sokolov, J. E. Hall, and M. Lösche. Soluble amyloid β-oligomers affect dielectric

membrane properties by bilayer insertion and domain formation: Implications for cell toxicity. *Biophys. J.*, 95(10):4845–4861, 2008.

[82] M. Kawahara and Y. Kuroda. Molecular mechanism of neurodegeneration induced by Alzheimer's β-amyloid protein: channel formation and disruption of calcium homeostasis. *Brain Res. Bull.*, 53(4):389–397, 2000.

[83] L. Rajendran, A. Schneider, G. Schlechtingen, S. Weidlich, J. Ries, T. Braxmeier, P. Schwille, J.B. Schulz, C. Schroeder, M. Simons, G. Jennings, H. Knölker, and K. Simons. Efficient inhibition of the Alzheimer's disease β-secretase by membrane targeting. *Science*, 320(5875):520, 2008.

[84] H. J. C. Berendsen. *Simulating the physical world*. Cambridge University Press, 2007.

[85] Y. Sugita and Y. Okamoto. Replica-exchange molecular dynamics method for protein folding. *Chem. Phys. Lett.*, 314(1-2):141–151, 1999.

[86] G. M. Torrie and J. P. Valleau. Nonphysical sampling distributions in Monte Carlo free-energy estimation: umbrella sampling. *J. Comp. Phys.*, 23(2):187–199, 1977.

[87] D. van der Spoel, E. Lindahl, B. Hess, G. Groenhof, A. E. Mark, and H. J. C. Berendsen. GROMACS: fast, flexible, and free. *J. Comp. Chem.*, 26(16):1701–1718, 2005.

[88] E. Schrödinger. An undulatory theory of the mechanics of atoms and molecules. *Phys. Rev.*, 28:1049–1070, 1926.

[89] M. Born and R. Oppenheimer. Zur Quantentheorie der Molekeln. *Annalen der Physik*, 389(20):457–484, 1927.

[90] D. van der Spoel, H. J. C. Berendsen, A. R. van Buuren, E. Apol, P. J. Meulenhoff, A. L. T. M. Sijbers, and R. van Drunen. *GROMACS User Manual*. Nijenborgh 4, 9747 AG Groningen, The Netherlands. Electronic access: `http://md.chem.rug.nl/~gmx`, 1995.

[91] J. E. Lennard-Jones. The determination of molecular fields. II. From the equation of state of a gas. In *Proc. Roy. Soc. (Lond.)*, volume 106, page 463, 1924.

[92] L. D. Schuler, X. Daura, and W. F. van Gunsteren. An improved GROMOS 96 force field for aliphatic hydrocarbons in the condensed phase. *J. Comp. Chem.*, 22(11):1205–1218, 2001.

[93] G. A. Kaminski, R. A. Friesner, J. Tirado-Rives, and W. L. Jorgensen. Evaluation and reparametrization of the OPLS-AA force field for proteins via comparison with accurate quantum chemical calculations on peptides. *J. Phys. Chem. B*, 105(28):6474–6487, 2001.

[94] H. J. C. Berendsen, J. P. M. Postma, W. F. van Gunsteren, and J. Hermans. *Interaction models for water in relation to protein hydration*. D. Reidel Publishing Company, Dordrecht, 1981.

[95] J. Hermans, H. J. C. Berendsen, W. F. van Gunsteren, and J. P. M. Postma. A consistent empirical potential for water-protein interactions. *Biopolymers*, 23(8):1513–1518, 1984.

[96] W. L. Jorgensen, J. Chandrasekhar, and J. D. Madura. Comparison of simple potential functions for simulating liquid water. *J. Chem. Phys.*, 79:926–935, Jul. 1983.

[97] M. P. Allen and D. J. Tildesley. *Computer simulation of liquids*. Clarendon Press, 1989.

[98] M. P. Allen. Introduction to molecular dynamics simulation. *Comp. Soft Matter: From Synthetic Polymers to Proteins*, 23:1–28, 2004.

[99] S. Nóse. A molecular dynamics method for simulations in the canonical ensemble. *Molec. Phys.*, 52:255–268, 1984.

[100] W. G. Hoover. Canonical dynamics: Equilibrium phase-space distributions. *Phys. Rev. A*, 31(3):1695–1697, 1985.

[101] H. J. C. Berendsen, J. P. M. Postma, W. F. van Gunsteren, A. Di Nola, and J. R. Haak. Molecular-dynamics with coupling to an external bath. *J. Chem. Phys.*, 81(8):3684–3690, 1984.

[102] W. F. van Gunsteren and M. Karplus. Effect of constraints on the dynamics of macromolecules. *Macromolecules*, 15(6):1528–1544, 1982.

[103] B. Hess, H. Bekker, H. J. C. Berendsen, and J. G. E. M. Fraaije. LINCS: A linear constraint solver for molecular simulations. *J. Comp. Chem.*, 18(12):1463–1472, 1997.

[104] S. Miyamoto and P. A. Kollman. SETTLE: An analytical version of the SHAKE and RATTLE algorithms for rigid water models. *J. Comp. Chem.*, 13:952–962, 1992.

[105] K. A. Feenstra, B. Hess, and H. J. C. Berendsen. Improving efficiency of large time-scale molecular dynamics simulations of hydrogen-rich systems. *J. Comp. Chem.*, 20:786–798, 1999.

[106] P. E. Smith and W. F. van Gunsteren. Consistent dielectric properties of the simple point charge and extended simple point charge water models at 277 and 300 K. *J. Chem. Phys.*, 100:3169, 1994.

[107] I. G. Tironi, R. Sperb, P. E. Smith, and W. F. van Gunsteren. A generalized reaction field method for molecular-dynamics simulations. *J. Chem. Phys.*, 102:5451–5459, 1995.

[108] X. Periole and A. E. Mark. Convergence and sampling efficiency in replica exchange simulations of peptide folding in explicit solvent. *J. Chem. Phys.*, 126:014903, 2007.

[109] M. J. Abraham and J. E. Gready. Ensuring mixing efficiency of replica-exchange molecular dynamics simulations. *J. Chem. Theory Comput.*, 4(7):1119–1128, 2008.

[110] W. Kabsch and C. Sander. Dictionary of protein secondary structure: Pattern recognition of hydrogen-bonded and geometrical features. *Biopolymers*, 22:2577–2637, 1983.

[111] X. Daura, K. Gademann, B. Jaun, D. Seebach, W. F. van Gunsteren, and A. E. Mark. Peptide folding: When simulation meets experiment. *Angew. Chem. Int. Ed. Engl.*, 38:236–240, 1999.

[112] A. Shrake and J. A. Rupley. Environment and exposure to solvent of protein atoms. Lysozyme and insulin. *J. Molec. Biol.*, 79(2):351–364, 1973.

[113] B. Lee and F. M. Richards. The interpretation of protein structures: estimation of static accessibility. *J. Molec. Biol.*, 55(3):379–400, 1971.

[114] D. Eisenberg and A. D. McLachlan. Solvation energy in protein folding and binding. *Nature*, 319(6050):199–203, 1986.

[115] W. Han and Y. D. Wu. A strand-loop-strand structure is a possible intermediate in fibril elongation: Long time simulations of Amyloid-β peptide (10- 35). *J. Am. Chem. Soc.*, 127(44):15408–15416, 2005.

[116] B. Hess. Similarities between principal components of protein dynamics and random diffusion. *Phys. Rev. E*, 62(6):8438–8448, 2000.

[117] B. Hess. Convergence of sampling in protein simulations. *Phys. Rev. E*, 65(3):31910, 2002.

[118] D. F. Evans and H. Wennerström. *The colloidal domain. Where physics, chemistry, biology, and technology meet.* Wiley, 1999.

[119] E. Terzi, G. Hölzemann, and J. Seelig. Reversible random coil-β-sheet transition of the Alzheimer β-amyloid fragment(25-35). *Biochemistry*, 33(6):1345–1350, 1994.

[120] S. Hashioka, A. Monji, T. Ueda, S. Kanba, and H. Nakanishi. Amyloid β fibril formation is not necessarily required for microglial activation by the peptides. *Neurochem. Int.*, 47(5):369–376, 2005.

[121] M. D. Martinez-Senac, J. Villalain, and J. C. Gomez-Fernandez. Structure of the Alzheimer β-amyloid peptide (25-35) and its interaction with negatively charged phospholipid vesicles. *Eur. J. Biochem.*, 265(2):744–753, 1999.

[122] S. T. Kim and D. F. Weaver. Theoretical studies on Alzheimer's disease: structures of β-amyloid aggregates. *J. Mol. Struct. Theochem*, 527(Sp. Iss. SI):127–138, 2000.

[123] B. Y. Ma and R. Nussinov. The stability of monomeric intermediates controls amyloid formation: Aβ 25-35 and its N27Q mutant. *Biophys. J.*, 90(10):3365–3374, 2006.

[124] G. Wei, A. I. Jewett, and J. E. Shea. Structural diversity of dimers of the Alzheimer amyloid-β(25-35) peptide and polymorphism of the resulting fibrils. *Phys. Chem. Chem. Phys.*, 12(14):3622–3629, 2010.

[125] V. Knecht. β-hairpin folding by a model amyloid peptide in solution and at an interface. *J. Phys. Chem. B*, 112(31):9476–9483, 2008.

[126] A. Monji, H. Utsumi, T. Ueda, T. Imoto, I. Yoshida, S. Hashioka, K. Tashiro, and N. Tashiro. Amyloid-β-protein (Aβ)(25–35)-associated free radical generation is strongly influenced by the aggregational state of the peptides. *Life Sciences*, 70(7):833–841, 2002.

[127] G. Boucher, N. Mousseau, and P. Derreumaux. Aggregating the amyloid Aβ(11-25) peptide into a four-stranded β-sheet structure. *Proteins*, 65(4):877–888, 2006.

[128] L. Reich. *Folding dynamics and stability of proteins.* PhD thesis, Univ. Potsdam, 2009.

[129] C. Wu, H. X. Lei, and Y. Duan. Formation of partially ordered oligomers of amyloidogenic hexapeptide (NFGAIL) in aqueous solution observed in molecular dynamics simulations. *Biophys. J.*, 87(5):3000–3009, 2004.

[130] S. A. Petty and S. M. Decatur. Intersheet rearrangement of polypeptides during nucleation of β-sheet aggregates. *Proc. Natl. Acad. Sci. USA*, 102(40):14272–14277, 2005.

[131] G. Cevc and D. Marsh. Phospholipid bilayers: Physical principles and models. *Cell biology (USA)*, 1987.

[132] G. Shanmugam and R. Jayakumar. Structural analysis of amyloid β peptide fragment (25–35) in different microenvironments. *Biopolymers*, 76(5):421–434, 2004.

[133] D. Matthes and B. L. de Groot. Secondary structure propensities in peptide folding simulations: A systematic comparison of molecular mechanics interaction schemes. *Biophys. J.*, 97(2):599–608, 2009.

[134] A. Baumketner and J. E. Shea. The structure of the Alzheimer amyloid β 10-35 peptide probed through replica-exchange molecular dynamics simulations in explicit solvent. *J. Molec. Biol.*, 366(1):275–285, 2007.

[135] C. R. Cantor and P. R. Schimmel. *Biophysical Chemistry, Part I: The conformation of biological macromolecules*. W.H. Freeman & Co, 1980.

[136] J. Cavanagh, W. J. Fairbrother, A. G. Palmer, N. J. Skelton, and M. Rance. *Protein NMR Spectroscopy. Principles and Practice*. Academic Press, 2006.

[137] M. P. Williamson, T. F. Havel, and K. Wüthrich. Solution conformation of proteinase inhibitor-IIA from bull seminal plasma by ^{1}H nuclear magnetic resonance and distance geometry. *J. Molec. Biol.*, 182(2):295–315, 1985.

[138] N. Tjandra and A. Bax. Direct measurement of distances and angles in biomolecules by NMR in a dilute liquid crystalline medium. *Science*, 278(5340):1111–1114, 1997.

[139] G. Cornilescu, F. Delaglio, and A. Bax. Protein backbone angle restraints from searching a database for chemical shift and sequence homology. *J. Biomol. NMR*, 13(3):289–302, 1999.

[140] G. Wagner. Characterization of the distribution of internal motions in the basic pancreatic trypsin-inhibitor using a large number of internal NMR probes. *Q. Rev. Biophys.*, 16(1):1–57, 1983.

[141] Y. X. Wang, J. Jacob, F. Cordier, P. Wingfield, S. J. Stahl, S. Lee-Huang, D. Torchia, S. Grzesiek, and A. Bax. Measurement of $^{3h}J_{NC'}$ connectivities across hydrogen bonds in a 30 kDa protein. *J. Biomol. NMR*, 14(2):181–184, 1999.

[142] V. Gaponenko, S. P. Sarma, A. S. Altieri, D. A. Horita, J. Li, and R. A. Byrd. Improving the accuracy of NMR structures of large proteins using pseudocontact shifts as long-range restraints. *J. Biomol. NMR*, 28(3):205–212, 2004.

[143] I. Bertini, C. Luchinat, and M. Piccioli. Paramagnetic probes in metalloproteins. *Meth. Enzymology*, 339:314, 2001.

[144] J. Iwahara, C. D. Schwieters, and G. M. Clore. Ensemble approach for NMR structure refinement against ^{1}H paramagnetic relaxation enhancement data arising from a flexible paramagnetic group attached to a macromolecule. *J. Am. Chem. Soc.*, 126(18):5879–5896, 2004.

[145] H. Friebolin. *Ein-und zweidimensionale NMR-Spektroskopie – Eine Einführung.* Wiley-VCH, 2006.

[146] M. Karplus. Contact Electron-Spin Coupling of Nuclear Magnetic Moments. *J. Chem. Phys.*, 30(1):11–15, 1959.

[147] A. Pardi, M. Billeter, and K. Wüthrich. Calibration of the angular dependence of the amide proton-C$^{\alpha}$ proton coupling constants, $^{3}J_{HN\alpha}$, in a globular protein: Use of $^{3}J_{HN\alpha}$ for identification of helical secondary structure. *J. Molec. Biol.*, 180(3):741–751, 1984.

[148] J. E. Nielsen and G. Vriend. Optimizing the hydrogen-bond network in Poisson-Boltzmann equation-based pKa calculations. *Proteins*, 43(4):403–412, 2001.

[149] J. E. Nielsen and J. A. McCammon. Calculating pKa values in enzyme active sites. *Protein Sci.*, 12(9):1894–1901, 2003.

[150] J. E. Nielsen and J. A. McCammon. On the evaluation and optimization of protein X-ray structures for pKa calculations. *Protein Sci.*, 12(2):313–326, 2003.

Danksagung

An dieser Stelle möchte ich mich bei all denen bedanken, die es mir ermöglicht haben, diese Arbeit anzufertigen und die mich auf diesem langen, manchmal schwierigen Weg begleitet haben.

Als erstes möchte ich mich bei Prof. Reinhard Lipowsky bedanken. Er hat mir die Möglichkeit gegeben, meine Doktorarbeit in seiner Abteilung am MPI für Kolloid- und Grenzflächenforschung anzufertigen. Ganz besonderer Dank gilt meinem Betreuer Dr. Volker Knecht. Er ermöglichte mir die Arbeit an einem spannenden Thema und den wissenschaftlichen Austausch über die Institutsgrenzen hinaus. Seine Tür stand immer offen, um Fragen zu diskutieren und Lösungen für Probleme zu suchen. Vielen Dank.

Bei Prof. Robert Seckler möchte ich mich dafür bedanken, dass er mir ermöglicht hat, diese Arbeit an der Universität Potsdam einzureichen. Er und die Mitarbeiter seiner Arbeitsgruppe haben viele meiner Fragen bezüglich experimenteller Methoden in der Biochemie geduldig beantwortet. Vielen Dank für die Diskussionen und Euer Interesse an den Ergebnissen meiner theoretischen Modellierungen.

Eine sehr angenehme und abwechslungsreiche Arbeitsatmosphäre verdanke ich allen Mitarbeitern der Theorieabteilung – ganz besonders Margarita, Jörg, und meinen wechselnden Bürokollegen Caro, Flo, Neha und Yulyia. Dank gilt auch Marco Ehlert, der bei Hardware- und Softwareproblemen jederzeit zur Stelle war.

Für jegliche Unterstützung während der vergangenen Jahre danke ich meiner Familie und meinen Freunden. Das gilt insbesondere für meine Eltern, Bea, Maria, Ramona und Stephie die mir Zeit zum Arbeiten an unzähligen Nachmittagen verschafft haben. Ganz besonders danke ich Steffen fürs Dasein in ganz vielen Momenten, sein Verständnis und seine Geduld, vor allem in den letzten Wochen. Ohne ihn wäre das alles nicht möglich gewesen.